



TECHNISCHE
UNIVERSITÄT
WIEN

Vienna University of Technology

DISSERTATION

Liquid-Repellent Surfaces based on Nanostructured Silicon Substrates

ausgeführt zum Zwecke der Erlangung des akademischen Grades eines
Doktors der technischen Wissenschaften (Dr.techn.)

unter der Leitung von

Ao.Univ.Prof. Dipl.-Ing. Dr.techn. Helmuth Hoffmann

Institut 163

für Angewandte Synthesechemie

eingereicht an der Technischen Universität Wien,

Fakultät für Technische Chemie

von

Roland Bittner, BSc. MSc.

0505319

Pannaschgasse 4/11

1050 Wien



Die approbierte Originalversion dieser Dissertation ist in der Hauptbibliothek der Technischen Universität Wien aufgestellt und zugänglich.

<http://www.ub.tuwien.ac.at>



The approved original version of this thesis is available at the main library of the Vienna University of Technology.

<http://www.ub.tuwien.ac.at/eng>



TECHNISCHE
UNIVERSITÄT
WIEN

Vienna University of Technology

Ich habe zur Kenntnis genommen, dass ich zur Drucklegung meiner Arbeit unter der Bezeichnung

Dissertation

nur mit Bewilligung der Prüfungskommission berechtigt bin.

Ich erkläre weiters Eides statt, dass ich meine Dissertation nach den anerkannten Grundsätzen für wissenschaftliche Abhandlungen selbstständig ausgeführt habe und alle verwendeten Hilfsmittel, insbesondere die zugrunde gelegte Literatur, genannt habe.

Weiters erkläre ich, dass ich dieses Dissertationsthema bisher weder im In- noch Ausland einer Beurteilerin/einem Beurteiler zur Begutachtung in irgendeiner Form als Prüfungsarbeit vorgelegt habe und dass diese Arbeit mit der vom Begutachter beurteilten Arbeit übereinstimmt.



Die approbierte Originalversion dieser Dissertation ist in der Hauptbibliothek der Technischen Universität Wien aufgestellt und zugänglich.

<http://www.ub.tuwien.ac.at>



The approved original version of this thesis is available at the main library of the Vienna University of Technology.

<http://www.ub.tuwien.ac.at/eng>

Acknowledgments

The approved original version of this thesis is
available at the main library of the Vienna
University of Technology.

<http://www.ub.tuwien.ac.at>

I would like to express my deep gratitude to Prof. Helmuth Hoffmann for his intense support and supervision throughout the whole thesis, always having spare time to give me competent advice and for giving me the opportunity to work in his group.

I want to thank Prof. Marko Mihovilovic for entrusting me with an employment at the institute which enabled me doing this work and especially for supporting me beyond that to finish my thesis in the course of 'Bildungskarenz'.

I am also particularly grateful for the fruitful scientific cooperation with Prof. Karl Kirchner and for his effort to establish the organisational foundation allowing me to apply for 'Bildungskarenz' in the first place.

Advice and ionic liquids supplied by Prof. Katharina Schröder has been proven to be indispensable and greatly enhanced the scope of the work beyond the original intent, setting the course of the second half of the thesis to a relatively little investigated but highly interesting topic.

I wish to acknowledge the help and productive discussions with Prof. Gernot Friedbacher, granting me access to the SEM device, providing me with invaluable insights in the etching process and for encouraging me to accompany him on conferences.

Special thanks have to be given to Elisabeth Eitenberger who eagerly performed all SEM measurements, also only on short notice, and helped interpreting the results.

It is especially important for me to express a particularly hearty appreciation for the contribution of Sarah Umdasch whose unconditional support in all its facets regarding the thesis and beyond can hardly be put into words.

I am very grateful for the ongoing support of my parents for the entirety of my whole studies without whom it would not have been possible, providing me the necessary spiritual and financial backing and encouragement to stay on track.

Finally, I want to thank all my colleagues, especially from the groups of Prof. Kirchner, Prof. Linert and Prof. Weinberger, not only for research related discussions and for occasionally performing an experiment for me but also for providing an enjoyable working atmosphere, particularly during lunch and coffee breaks.

This work focuses on the preparation of liquid repellent surfaces. We follow two fundamentally different biomimetic approaches to reach this goal, Cassie-Baxter systems and SLIPS (Slippery Liquid Infused Porous Surfaces) systems.

Cassie-Baxter systems are commonly found in nature, with the lotus leaf as the most popular example. They combine high surface roughness and low surface energy to reach superlyophobic properties with contact angles above 150° and a contact angle hysteresis below 10° . In order to mimic such a surface, we first employed silver assisted etching of a silicon substrate to create a rough surface covered in upright standing silicon nanowires. This surface was then coated with a covalently bound monolayer of an azide-terminated silane, which was subsequently coupled with a polyfluorinated alkyne in a Huisgen 1,3-dipolar cycloaddition, leading to the desired low surface energy. This procedure ensures that the second layer is also present on the surface as a monolayer, maintaining the initial surface structure, while allowing easy variation of the terminal functionality and adjustment to the demands of different practical applications. Overall, a contact angle of $168 \pm 3^\circ$ for water and even more impressively $113 \pm 2^\circ$ for ethanol, which is much harder to repel due to its lower surface tension, was achieved.

While less widespread, SLIPS systems can also be found in nature. For example, carnivorous pitcher plants use SLIPS surfaces to catch their prey. In general, SLIPS use porous surfaces impregnated with a lubricant liquid to repel a second, immiscible liquid. The second liquid only comes in contact with the impregnation liquid. The contact angles are much smaller in SLIPS systems compared with Cassie-Baxter surfaces but, due to the negligible hysteresis, the slightest tilt of the surface is enough to detach a drop of probe liquid. In this work, we used ionic liquids as impregnation liquids due to their extremely low volatility which enhances the longevity of the impregnated surface. After a screening of a few selected ionic liquids, we found $[\text{C}_2\text{mim}][\text{MeSO}_4]$ to be the most suitable compound to repel even low surface tension liquids. A second, major requirement for a stable SLIPS system is a suitable coating of the substrate surface prior to impregnation in order to prevent replacement of the impregnation liquid with the probe liquid. For this purpose, we synthesised a coating compound that closely matches the surface tension of the impregnation liquid. The coating was then applied to silicon nanowire substrates prepared by using again silver-assisted etching. After impregnation with the ionic liquid, the resulting SLIPS was able to repel cyclohexane (roll-off angle: $1.8 \pm 1.2^\circ$) and toluene (roll-off angle: $5 \pm 0.5^\circ$) at minimal substrate tilting.

Zusammenfassung

The approved original version of this thesis is
available at the main library of the Vienna
University of Technology.

<http://www.ub.tuwien.ac.at>

In dieser Arbeit verfolgen wir zwei unterschiedliche, durch die Natur inspirierte Ansätze zur Herstellung von flüssigkeitsabweisenden Oberflächen, nämlich Cassie-Baxter und SLIPS (Slippery Liquid Infused Porous Surfaces) Systeme.

Cassie-Baxter Systeme sind in erster Linie durch den Lotus Effekt bekannt. Dabei führt eine Kombination von rauen Oberflächen mit gleichzeitig niedriger Oberflächenenergie zu superlyophoben Eigenschaften mit Kontaktwinkeln über 150° und einer Kontaktwinkelhysterese kleiner als 10° . Um solche Oberflächen nachzuahmen, haben wir Siliziumsubstrate verwendet, die durch silberkatalysiertes Ätzen vollständig mit aufrechtstehenden Siliziumnanodrähten bedeckt wurden. Die Oberflächen wurden dann mit einer kovalent gebundenen, Azid-terminierten Monoschicht versehen, die in weiterer Folge mit einem polyfluorierten Alkin in einer Huisgen 1,3-dipolaren Cycloaddition umgesetzt wurde, um eine niedrige Oberflächenenergie zu erreichen. Dadurch liegt eine modifizierte Monoschicht auf der Oberfläche vor und die präparierte Oberflächenstruktur bleibt erhalten, aber gleichzeitig können durch Variation des Alkins je nach Anforderung verschiedene Funktionalitäten an die Oberfläche gebunden werden. Auf den fertigen Oberflächen konnten wir sowohl mit Wasser ($168 \pm 3^\circ$) als auch mit Ethanol ($113 \pm 2^\circ$), das durch seine niedrigere Oberflächenspannung schwerer abweisbar ist, hohe Kontaktwinkel beobachten.

SLIPS Systeme, die in der Natur beispielsweise bei fleischfressenden Kannenpflanzen zum Fangen von Insekten vorkommen, bestehen allgemein aus porösen, mit Imprägnierflüssigkeit getränkten Oberflächen. Eine zweite, unmischbare Flüssigkeit, die mit dieser Anordnung in Kontakt kommt, interagiert dann lediglich mit der Imprägnierflüssigkeit aber nicht mit dem festen Substrat. Die mit SLIPS Systemen erreichbaren Kontaktwinkel liegen zwar deutlich unter denen von Cassie-Baxter Systemen, dafür zeichnen sie sich durch eine verschwindend geringe Kontaktwinkelhysterese aus, sodass ein Tropfen bereits bei minimaler Neigung des Substrats abzurinnen beginnt. In dieser Arbeit konzentrierten wir uns auf die Verwendung von ionischen Flüssigkeiten als Imprägnierflüssigkeiten, da diese schwer flüchtig sind und damit sehr langlebige Systeme möglich sind. Nach einigen Vorversuchen konnten wir mit $[C_2mim][MeSO_4]$ eine Imprägnierflüssigkeit finden, die selbst Flüssigkeiten mit niedriger Oberflächenspannung abweisen kann. Um ein stabiles SLIPS System darauf aufzubauen, haben wir eine genau auf die Eigenschaften der ionischen Flüssigkeit abgestimmte Beschichtung synthetisiert, und konnten diese auf silberkatalysiert geätztes Siliziumsubstrat aufbringen. Das fertige SLIPS System war in der Lage Tropfen von Cyclohexan ($1.8 \pm 1.2^\circ$) und Toluol ($5 \pm 0.5^\circ$) nur durch äußerst geringe Neigung abzurinnen zu lassen.

Table of Contents

The approved original version of this thesis is
available at the main library of the Vienna
University of Technology.

<http://www.ub.tuwien.ac.at>

Acknowledgments	V
Abstract	VI
Zusammenfassung	VII
Table of Contents	VIII
1 Introduction	1
2 Theory	9
2.1 Theoretical Background	9
2.1.1 Wetting Properties of Flat Surfaces	9
2.1.2 Solid Surface Energy Calculations.....	10
2.1.3 Wetting Properties of Rough Surfaces	12
2.1.4 Dynamic Contact Angle	20
2.1.5 Slippery Liquid Infused Porous Surfaces (SLIPS).....	22
2.1.6 Metal-assisted Etching of Silicon Nanowires.....	27
2.2 Principles of Measurements	30
2.2.1 Brewster Angle FTIR Transmission Spectroscopy.....	30
2.2.2 Ellipsometry.....	32
2.2.3 Contact Angle, Surface Tension and Interface Tension Goniometry	34
3 Experimental	37
3.1 Chemicals and Material	37
3.1.1 Synthesis of THFDP.....	37
3.1.2 Synthesis of [C ₃ mim]Cl	38
3.2 Sample Preparation	38
3.2.1 Cutting and Cleaning of Silicon Substrates.....	38
3.2.2 Etching of Silicon Nanowires	38
3.2.3 Surface Modification	39
3.2.4 Impregnation of SLIPS	39
3.3 Sample Characterization	39
3.3.1 FTIR.....	39
3.3.2 Ellipsometry.....	40
3.3.3 Optical Goniometry	41

3.3.4	SEM	42
3.3.5	NMR Spectroscopy	43
4	Results and Discussion	44
4.1	Cassie-Baxter Systems	44
4.1.1	Topography	44
4.1.1.1	Optimization of Hydrogen Peroxide Concentration	45
4.1.1.2	Optimization of Etching Duration	48
4.1.1.3	Determination of Silver and Hydrogen Peroxide Consumption	50
4.1.2	Coating	53
4.1.2.1	Covalent Coating of OTS and BUTS	55
4.1.2.2	Optimization of Sodium Azide Treatment	58
4.1.2.3	Synthesis of THFDP and Huisgen 1,3-Dipolar Cycloaddition	60
4.1.3	Wetting Properties of Cassie-Baxter Type Materials	62
4.1.3.1	Influence of Liquid Evaporation on Contact Angle Measurements	63
4.1.3.2	Contact Angle Raw Data	66
4.1.3.3	Surface Energy Calculation	71
4.1.3.4	Evaluation of Surface Properties	80
4.2	SLIPS Systems	81
4.2.1	Probe Liquid – General Considerations	81
4.2.2	Impregnation Liquid	82
4.2.2.1	Surface Tension Measurement of Selected Ionic Liquids	82
4.2.3	Coating	85
4.2.3.1	Synthesis and Covalent Coating of [C ₃ mim]Cl	86
4.2.4	Probe Liquid - Miscibility with [C ₂ mim][MeSO ₄]	89
4.2.5	Suitability Tests of Selected SLIPS Systems	90
4.2.6	Topography	94
4.2.7	Contact Angle Measurements of SLIPS Systems	95
5	Conclusion	99
6	References	102
7	List of Figures	106
8	List of Tables	110
9	List of Abbreviations	113
10	Curriculum Vitae	114



Die approbierte Originalversion dieser Dissertation ist in der Hauptbibliothek der Technischen Universität Wien aufgestellt und zugänglich.

<http://www.ub.tuwien.ac.at>



The approved original version of this thesis is available at the main library of the Vienna University of Technology.

<http://www.ub.tuwien.ac.at/eng>

1 Introduction

The approved original version of this thesis is
available at the main library of the Vienna
University of Technology.

<http://www.ub.tuwien.ac.at>

Wettability is a fascinating property. There are numerous cases in flora and fauna where only precisely adjusted wettability enables certain tasks to be fulfilled [1]. Yet they are often overlooked since their benefit may not be apparent on first sight.

Probably the most commonly given example in this regard is the leaf of the lotus plant [2]. Its hydrophobic properties allow raindrops to easily roll off the leaf and take dust particles with them in the process, leaving behind a clean surface which in turn enhances the efficiency for photosynthesis. Rice plants even bring this to the next level [3]. They have relatively narrow but elongated leaves. Anisotropic hydrophobic behaviour forces the drop to move along the whole leaf and prevents it from falling off prematurely. This ensures that each drop cleans a good portion of the leaf. Similarly wings of different insects like the cicada, flies, moths and many more also show self-cleaning properties [4-6]. Butterflies use again anisotropic wettability on their wings to guide water drops away from their body helping them to stay clean in wet environment [7, 8]. The use of specialized wettability in nature is, however, not confined to self-cleaning. For instance, water striders rely on their hydrophobic feet to keep them floating on water surfaces [9]. Namib desert beetle *Stenocara sp.* was reported to use a sophisticated arrangement of both hydrophobic and hydrophilic areas on its carapace to collect water from morning dew, guiding it directly into its mouth in an otherwise arid environment [10]. Also, plants like *Euphorbia Polychrome*, *Echeveria Schaviana*, *Echeveria Elegans* or *Alchemilla Mollis* use similar strategies to collect water [11].

In all these cases, it could be shown that in fact only two properties are required to control wettability. On one hand, the surface energy of the outermost layer largely defines the general regime in which the overall wettability will be. A low surface energy, due to a thin film of wax or even proteins, will result in hydrophobic behaviour. Accordingly, high surface energy will give hydrophilic surfaces. Roughness, on the other hand, enhances prevailing conditions and leads to more extreme behaviour. This works in both ways, ultimately resulting in superhydrophobic or superhydrophilic surfaces.

The most distinct way a combination of roughness and low surface energy can lead to hydrophobic behaviour is if the drop follows the so-called Cassie-Baxter wetting model [12]. Here, the drop only touches the substrate at the outermost part of the rough surface while air is trapped in the pores which enhances hydrophobicity leading to sphere-shaped drops. This behaviour can also be observed at home when for example watering indoor plants with already very dry soil or when

trying to wet a very dry kitchen sponge. However, in both these cases, as well as in a lot of cases in nature, the Cassie-Baxter state is only metastable.

A slightly more complex self-cleaning surface in nature can be found on snail shells [13] and fish scales [14]. In those examples the surface is hydrophilic. Thus, when in a wet environment, all pores are completely filled with water, forming a lubricant to repel oil drops, effectively resulting in an oleophobic surface. This not only keeps the surfaces clean from contaminants but also inhibits the attachment of algae or plankton. Pitcher plants, carnivorous plants, which feed on insects or even small mammals, use an analogous technique to capture their prey [15]. They possess a horn shaped trap which is oleophobic on the inside due to a lubricating water film. An insect sitting on its rim will inevitably slide down to the bottom, unable to crawl up due to the slippery surface or fly due to the constricted space and will be digested.

The wetting state in these examples, consisting of a completely wetted rough surface which is then able to repel other immiscible liquids, is known as slippery liquid infused porous surface (SLIPS) and represents the second group of hydrophobic surfaces [16]. Even though both, SLIPS and Cassie-Baxter states, repel liquids, drops behave fundamentally different in these two states. While drops in Cassie-Baxter states are remarkable because of their pronounced sphere-shape, SLIPS show flatter drops but they are much more mobile. A SLIPS surface only has to be tilted ever so slightly for the drop to start moving off the surface.

The versatile uses of surfaces with special wettability in nature is indeed compelling and exceeds the small selection of examples given here by far. Inspired by those, there is a multitude of possible applications where similar properties can be used advantageously. A few examples where wettability is of pivotal importance for industrial and commercial tasks are given in the following paragraphs.

Textiles are a prime example where self-cleaning properties are desirable [17]. Properly prepared hydrophobicity will prevent them from getting dirty in the first place when spilling liquid on them. Beyond that, growth of bacteria can be inhibited by oleophobicity to avoid smell [18]. There are already several commercial fabrics incorporating such properties but there is still room for improvement since the demands on the fabric in day to day use are quite high. They have to withstand high and low temperatures, direct sunlight and cleaning in washing machines, while maintaining colour and softness and being producible in a cost-efficient and environmentally friendly way.

Anti-freezing is another important issue for several applications. Layers of ice reduce the efficiency of refrigerators, air-conditioners, aircrafts and wind turbines. It could be shown that hydrophobic surfaces can tackle this problem on several fronts. First of all, it was reported that surfaces with low surface energy require higher supersaturation of water in air before nucleation of small water drops, enabling condensation, can take place [19]. Subsequent growth of ice is also slowed down by rough surfaces due to limited heat exchange between ice and substrate [20]. Beyond that, already formed ice on such a surface is attached much more loosely, facilitating its removal [21].

Corrosion is a major problem for modern economics and environment which can again be addressed with hydrophobic surfaces [22]. A significant part of current steel production is necessary just to replace defect parts. It was shown that hydrophobic and oleophobic surfaces are able to slow down the progression of corrosion by providing a film limiting the contact of the substrate with solvents or corrosive compounds and therefore inhibiting reactions. There are several approaches described, working not only for steel but also for aluminium [23], copper [24, 25], zinc [26] and nickel [27].

Optical devices can also profit from hydrophobic surfaces with self-cleaning properties [28]. Antireflective coatings are already commonly used on lenses. The best example for this are probably eye-glasses but also solar cells greatly benefit from the absence of reflections. By modifying the coatings to feature also hydrophobicity, dust can effectively be removed from their surface, further enhancing the performance. The primary limiting factor here is that the roughness only can be in the nanometre scale to not undermine the transparency of the device.

There are also reports about drag reduction of water on hydrophobic surfaces [29]. Due to reduced interactions between water and the substrate, water glides more easily over such surfaces. This can be advantageous for boats but also for pipe systems. It could be shown that the flow of water through hydrophobic pipes is improved in comparison to untreated pipes when using the same pressure.

Another field, where hydrophobic surfaces can be applied, is the separation of oil and water [30, 31]. When using a hydrophobic but oleophilic mesh, water will be repelled and cannot penetrate the mesh. For organic solvents on the other hand, the mesh will be no hindrance and they will pass right through it and can be collected separately. Similarly, when such a material is processed in form of an open-cell foam, it can also be used to absorb oil spills in water, since only oil can enter the sponge while water will be repelled.

Wettability is also an integral factor for bio-adhesion on surfaces [32]. Proteins tend to stick more easily to hydrophobic surfaces due to their commonly hydrophobic sidechains, whereas hydrophilic surfaces only lead to loosely bound proteins. The relation between adhesion and wettability can also be extended to whole cells. For medical application, the prevention of platelet adhesion, which is a main factor for blood coagulation, is of special importance. Hydrophobic surfaces on implants or other devices repelling platelets are reported to improve compatibility with blood in in-vitro tests [33]. A very different application making use of similar properties can be found in paint for ship hulls. Reduced algae growth on hulls extends the necessary interval for cleaning and repainting to avoid damage due to biofouling.

Properly controlled wettability can also be used in chemical catalysis. SILP (supported ionic liquid phases) can be used to immobilize a thin layer of ionic liquid on a porous surface submerged in another immiscible liquid [34]. If solubilities are well-adjusted, a catalyst then remains dissolved only in the ionic liquid, while the precursor and the product are mainly dissolved in the second liquid. The reaction happens then at the interface between those two, which is relatively large due to the porous nature of the substrate. With this method, reactions can be performed in columns for even higher yield without the need to covalently bind the catalyst and likely worsen its performance. Once a robust system is developed, it can then possibly be employed for all kind of catalysts showing suitable partition equilibria.

Besides the examples listed, which are already largely in commercial use, there are countless other options to exploit properly selected wettability. It can be used for aquatic vessels moving like water striders or lab-on-a-chip devices to move drops of samples over a surface with anisotropic or switchable wettability to the desired location. Basically, whenever a solid is in contact with a liquid, wettability is a major factor to tune the system properties.

For most of the applications listed above, Cassie-Baxter wetting is the instrument of choice to reach the desired properties. Thus, there has been put significant effort into mimicking nature and artificially producing rough surfaces with low surface energy, especially since it is more challenging to achieve hydrophobic than hydrophilic behaviour. The different approaches can best be classified in two groups, each with two subgroups.

First of all, there are top-down approaches. These summarize the machining of large pieces of flat, solid substrates into finer structures by using moulds, lasers or other tools to create surface roughness. This group can further be divided depending on the surface energy of the substrate. If materials with low surface energy are used to begin with, no additional modifications are then

necessary (Approach 1), otherwise a subsequent surface modification is required (Approach 2). Secondly, there are bottom-up methods. They include approaches where small building blocks spontaneously self-assemble to form well-organized larger structures. If the building blocks already show low surface energy, again no subsequent surface modification is necessary (Approach 3), otherwise a surface coating step must be added (Approach 4).

The four approaches have different advantages and limitations. Approach 1 uses bulk materials with low surface energy. This makes it most resistant to mechanical damage since scratches only uncover a surface with again low surface energy. In approach 2 to 4, the substrate can be chosen freely, but requires the addition of hydrophobic properties on top. The bulk can then be chosen to meet other requirements of a workpiece except for wettability.

Approach 1 and 3 directly use low surface energy material for producing roughness. This saves a step in the production process. It also reduces the number of different materials on the surface making the surface less susceptible to chemical or mechanical damage, since each interface or compound is potentially a soft spot. On the other hand, when separating the generation of roughness and the coating with a low surface energy substance, an independent optimization of those two steps is possible. An overview over the characteristics of the different approaches can be seen in Table 1.

	Approach 1	Approach 2	Approach 3	Approach 4
Substrate independent from wettability considerations	-	+	+	+
Mechanical and chemical stability	+	+/-	+/-	-
Roughness and surface energy independently optimizable	-	+	-	+
Minimal preparation steps	1	2	1	2
Different materials	1	2	2	3

Table 1: General characteristic of different preparation methods for Cassie-Baxter systems with + and - representing advantageous and disadvantageous behaviour, respectively. Approach 1: Top-down methods applied on low surface energy substrate; Approach 2: Top-down methods applied to any substrate with subsequent surface modification; Approach 3: Bottom-up methods using low surface energy building blocks; Approach 4: Bottom-up methods using any building blocks with subsequent surface modification.

There are numerous specific methods presented in literature to produce Cassie-Baxter systems according to one approach or the other. Basically, any method resulting in a rough surface is in theory suitable and can be combined at will with different methods to achieve low surface energy. Also, if the same general method was chosen by two authors, still they often differ strongly in the details. It is therefore not possible to present here an extensive list but only a few selected examples, most of them representing a common class of treatments.

As an example following approach 1, it was reported that lotus leaves can be used as templates [35]. First, a negative replica out of poly(dimethylsiloxane) was prepared and it was then again used as a mould to prepare a positive replica. It was found that the final cast showed similar hydrophobic behaviour as the original leaf. Another procedure employing approach 1 uses oxygen plasma treatment of polytetrafluoroethylene (PTFE) substrate [36]. This will create needle-like structures without significantly changing the surface composition. By altering the duration of the treatment, the length of the needles could be changed reaching 1 μm after 300 s.

Methods following approach 2 often use anisotropic etching. A prime example for anisotropic etching is photolithography. For example, x-ray lithography was used to create regular patterns of spikes on a silicon wafer [37]. Subsequent sputtering with gold and treatment with hexadecane thiol could then create a rough, low energy hydrocarbon surface.

Assemblies from colloidal solutions can be used to produce surfaces according to approach 3. Low surface energy silica spheres could be produced by using tetraethoxysilane in a sol-gel process and later adding 1H,1H,2H,2H-perfluorodecyltriethoxysilane to the mixture for surface modification [38]. These beads could then be applied to glass slides via spin-coating to obtain hydrophobic surfaces.

Chemical bath deposition can be employed to reach Cassie-Baxter states according to approach 4. It was reported that a solution of CoCl_2 and NH_2CO can be used to deposit $\text{Co}(\text{OH})_2$ on glass slides [39]. Under the chosen conditions, growth of ordered single crystals occurred, showing mostly upwards facing spikes. The needles with a diameter of only about 6.5 nm were then coated with lauric acid, which gave strong hydrophobic properties. Another quite unusual procedure falling in this category is the treatment of a glass slide with candle soot [40]. In this work, the fractal-like structure of nanospheres present in soot was reinforced with tetraethoxysilane in a chemical vapor deposition process. Then the original nanospheres were removed in a calcination step and the surface was coated with a polyfluorinated silane leaving a transparent surface with exceptional liquid-repelling properties.

In addition to using only a single approach, some authors also combine a top-down method with a bottom-up method to achieve hierarchically structured surfaces [41]. These surfaces typically show roughness with large features, each of which is then covered again by a rough surface with features several orders of magnitude smaller. They are known to show even better liquid repellent properties but are significantly more laborious to produce. The best liquid repellent behaviour currently known, can be achieved with surfaces featuring overhanging structures forming

mushroom-like shapes [42]. However, these formations can virtually exclusively be produced with highly elaborate photolithography methods and are therefore not applicable to large areas.

SLIPS systems, like Cassie-Baxter systems, as well need rough surfaces and control over surface energy. Therefore, in principal, the same four approaches described for Cassie-Baxter systems are also applicable to them. The two main difference here are, first, that the particular shape of the rough surface only plays a minor role. Its main purpose is to act as a reservoir for the lubricating impregnation liquid. Secondly, also the surface energy must not be as low as possible, but it has to be adjusted precisely to the impregnation liquid, to allow the impregnation liquid to completely wet the surface regardless of other parameters. The impregnation liquid itself should have low volatility and should be immiscible with as many probe liquids as possible, since immiscibility is a basic requirement for a stable system.

To give an example of a SLIPS system described in literature, it was reported that a combination of photolithography and wet-chemical etching can be used to create a hierarchically structured silicon substrate [43]. The surface was then coated with a perfluorinated silane and wetted by a spin-coating process with a perfluoropolyether (DuPont Krytox) to ensure a homogeneous thin film of the lubricant. Krytox is known to be immiscible with both aqueous as well as several non-aqueous solvents. The resulting surface could then repel several liquids like water but also ethanol or heptane. Other authors used photolithography in addition to two different plasma etching steps to create hierarchically structured surface morphologies on silicon wafers [44]. They then applied a coating of trichloro(octadecyl)silane (OTS) in solution and dipped the samples either in a silicon oil or in an ionic liquid (1-butyl-3-methylimidazolium bis(trifluoromethylsulfonyl) imide) and removed it slowly to retain only a thin film on the surface. These surfaces were then able to easily repel drops of water.

In this work, we focused first on the preparation of Cassie-Baxter systems as liquid-repellent model surfaces based on silicon as substrate material. Silicon is available in high purity at moderate prices and is, due to its leading role in semiconductor industry, one of the best studied substrate materials. Silicon can not only be coated with a wide range of different compounds based on the well-established trichlorosilane or trialkoxysilane surface coupling technique [45], it can also be morphologically modified by a wide variety of different techniques [46]. In this work, a metal-assisted wet-chemical etching technique was employed, which uses metal particles precipitated on the surface to catalyse anisotropic etching [47], following the previously described approach 2, which arguably combines the most advantages. Metal-assisted etching in combination with alkylsilane surface modification was already used before for the preparation of Cassie-Baxter

systems [48]. However, we wanted to develop a method to coat such surfaces in a two-step process, in which the first step provides a monolayer of a covalently bound precursor which can then further be transferred into any desired functionality using in-situ surface coupling reactions. This should provide a toolbox for easy and versatile surface modification and, in our case, allow us to vary surface energies while maintaining the morphology of the substrate.

Beyond that, we also wanted to prepare SLIPS systems representing a more specialized approach to liquid repellent behaviour. As substrates, we also wanted to employ silicon wafers treated by metal-assisted etching for the same reasons mentioned above. The main point distinguishing our work from existing research should be the chemistry of the impregnation liquid and the coating used. Whereas most SLIPS systems described in literature to date are based on fluorinated impregnation liquids and surface modifications, we wanted to explore a new class of impregnation liquids – ionic liquids. They fulfil the requirements of low volatility and low miscibility with many other liquids. Ionic liquids have the additional advantage that their physical properties can be tuned over a wide range by varying their chemical composition, which should allow better fine-tuning of the liquid-repellent properties of the final SLIPS system than with any other impregnation liquid. Surprisingly, only few reports can be found in literature using ionic liquids as impregnation liquids for SLIPS [49].

2 Theory

The approved original version of this thesis is
available at the main library of the Vienna
University of Technology.

<http://www.ub.tuwien.ac.at>

2.1 Theoretical Background

2.1.1 Wetting Properties of Flat Surfaces

The main property to distinguish between wetting and non-wetting behaviour is the contact angle. It was discovered by Thomas Young in the early 19th century that the contact angle (θ) is defined by the balance of three different forces (Figure 1), the surface energy of solid substrate (γ_s), the surface tension of the involved liquid (γ_l) and the interface energy between those two phases (γ_{sl}), resulting in the Young equation [50] (Equation 1). The static contact angle in equilibrium on a flat surface is therefore also often referred to as ‘Young angle’.

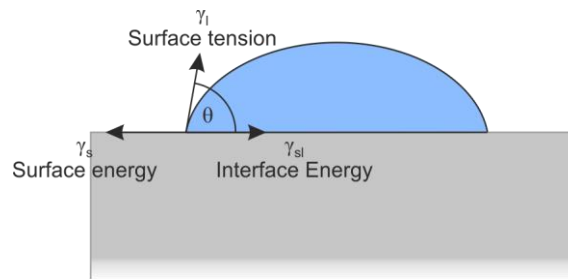


Figure 1: Involved forces at the boundary of a drop according to Young.

$$\cos\theta = \frac{\gamma_s - \gamma_{sl}}{\gamma_l} \quad (1)$$

Two of the variables occurring in this equation are readily accessible, the surface tension of the liquid with pendant drop measurements as well as the contact angle using a goniometer, the other two terms are not directly measurable. In order to be able to solve this equation, an approximation for one of the two, usually the interface tension, is necessary. There are several different ways to do so. The first attempt was made by Berthelot in the late 19th century stating that the interfacial cohesion work is equal the geometric mean of the cohesion work of the solid and the cohesion work of the liquid.

$$W_{sl} = \sqrt{W_s W_l} \quad (2)$$

The cohesion work in general is thereby the work per area necessary to split the material apart. When splitting one compound in half, this means that is necessary to expend twice the surface energy or surface tension since two new areas of the same size are created. When separating two different phases, one new area for each compound is formed and simultaneously the interface tension is lost. This can be seen in Equation 3, 4 and 5.

$$W_s = 2\gamma_s \quad (3)$$

$$W_l = 2\gamma_l \quad (4)$$

$$W_{sl} = \gamma_s + \gamma_l - \gamma_{sl} \quad (5)$$

When Equation 2, 3, 4 and 5 are then combined, the Berthelot hypothesis is formed (Equation 6).

$$\gamma_{sl} = \gamma_s + \gamma_l - 2\sqrt{\gamma_s \gamma_l} \quad (6)$$

Fowkes later refined the basic idea how the surface energy is formed [51, 52]. He assumed that the total surface energy is the sum of different kind of interactions, being dispersive, hydrogen bonds, acid-base, polar and induction.

$$\gamma = \gamma^d + \gamma^h + \gamma^{ab} + \gamma^p + \gamma^i \quad (7)$$

Dispersive interactions mainly account for London interactions, which are the spontaneous formation and attraction of dipoles in atoms. Thus, they are ubiquitous in all solids and liquids. The other terms, since they can all be associated with polar interactions, were later combined by Owens, Wendt, Kaelble and Rabel into a single parameter [53-55] (Equation 8). Analogous to the Berthelot hypothesis, they then used the geometric mean of the dispersive and polar components to form the OWKR approximation (Equation 9).

$$\gamma = \gamma^d + \gamma^p \quad (8)$$

$$\gamma_{sl} = \gamma_s + \gamma_l - 2 \left(\sqrt{\gamma_s^d \gamma_l^d} + \sqrt{\gamma_s^p \gamma_l^p} \right) \quad (9)$$

For interfaces where only a single kind of interactions can be found, the omnipresent dispersive interactions, the simpler Berthelot hypothesis is equivalent with the OWKR approximation, otherwise the OWKR approximation is more reliable. When using any of the two presented approaches to approximate γ_{sl} in Equation 1, it can be seen that only the surface tension of the liquid and the surface energy of the substrate influence the final contact angle. In order to achieve liquid repellent behaviour, a high surface tension and a low surface energy is necessary.

2.1.2 Solid Surface Energy Calculations

While there are several methods to calculate the surface energy of a solid, only two are presented here, which are also being used in this work. A good overview about multiple different methods was recently presented by Zenkiewicz [56]. The first one discussed here, is the Owens-Wendt

approach based on their approximation for γ_{sl} made in Equation 9. When applying it on Equation 1, Equation 10 can be obtained.

$$\cos\theta = \frac{2\left(\sqrt{\gamma_l^d \gamma_s^d} + \sqrt{\gamma_l^p \gamma_s^p}\right)}{\gamma_l^d + \gamma_l^p} - 1 \quad (10)$$

The variables in this equation are the polar and dispersive share of the surface energy, the polar and dispersive share of the surface tension and the contact angle. In order to use this equation for the determination of the surface energy, the contact angle of two different probe liquids on the surface has to be measured. Furthermore, the polar and dispersive share of the probe liquids has to be known. Only then a solvable system of equations can be established with only two unknown variables, the polar and dispersive share of the surface energy, and two equations, one for each probe liquid. The two equations can then be combined and solved for these variables as shown in Equation 11 and 12.

$$\gamma_s^d = \left(\frac{\sqrt{\gamma_{l,2}^p \gamma_{l,1} (1 + \cos\theta_1)} - \sqrt{\gamma_{l,1}^p \gamma_{l,2} (1 + \cos\theta_2)}}{2\left(\sqrt{\gamma_{l,1}^d \gamma_{l,2}^p} - \sqrt{\gamma_{l,1}^p \gamma_{l,2}^d}\right)} \right)^2 \quad (11)$$

$$\gamma_s^p = \left(\frac{\sqrt{\gamma_{l,2}^d \gamma_{l,1} (1 + \cos\theta_1)} - \sqrt{\gamma_{l,1}^d \gamma_{l,2} (1 + \cos\theta_2)}}{2\left(\sqrt{\gamma_{l,1}^p \gamma_{l,2}^d} - \sqrt{\gamma_{l,1}^d \gamma_{l,2}^p}\right)} \right)^2 \quad (12)$$

This method works best if the ratio between polar and dispersive components of the two involved liquids are as different as possible, since otherwise the denominator in the equations becomes close to zero, leading to high errors. Also, the liquids should be chosen to avoid contact angles close to 0° or 180° since these extreme contact angles cannot be determined precisely.

The second method presented here, is the so-called Zisman plot. The goal of this method is to extrapolate the surface tension to the point where the contact angle exactly becomes 0° . At this point, $\cos\theta$ in the Young equation (Equation 1) becomes 1 and the equation can thus be rewritten as Equation 13.

$$\gamma_s = \gamma_{sl} + \gamma_l \quad (13)$$

γ_l is then known from the extrapolation but, generally, γ_{sl} is unknown. However, γ_{sl} has to be always positive. This means, in any case, this method allows at least the determination of a lower limit of the surface energy of the solid.

Under certain conditions, more information can be retrieved. If the surface energy and the surface tension is defined completely only by dispersive interaction at the point where the contact angle is 0° , the Berthelot hypothesis (Equation 6) is applicable to approximate γ_{sl} there. When replacing γ_{sl} with the corresponding terms in Equation 13 and simplifying, it can be shown that Equation 14 can be obtained.

$$\gamma_s = \gamma_l \quad (14)$$

From Equation 13 and Equation 14 can be seen that as long as the Berthelot hypothesis is applicable at the point where the contact angle is 0° , γ_{sl} has to be zero and knowledge of the extrapolated surface tension alone is enough to determine the surface energy of the solid.

In order to apply the whole method, it is necessary to obtain the surface tension of a probe liquid which would resulting in a contact angle of 0° . This is usually done by measuring the contact angle as a function of the surface tension with subsequent extrapolation. If possible, usually the whole experimental set-up is chosen to fulfil the Berthelot hypothesis at any point. This, on one hand, ensures that the Berthelot hypothesis is fulfilled at the only relevant point for the calculation, where the contact angle is 0° , but it also allows easier extrapolation. It is then possible to apply the Berthelot hypothesis to the Young equation and use the resulting Equation 15 to fit all obtained data. This way a linear relation is expected when plotting $\cos\theta$ against $\frac{2}{\sqrt{\gamma_l}}$ with the slope $\sqrt{\gamma_s}$.

$$\cos\theta = 2 \sqrt{\frac{\gamma_s}{\gamma_l}} - 1 \quad (15)$$

If the Berthelot hypothesis is not suitable for the whole system, $\cos\theta$ is usually plotted against γ_l in combination with any fit representing the data properly. It has to be stressed again, that for a precise determination of the surface energy, the Berthelot hypothesis still has to be valid at the point where the contact angle becomes 0° . Otherwise γ_{sl} is greater than 0 at this point and, according to Equation 13, only a lower limit for the surface energy can be determined.

2.1.3 Wetting Properties of Rough Surfaces

The compound with the lowest surface energy currently known and therefore best suited to repel liquids is $C_{20}F_{42}$, having a surface energy of 6.7 mJ/m^2 [57]. However, when looking at different common organic solvents and calculating their contact angle on $C_{20}F_{42}$ using Equation 1 and 6, it becomes evident that not even this compound is capable to reach particularly high contact angles (Table 2).

	γ (mJ/m ²)	γ^p (mJ/m ²)	γ^d (mJ/m ²)	θ (°)	Ref.
Water	72.8	51.0	21.8	113.2	[58]
Nitromethane	36.8	16.5	20.3	98.4	[58]
Benzene	28.4	1.7	26.7	91.6	[59]
Toluene	28.4	2.3	26.1	91.6	[59]
Chloroform	27.2	2.3	24.8	90.4	[58]
1-octanol	26.7	5.4	21.3	89.9	[59]
Dichloromethane	26.5	3.3	23.2	89.7	[58]
Ethanol	22.3	3.3	19.0	84.5	[60]

Table 2: Total, polar and dispersive surface tension of different liquids and calculated contact angle on a flat C₂₀F₄₂ surface using the Young equation.

To further enhance the liquid repellent properties of a substrate, roughness can be introduced. When examining the behaviour of a liquid drop on such a surface, three different states can be observed. In the Wenzel state [61] (Figure 2) the liquid penetrates the pores of the substrate. The contact area between the liquid and the substrate is therefore extended by the roughness (r).

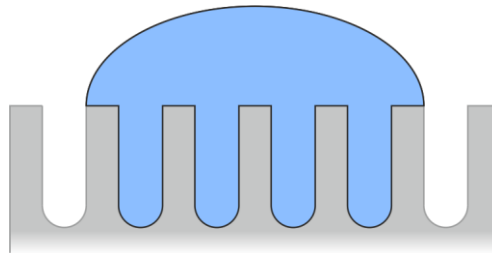


Figure 2: Wenzel wetting state.

The same is true for the contact area between substrate and surrounding. The roughness is thereby defined as the actual surface area divided by the projected geometric area. It must therefore always be equal to or greater than 1. The contact angle in this state can be described with a modified Young equation (Equation 1) where γ_s and γ_{sl} have to be multiplied with the factor r to account for the increased interface area (Equation 16).

$$\cos\theta^* = \frac{r\gamma_s - r\gamma_{sl}}{\gamma_l} \quad (16)$$

When comparing the contact angle of a flat and a rough Wenzel-state substrate, it can be seen that at a flat contact angle of 90° also the rough contact angle has to be 90°. However, small deviations from 90° lead to significantly bigger deviations on the rough substrate (Figure 3).

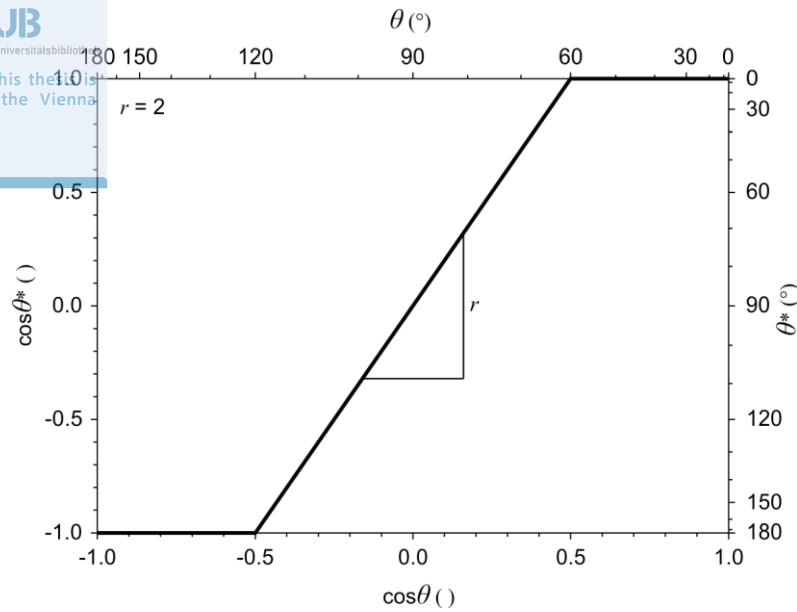


Figure 3: Calculated rough contact angles as a function of the flat contact angle according to the Wenzel state.

Another possible behaviour is according to the Cassie-Baxter model [12]. Here the drop only touches the tips of the rough surface but the inside of the pores stays dry (Figure 4). At the area between the drop and the rough surface as a whole, the drop is then only partly in contact with the solid but also with the surrounding. The cosine of the rough contact angle can then be expressed as the weighted arithmetic mean of the cosine of the contact angle to the substrate and to the surrounding (Equation 17). The weighting factor (ϕ) is here defined by the solid fraction at the interface.

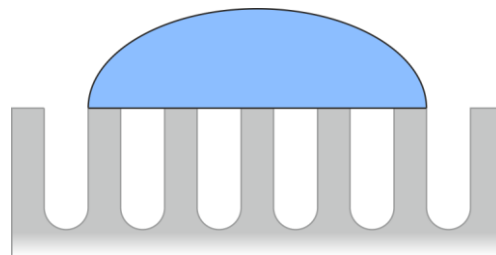


Figure 4: Cassie-Baxter wetting state.

$$\cos\theta^* = \phi \cos\theta_s + (1 - \phi)\cos\theta_{pores} \quad (17)$$

However, if the surrounding is gaseous, the contact angle θ_{pores} will be always 180° since liquids cannot wet gases. The contact angle of a drop in the Cassie-Baxter state will therefore always be higher than on a flat substrate (Figure 5).

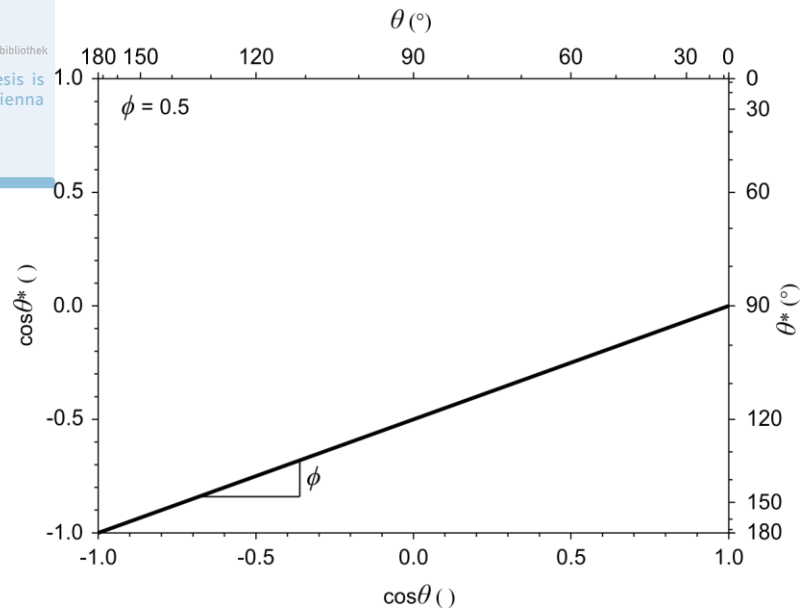


Figure 5: Calculated rough contact angle as a function of the flat contact angle according to the Cassie-Baxter state.

Similar to the Cassie-Baxter state is the impregnated Cassie-Baxter state (Figure 6). In this case, the pores are not filled with air but with the probe liquid itself. The same thoughts also apply here but with the difference that a liquid will always completely wet itself completely and therefore θ_{pores} will be 0° in this case (Equation 17, Figure 7).

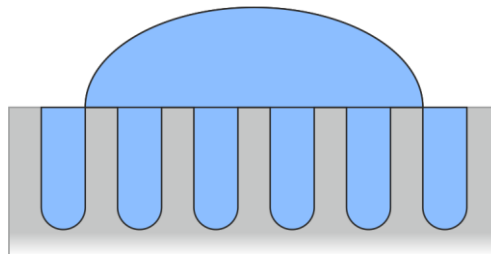


Figure 6: Impregnated Cassie-Baxter wetting state.

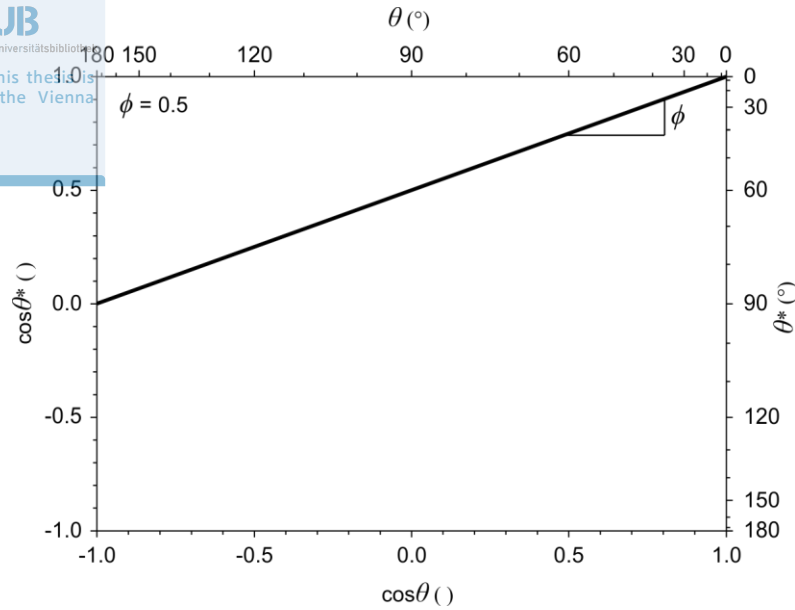


Figure 7: Calculated rough contact angle as a function of the flat contact angle according to the impregnated Cassie-Baxter state.

In order to understand which state is the most stable under different conditions, surface impregnation has to be discussed. When an impregnated surface is extended by a small amount (dx), the energy of the system changes with the amount of newly formed and lost interface times the energy of the interface (Equation 18). In this case, the surface area inside of the pores ($r - \phi$) will be covered with liquid instead of being dry ($\gamma_{sl} - \gamma_s$) and the liquid filling the pores will expose the newly formed liquid surface area ($1 - \phi$) to the surrounding (γ_l).

$$dE = (r - \phi) (\gamma_{sl} - \gamma_s) dx + (1 - \phi) \gamma_l dx \quad (18)$$

If the energy change is below 0, a completely impregnated surface is the most stable configuration since then the expansion of the impregnated area will always stabilize the system. This is true if Inequation 19 is fulfilled.

$$\cos \theta > \frac{1 - \phi}{r - \phi} \quad (19)$$

Since Cassie-Baxter and Wenzel state require dry pores, at least outside of the contact area, they cannot be the thermodynamically stable states beyond this point. The only model for which the requirements are then met, which then also must be the thermodynamically stable one, is the impregnated Cassie-Baxter model. With the same argument, it can be concluded that below this point only Cassie-Baxter and Wenzel can potentially be thermodynamically stable.

To further distinguish between Cassie-Baxter and Wenzel, the total energy of a drop being placed on a rough surface has to be established for both systems, respectively. It is thereby assumed that

the drop is relatively small, so that deformation due to gravity can be neglected. The drop will then form a spherical cap. Moreover, the volume of the drop should be the same for both systems. The amount of liquid inside the pores in the Wenzel state will be neglected for this purpose, since it is assumed that is very small in comparison to the total volume of the drop. For Cassie-Baxter, the calculated energy can be seen in Equation 20 with S being the outer surface of the spherical cap and C being the contact area between drop and substrate.

$$E_{CB} = S_{CB}\gamma_l + C_{CB}\phi\gamma_{sl} + C_{CB}(1 - \phi)\gamma_l - C_{CB}\phi\gamma_s \quad (20)$$

By using the Young equation as well as Equation 17, it can be simplified to Equation 21.

$$E_{CB} = \gamma_l(S_{CB} - C_{CB}\cos\theta_{CB}) \quad (21)$$

In a similar manner, the energy of a drop in the Wenzel state (Equation 22) can be simplified by using the Young equation and Equation 16 to obtain Equation 23.

$$E_W = S_W\gamma_l + C_W r\gamma_{sl} - C_W r\gamma_s \quad (22)$$

$$E_W = \gamma_l(S_W - C_W\cos\theta_W) \quad (23)$$

S and C can be expressed as a function of only the drop volume V and the contact angle θ .

$$S = (2 - 2\cos\theta)^3 \sqrt{\frac{9V^2\pi}{(\cos^3\theta - 3\cos\theta + 2)^2}} \quad (24)$$

$$C = \sin^2\theta^3 \sqrt{\frac{9V^2\pi}{(\cos^3\theta - 3\cos\theta + 2)^2}} \quad (25)$$

Since Equation 21 and 23 only differ in their respective indices, insertion of Equations 24 and 25 can be done in a more general approach with $x = CB$ or W leading to Equations 26 and, after some simplification, Equation 27.

$$E_x = \gamma_l^3 \sqrt{\frac{9V^2\pi}{(\cos^3\theta_x - 3\cos\theta_x + 2)^2}} (2 - 2\cos\theta_x - \sin^2\theta_x \cos\theta_x) \quad (26)$$

$$E_x = \gamma_l^3 \sqrt{9V^2\pi} \sqrt{\cos^3\theta_x - 3\cos\theta_x + 2} \quad (27)$$

Inequation 28, which assesses the stability range of the two states, can then be rewritten as Inequation 29 by using Equation 27 and eliminating identical terms.

$$E_{CB} > E_W \quad (28)$$

$$\sqrt[3]{\cos^3 \theta_{CB} - 3\cos\theta_{CB} + 2} > \sqrt[3]{\cos^3 \theta_W - 3\cos\theta_W + 2} \quad (29)$$

Since the function $f(k) = \sqrt[3]{k^3 - 3k + 2}$ is monotonically decreasing between -1 and 1, it can be concluded that in order for Inequation 28 and 29 to be true, Inequation 30 has to be fulfilled.

$$\cos\theta_{CB} < \cos\theta_W \quad (30)$$

This then results in the following representation of the most stable state in green as a function of $\cos\theta$.

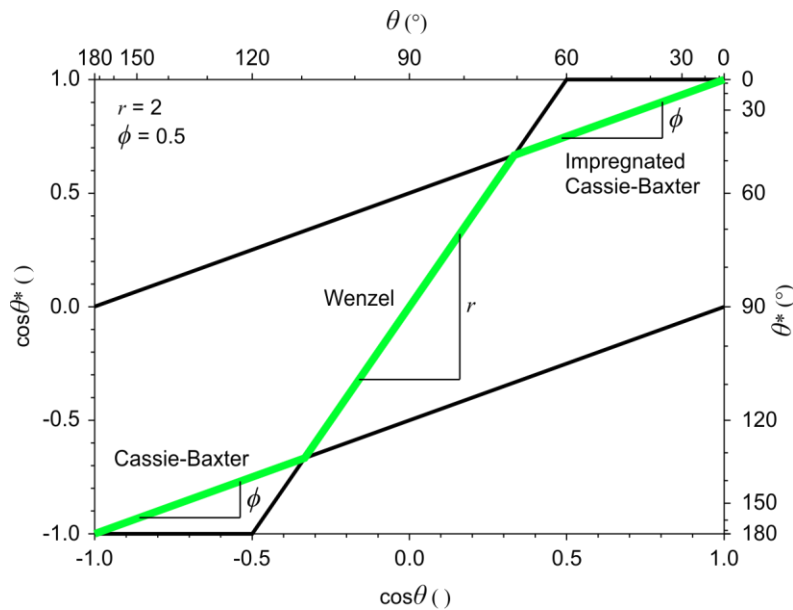


Figure 8: Representation of the most stable wetting state on a rough surface (green) superimposed on calculated rough contact angles according to the Cassie-Baxter, Wenzel and impregnated Cassie-Baxter state (black).

But it is not only necessary to discuss the thermodynamic stable state, also metastable states are of importance. For the purpose of liquid repellent surfaces, this is especially true for the metastable extension of the Cassie-Baxter state. When the Cassie-Baxter state collapses, the liquid moves down into the pores and, as soon as the pores are completely filled, the Wenzel state is reached. The most unstable transition state during this process is when the side walls of the pores are already wetted but at the bottom of the pores still a thin layer of atmosphere remains (Figure 9).

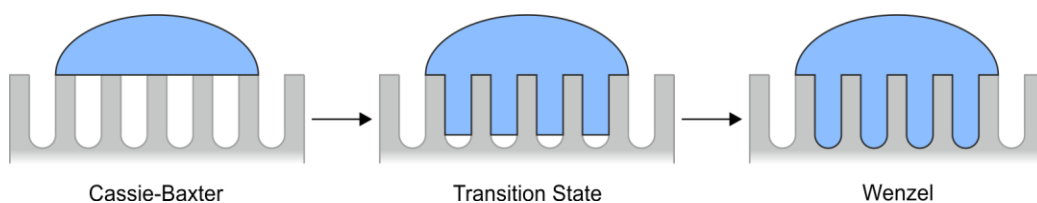


Figure 9: Representation of the collapse of the Cassie-Baxter state and transition to the Wenzel state.

To calculate the energy of the transition state, it is easiest to just modify the energy of the Cassie-Baxter state. Since in this process the overall drop shape stays the same, when again neglecting the volume of liquid entering the pores, the contact area between the drop and the surface as well as the outer surface of the drop is the same for the Cassie-Baxter state and the transition state ($C = C_{CB} = C_{TS}$; $S = S_{CB} = S_{TS}$). The energy of the transition state can then be calculated by replacing the surface energy of the side walls of the pores with the interface energy between liquid and solid, as can be seen in Equation 31.

$$E_{TS} = E_{CB} + C(r - 1)(\gamma_{sl} - \gamma_s) \quad (31)$$

As long as this transition state is energetically unfavourable in comparison to the Cassie-Baxter state, a metastable Cassie-Baxter state may exist (Inequation 32).

$$E_{TS} > E_{CB} \quad (32)$$

Equation 31 and Inequation 32 can then be summarized to Inequation 33.

$$C(r - 1)(\gamma_{sl} - \gamma_s) > 0 \quad (33)$$

Here C and $(r - 1)$ are always positive, however the term $(\gamma_{sl} - \gamma_s)$ is only positive as long as Inequation 34 is true.

$$\gamma_{sl} > \gamma_s \quad (34)$$

When putting the OWKR hypothesis (Equation 9) in Inequation 34, Inequation 35 can be formed.

$$\gamma_l > 2 \left(\sqrt{\gamma_s^d \gamma_l^d} + \sqrt{\gamma_s^p \gamma_l^p} \right) \quad (35)$$

It can then be further combined with Equation 10 leading to Inequation 36.

$$\cos\theta < 0 \quad (36)$$

In conclusion, a metastable Cassie-Baxter state is only possible if the contact angle of a liquid on a flat surface is above 90° . Additionally, judging from Equation 31, the energy difference between the transition state and the Cassie-Baxter state can be enhanced by increasing the roughness.

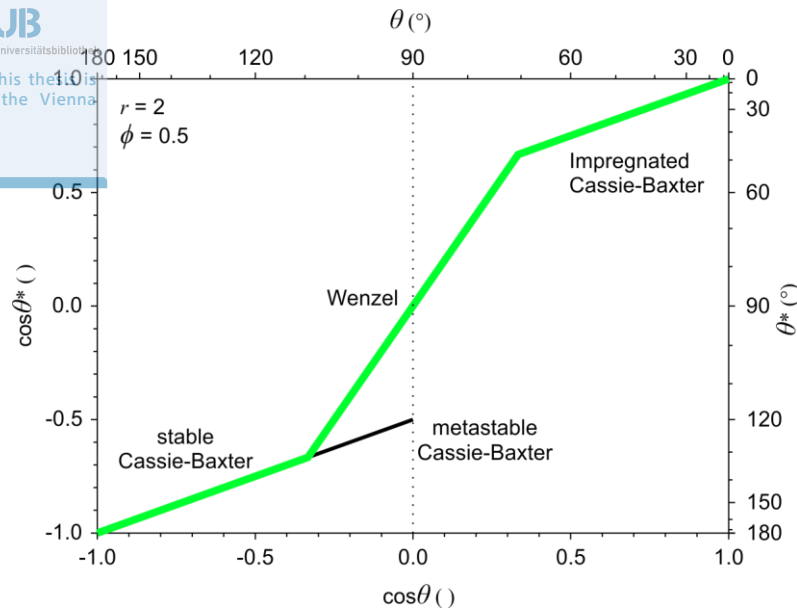


Figure 10: Contact angles of thermodynamic stable states (green) and metastable Cassie-Baxter state (black) on rough surfaces as a function of the flat contact angle.

2.1.4 Dynamic Contact Angle

Besides the static contact angle, which is the contact angle in equilibrium, also the dynamic contact angle has to be discussed. When slowly tilting a surface with a drop on it, the liquid will follow gravity and flow to the lower side of the drop. At the beginning, the position of the contact area between the drop and the substrate will not change. Consequently, the contact angle on the lower side will increase, while on the other end the angle will decrease. This will continue until a critical angle on both sides is exceeded at which point the drop as a whole will begin to move and roll off of the surface. At this point, the tilt of the samples relative to a horizontal plane is called roll-off angle. The deviations from the static contact angle during this process are metastable and are due to activation energy necessary prohibiting reach of equilibrium. The main reason that there is an activation energy, which has to be overcome before a drop can roll-off, can be explained with surface roughness. As an example, a drop in the Cassie-Baxter state is shown in Figure 11.

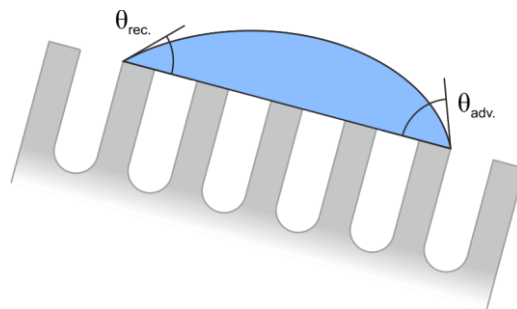


Figure 11: Advancing and receding contact angle in the Cassie-Baxter state.

According to the Cassie-Baxter state, the drop touches only the tips of the substrate. This state was explained in 2.1.3 as a combination of contact area to the surrounding at the interface, which has to show a contact angle of 180° , and contact area to the substrate, which shows a lower contact angle. This results in a macroscopically observed contact angle somewhere in between (Equation 17). Since the macroscopically observed contact angle is smaller than the contact angle to the surrounding, all gaps at the interface destabilize the interface area. Analogously, the contact between drop and substrate stabilize the interface area, perfectly offsetting the destabilizing effect at the equilibrium. Due to its stabilizing effect, the drop will always touch substrate at its rim. When tilting the substrate, as in Figure 11, the drop will not move in the beginning on neither side but the macroscopically contact angle on the left side will decrease, while the contact angle on the right side will increase. On the left side, the drop will only start to move if the current, metastable and macroscopically observable contact angle becomes smaller than the equilibrium contact angle to flat substrate (θ_s in Equation 17). On the right side, the drop will start moving when the current contact angle there becomes large enough that the drop overhangs the last column it touches to such a degree that any point of the drop contour comes in touch with the next, formerly dry, column. Then, due to its stabilizing properties, the drop will immediately wet the whole tip of the column.

The same behaviour can be seen in the Wenzel state (Figure 12), which is the most stable state at static contact angles of around 90° on flat substrate (θ_s). In order for the drop to move the right border, it has to wet formerly dry pores on the right first by moving downwards along the column. On the sidewall of the column, however, the contact angle is locally much smaller than the desired contact angle of about 90° . The penetration and therefore the movement of the drop are here again inhibited and even to a much higher degree than it is the case in the Cassie-Baxter state. Similarly, before moving on the left side, the liquid has to leave the pore even though the local contact angle on the vertical wall of the pore is much larger than the equilibrium contact angle to flat substrate (θ_s).

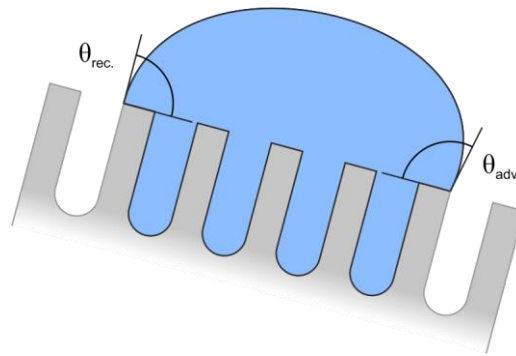


Figure 12: Advancing and receding contact angle in the Wenzel state.

The most extreme deviations from the static contact angle, at which point the metastable state collapses and the drop begins to move, are called advancing angle on the right side of the drop in Figure 11 and Figure 12 and receding angle on the left side. The difference between those two angles is known as hysteresis. In both presented models, roughness causes the hysteresis. On solid surfaces, the existence of a hysteresis is therefore an omnipresent phenomenon, since, even if not introduced by design, a certain degree of roughness originating from grain boundaries, scratches, crystallographic defects or at least on an atomic level cannot be avoided. The hysteresis is also influenced by the energy difference between stabilizing and destabilizing area. This means a drop in the Cassie-Baxter state showing a contact angle close to 180° will inherently have a lower hysteresis than one with low contact angle.

2.1.5 Slippery Liquid Infused Porous Surfaces (SLIPS)

Besides reaching high contact angles, another design goal for liquid repellent surfaces can be to achieve roll-off angle as small as possible. According to 2.1.4, this requires a surface as flat as possible, but as a consequence high contact angles can no longer be obtained since there is then no roughness enabling the Cassie-Baxter state. However, it is difficult and tedious work to produce completely flat solid surfaces without any defects and for thermodynamic reasons they will not stay clean and defect free for long in most applications. Liquids inherently do not have these problems. The mobility of the molecules in combination with gravity levels the surface after each distortion immediately. However, liquids cannot be shaped at will without an outer container, rendering their surface properties largely unusable for workpieces requiring tilted surfaces.

SLIPS (Figure 13) try to combine the strengths of both aggregate states. The idea is here to use a rough, solid substrate which is completely wetted with an impregnation liquid (teal). Capillary forces keep this liquid in place so that it cannot flow off. When a probe liquid (blue) comes in contact with this arrangement, only the properties of the liquid-liquid interface have to be considered for wetting purposes, while the underlying solid substrate can be shaped as desired. The surface

Surface tension of the impregnation liquid will be abbreviated as γ_i in this work and interface tensions follow the already introduced scheme.

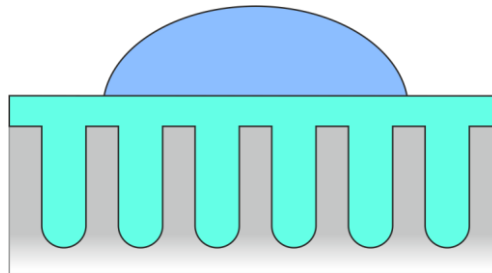


Figure 13: SLIPS scheme.

There are numerous conditions to be met for such a system to be stable. First and foremost, the two liquids must not be miscible. Additionally, the energies of different possible arrangements have to be compared to find conditions favouring the state presented in Figure 13. This can be done by separating the model in three regions (Figure 14).

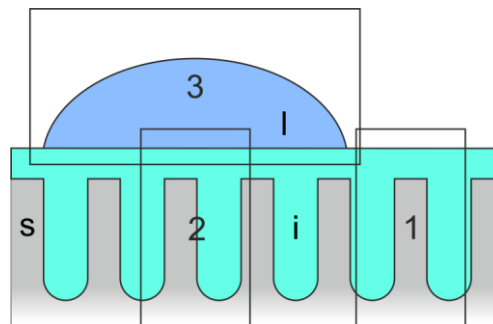


Figure 14: SLIPS regions for stability considerations.

Each region can be considered separately. Region 1 (Figure 15) describes the part without probe liquid on top. There, the impregnation-liquid can completely wet the pores and the tips (1A) but it can also just wet the pores with dry tips (1B) or it can completely flow off so that only a dry surface remains (1C). A Cassie-Baxter state is also an imaginable option (1D).

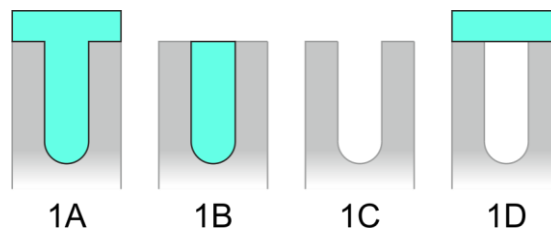


Figure 15: Different possible wetting states in region 1.

To calculate the energies of the different states, the surface energy, interface energy and surface tension has to be multiplied with the amount of the respective surface present (Equation 37, 38, 39

and 40). r represents again the roughness and ϕ the solid fraction of the outer surface as introduced in 2.1.3.

$$E_{1A} = r\gamma_{si} + \gamma_i \quad (37)$$

$$E_{1B} = (r - \phi)\gamma_{si} + (1 - \phi)\gamma_i + \phi\gamma_s \quad (38)$$

$$E_{1C} = r\gamma_s \quad (39)$$

$$E_{1D} = (r - \phi)\gamma_s + (2 - \phi)\gamma_i + \phi\gamma_{si} \quad (40)$$

These energies can be compared by forming inequations to find the thermodynamically most stable state. Conveniently, all formed inequations can be easily rewritten to express $\frac{\gamma_s - \gamma_{si}}{\gamma_i}$ on one side. The results of the individual inequations are shown in Figure 16A as well as the most stable states as a function of $\frac{\gamma_s - \gamma_{si}}{\gamma_i}$ in Figure 16B. For simplicity reasons, the inequation between state 1B and 1D is not shown. However, this inequation is not required to find the thermodynamically most stable state since at least either 1A or 1C are more stable than 1D and therefore the Cassie-Baxter state can here be excluded from all further considerations. It is necessary to point out, that in contrast to chapter 2.1.3 where the Cassie-Baxter state was found to be thermodynamically stable under certain conditions, the exposition for the considerations done here are different. In chapter 2.1.3 a drop with constant volume was forced on a surface and its behaviour predicted, excluding a state equivalent to 1C, while here the long-term stability is of interest and therefore a volume change due to flowing off of impregnation liquid is allowed.

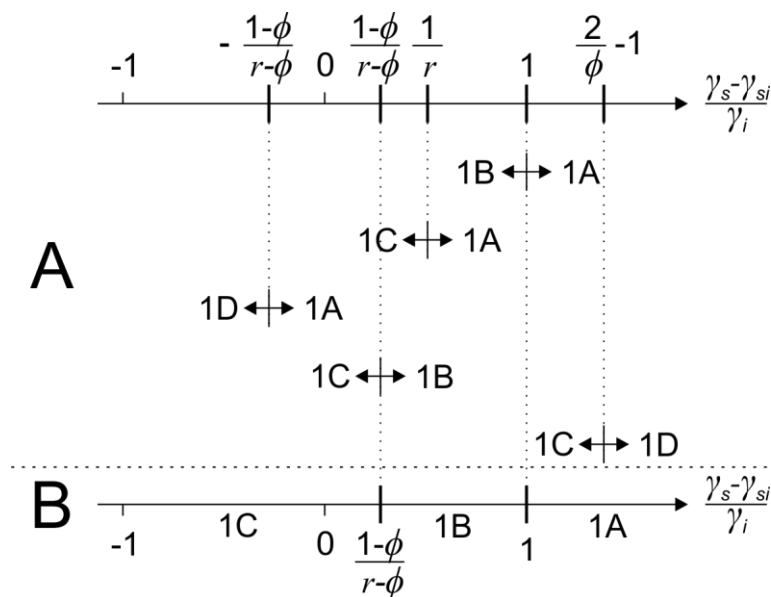


Figure 16: A: Results of the inequations between the energies of the different wetting states in region 1; B: Most stable state in region 1.

From these inequations, the way the impregnation liquid behaves on the rough substrate can be

fully predicted by determining $\frac{\gamma_s - \gamma_{si}}{\gamma_i}$, r and ϕ . $\frac{\gamma_s - \gamma_{si}}{\gamma_i}$ is directly accessible by measuring the contact

angle of the impregnation liquid on the flat substrate and applying the Young equation. r and ϕ

may be necessary for the full picture but they are only required to differentiate between state 1B

and 1C. However, the only state capable to function as a SLIPS system is state 1A. In the other states,

the solid surface would be at least partially exposed to the probe liquid when it comes in contact

with the surface. It can be concluded that the contact angle of the impregnation liquid on a flat

substrate has to be 0° ($\frac{\gamma_s - \gamma_{si}}{\gamma_i} \geq 1$) in order for the liquid to behave according to state 1A when

using the same combination of liquid and solid on a rough substrate (see Equation 1).

Similar considerations can be made for the states of region 2 by simply replacing γ_i with γ_{il} and γ_s

with γ_{sl} (Figure 17 and Figure 18). Because of the results in region 1 an equivalent of state 1D is no

longer necessary.

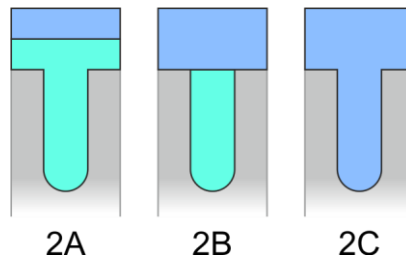


Figure 17: Different possible wetting states in region 2.

$$E_{2A} = r\gamma_{si} + \gamma_{il} \quad (41)$$

$$E_{2B} = (r - \phi)\gamma_{si} + (1 - \phi)\gamma_{il} + \phi\gamma_{sl} \quad (42)$$

$$E_{2C} = r\gamma_{sl} \quad (43)$$

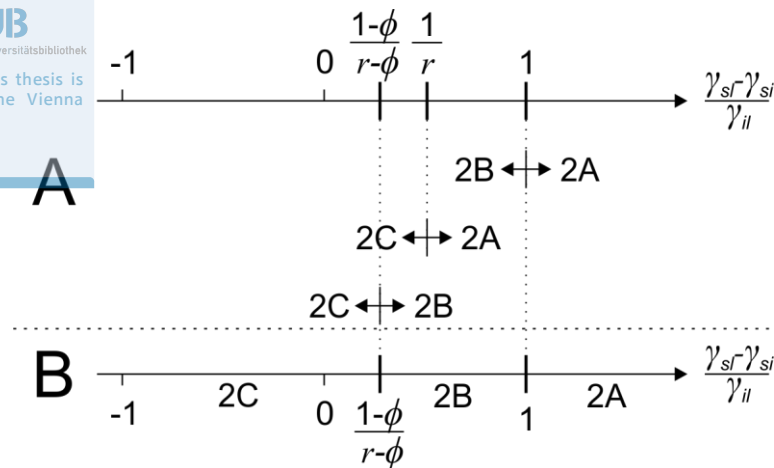


Figure 18: A: Results of the inequations between the energies of the different wetting states in region 2; B: Most stable state for region 2.

In region 2, again, the only term necessary to distinguish between the desired 2A state, with all solid features submersed in impregnation liquid, and the rest is $\frac{\gamma_{sl} - \gamma_{si}}{\gamma_{il}}$. This one can also be directly acquired by using the Young equation and measuring the contact angle of the impregnation liquid on the flat solid substrate but this time with probe liquid as surrounding. Also in this case, a contact angle of 0° is needed ($\frac{\gamma_{sl} - \gamma_{si}}{\gamma_{il}} \geq 1$).

For both region 1 and 2 the behaviour so far was described using only the static contact angle. However, this is not sufficient to reliably predict the SLIPS system, since the static contact angle merely defines the state with the lowest energy. Much more revealing is the advancing and the receding contact angle, since they describe the thresholds where spontaneously changes happen. An advancing contact angle of 0° of the impregnation liquid on the substrate with either air or probe liquid as surrounding means thereby that, no matter the current state the liquids are in, it will immediately switch to state 1A or 2A, respectively. Once state 1A or 2A is formed, a receding contact angle of 0° is required to prevent the liquids to spontaneously switch to any other state. Receding contact angles are generally lower than advancing ones. Thus, it is easier to establish conditions maintaining the SLIPS system than creating it. This means, it is necessary under all used surroundings to have a receding contact angle of the impregnation liquid on the substrate of 0° to maintain the SLIPS and it is necessary to have at least one surrounding which also gives an advancing contact angle of 0° to form the SLIPS state.

Finally, this leaves region 3 to discuss. Here only the behaviour of the two liquids is of interest. The first issue is complete wetting of the probe liquid on the impregnation liquid (Figure 19). This is problematic since the probe liquid will not flow entirely of the surface when tilted but a thin film

will remain. The condition to avoid this problem can be simply derived from the Young equation

with non-complete wetting occurring if $\frac{\gamma_i - \gamma_{il}}{\gamma_l} < 1$.

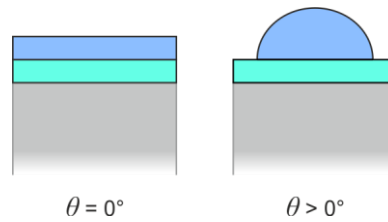


Figure 19: Transition between complete ($\theta = 0^\circ$) and non-complete ($\theta > 0^\circ$) wetting on SLIPS.

The final issue regarding thermodynamic stability is so-called cloaking (Figure 20). Here the impregnation liquid is sucked out of the pores and forms a thin layer around the probe liquid. To determine the transition, the energies of the two states have been calculated and compared. Since ultimately only the inequation between $E_{non-cloaking}$ and $E_{cloaking}$ is of interest, terms identical for both energies can be neglected.

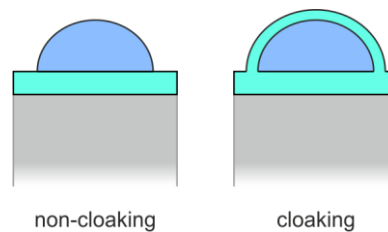


Figure 20: Transition between cloaking and non-cloaking behaviour on SLIPS.

$$E_{non-cloaking} = \gamma_l \quad (44)$$

$$E_{cloaking} = \gamma_{il} + \gamma_i \quad (45)$$

This results then in cloaking not occurring if $\frac{\gamma_l - \gamma_{il}}{\gamma_i} < 1$.

2.1.6 Metal-assisted Etching of Silicon Nanowires

Metal-assisted etching [47] (Figure 21) is a versatile method to produce a wide range of differently nanostructured silicon depending on the particular conditions. The general principal is to bring noble metal particles in contact with a silicon surface. The arrangement is then submerged in a solution containing an oxidizing agent, most commonly hydrogen peroxide (H_2O_2), and hydrofluoric acid (HF). Due to its higher electrochemical potential, the metal then acts as a cathode while the silicon functions as an anode. This accelerates the reduction of the oxidizing agent at the metal particles and allows a subsequent charge transfer from the thereby produced electron holes to the silicon. The oxidized silicon is then dissolved by the also present HF. Finally, the formed ions diffuse away from the interface while the metal moves further into the bulk forming a pore.

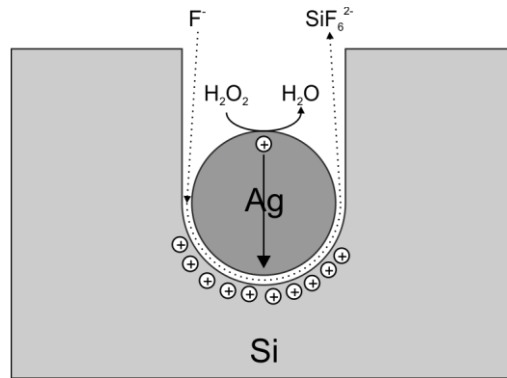
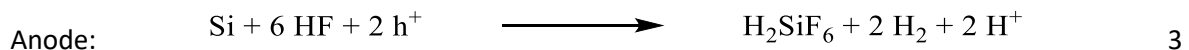
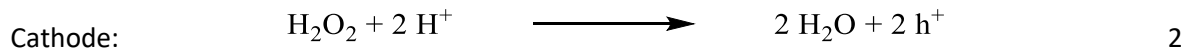


Figure 21: Metal-assisted etching schema.

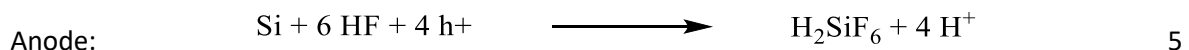
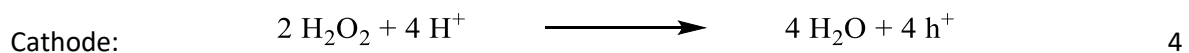
The overall reaction (Reaction 1) is a mixed reaction of an electroless and a chemical reaction.



Which of these two is dominant can be controlled with the HF:H₂O₂ ratio. For very low H₂O₂ concentrations compared to HF, the chemical mechanism is dominant (Reaction 2 and 3). In the previous reaction scheme n is then 2. Here silicon is partly oxidized by H₂O₂ but also by H⁺.



If very high H₂O₂ concentrations are used, the electroless mechanism is prevailing. Then n is 4. In this case, just H₂O₂ is responsible for the oxidation, so the most prominent visible difference is that no hydrogen gas is formed during the reaction. (Reaction 4 and 5)



The transition from electroless to chemical etching is fluent, allowing also intermediate values for n. For both cases, the formation of the electron holes (Reaction 2 and 4) and the dissolution of oxidized silicon (Reaction 3 and 5) are largely independent reactions with independent reaction rate. It is therefore expectable that this is also the case for the combined overall reaction. If the H₂O₂ concentration is low in comparison to HF, the anode reaction is faster and electron holes are immediately consumed as soon as they are transferred to the silicon. This leads to sharply defined cylindric pores. With high H₂O₂ concentration, this is not the case. Then the formed electron holes have time to diffuse in the silicon before they are consumed. This widens the pores close to the

surface and gives cone shaped pores. The cone shape is more pronounced with increasing H_2O_2 concentration and can ultimately lead to a completely isotropic etching process.

There is a multitude of different ways to initially deposit the noble metal on the silicon surface which cannot all be covered. Which method is suitable for a specific task only depends on the requirements regarding control over shape, size and distribution affecting the final pores. In regard of this work, the only method briefly discussed will be the wet-chemical deposition of silver from an $AgNO_3/HF$ solution. This is again a metal-assisted etching process with Ag^+ as the oxidizing agent. The main difference to the already discussed procedure with H_2O_2 is that at the beginning no catalyst is present at the surface and first a slow, uncatalyzed nucleation step has to take place. However, as soon as some silver is deposited at the surface, the reduction of other silver ions happens preferentially at the metal particles. This leads to growth of the nuclei into larger dendrite structures and again to charge transfer to the silicon and its subsequent dissolution.

The formed pores in metal assisted etching of Si (100) surfaces are typically parallel to each other, which can be explained with the so-called back-bond theory. A surface atom on a (100) plane has two back-bonds to neighbouring silicon atoms while a surface atom on a (111) or (110) plane has three back-bonds. It is therefore easier to remove atoms on the (100) plane leading to an enhanced etching speed orthogonal to this plane. This theory was supported by studies [62] using an addition of oxidant effectively changing the surface $-H$ groups to $-OH$. These groups weaken the back-bonds and reduce the anisotropy of the etching. However, it was also reported that with even higher oxidant concentration the preferred direction can switch to [111] which cannot be explained with the back-bond theory [63].

If the metal particles are close enough together, single pores are connected and nanowire-like structures remain in between. The metal particles do not necessarily have to touch each other for this to occur since there are three different mechanisms which widen the pores. First of all, judging from the electrochemical potential, silicon is also etched without a catalyst in H_2O_2/HF solution but at a much slower rate. Secondly, a partial dissolution of the metal particles and precipitation on the sidewalls of the pores may occur, which then catalyses etching there. Finally, the transferred electron holes can diffuse to the sidewalls leading to oxidation and dissolution there.

It was also reported that illumination during the etching has an influence on the etching speed [47]. This is, however, only true if the light intensity is high enough so that the concentration of photo-excited holes in the valence band is in a similar range as the concentration of holes due to the

oxidant. No difference between etching in darkness and regular ambient room light is to be expected, nevertheless as a precaution etching should be done in darkness.

2.2 Principles of Measurements

In this work, the analytical methods used were nuclear magnet resonance spectroscopy (NMR), scanning electron microscopy (SEM), Fourier transform infrared spectroscopy (FTIR), Brewster angle FTIR, Ellipsometry and Contact angle, surface tension and interface tension goniometry. Whereas the theoretical background of NMR, SEM and FTIR is widely known due to their versatility for all kind of research, the other mentioned methods are specialized to investigate mainly surface properties and are therefore less prevalent. This section should cover the theoretic background of these methods to highlight the information they provide.

2.2.1 Brewster Angle FTIR Transmission Spectroscopy

FTIR in general is a method able to identify functional groups in compounds via their vibrational spectra. Brewster angle FTIR uses a special setup which allows to measure FTIR spectra of slices of samples with parallel surfaces, here silicon wafers, in transmission without irritating interference fringes.

Silicon is in principle transparent to IR light, allowing coatings on silicon wafers to be measured in transmission. However, due to its higher refractive index than air, the IR beam will be partly reflected when entering and leaving the sample. This can be quite a problem, especially when the beam passes perpendicularly through two plane-parallel surfaces. The beam will then be partially reflected whenever it reaches an air-silicon interface multiple times back and forth. Since each reflection has the exact same path as the original beam, they will interfere with each other leading to a very pronounced interference pattern concealing relevant information.

To prevent this problem, the sample can be tilted in order for the beam to hit the sample under a different angle of incidence. Then the intensity of the reflected and transmitted beams changes. The light polarised orthogonally (s-polarised) and parallel (p-polarised) to the plane of incidence behave differently in this case (Figure 22). Their respective reflectivity can be calculated using the Fresnel equation (Equation 46 and 47).

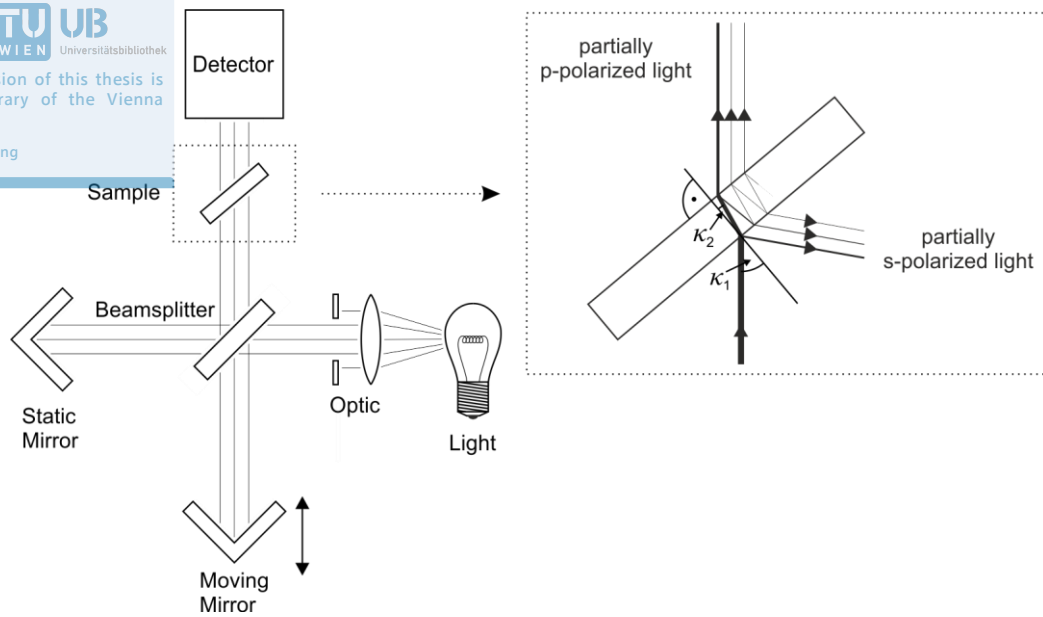


Figure 22: Schematic of a Brewster angle FTIR setup highlighting the partially polarization due to an angle of incidence (κ_1).

$$r_{s,12} = \left(\frac{N_1 \cos \kappa_1 - N_2 \cos \kappa_2}{N_1 \cos \kappa_1 + N_2 \cos \kappa_2} \right)^2 \quad (46)$$

$$r_{p,12} = \left(\frac{N_2 \cos \kappa_1 - N_1 \cos \kappa_2}{N_2 \cos \kappa_1 + N_1 \cos \kappa_2} \right)^2 \quad (47)$$

N is the complex refractive index which can be calculated from the refractive index (n) and the absorption coefficient (k) ($N = n - ik$). κ_1 and κ_2 , the angles of incidence and refraction (Figure 22), are defined by the Snell's law (Equation 48).

$$N_1 \sin \kappa_1 = N_2 \sin \kappa_2 \quad (48)$$

Based on these equations, $r_{s,12}$ and $r_{p,12}$ can be plotted as a function of the angle of incidence (κ_1) for any two phases with known refractive indices. The plot for air ($n_1 = 1.0003$, $k_1 = 0$) and silicon ($n_2 = 3.49713$, $k_2 = 0$) is shown in Figure 23.

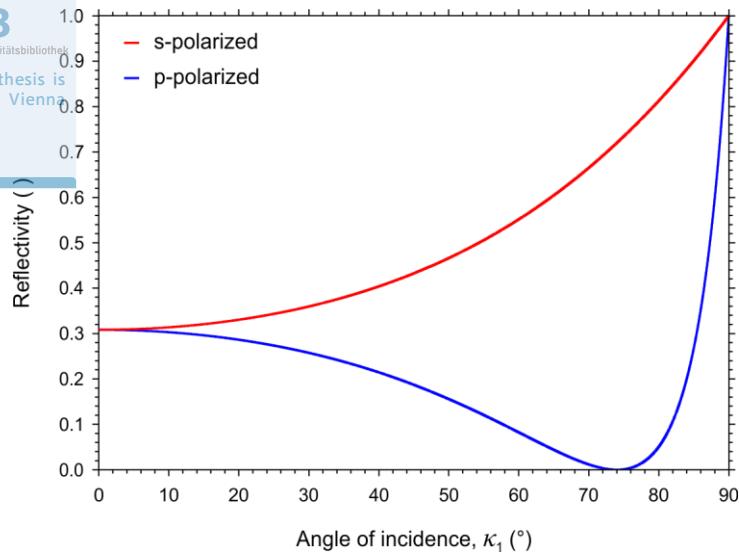


Figure 23: Reflectivity of s- and p-polarized light as a function of the angle of incidence for silicon and air.

For a certain angle, the so-called Brewster angle, the reflectivity of p-polarized light is 0. The amount of interference increases with increasing reflectivity. If the sample is tilted to a degree that the incoming lights hits it under the Brewster angle, p-polarized light will not show any interferences at all. Simultaneously, the total intensity of s-polarized light passing through the sample, which is still susceptible to interferences at this angle, is greatly reduced due to the high reflectivity when first entering the silicon. If this suppresses interferences not sufficiently, s-polarized light can additionally be removed with the use of a polarizer.

2.2.2 Ellipsometry

Ellipsometry is an optical method which allows the determination of either refractive indices, absorption coefficient or layer thickness of thin films if the respective other properties are known. (Figure 24)

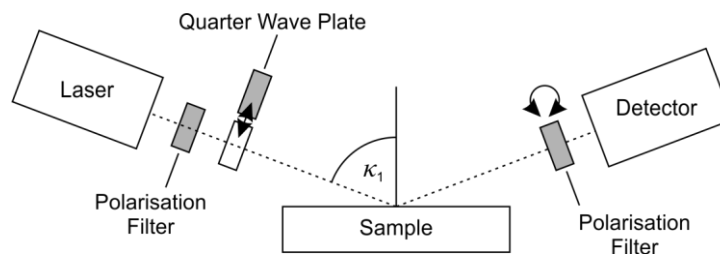


Figure 24: Schematic arrangement for ellipsometric measurements.

As light source for ellipsometric measurements, monochromatic and polarised light is required. Commonly, a laser with added polarisation filter is therefore employed. For the measurement, the beam is then targeted on a substrate covered with a thin film under a certain angle of incidence. The polarisation filter is thereby set to produce linear polarised light at an angle of 45° relative to

the plane of incidence on the sample. Since the planes to describe polarisation of light can freely be chosen, it is more convenient to describe this beam as an overlay of two different beams, one orthogonally polarised (s-polarised) and one parallel polarised (p-polarised) to the plane of incidence on the sample. Under these conditions, the two beams have the same amplitude and no phase shift. The events at the surface can be more easily depicted if the two beams are described completely independent from each other. As soon as one of the two beams hits the interface between the thin layer and air, it will be partly reflected and partly refracted due to different refractive indices of the two phases as discussed in 2.2.1. The refracted beam will then hit the next interface consisting of the thin layer and the substrate being again partly reflected and refracted for the same reason. As a consequence, multiple reflections will occur within the thin layer losing some of the light on either side of the layer. The final beam reflected by the whole sample is therefore an overlay of all the beams produced by the different reflection events. Since light in general can be described as a sinus wave and the sum of different sinus waves with the same frequency give a single new sinus wave with the same frequency but altered amplitude and phase, it is plausible that also the amplitude and phase of the reflected beams changes. The change depends thereby on the reflectivity at the interfaces and the layer thickness. As already discussed in 2.2.1 and shown in Figure 23 the reflectivity of the s- and the p-polarised beam is not the same, leading to different amplitude and phase shifts. At the detector, an overlay of these beams will arrive which is then in general elliptically polarised. The detector will then be used to determine the ratio of amplitudes ($\tan \varphi$) and phase shift (Δ) of the two beams. This can be done by measuring the total amplitude of the light as a function of the orientation of a second polarisation filter once without any further adjustments and once with an additional quarter wave plate in the initial beam path. This plate leaves the initial ratio of the amplitudes untouched but adds a phase shift of $\frac{\lambda}{4}$ between the two beams. The two measurements of the reflected beam allow then the calculation of the ratio of amplitudes and phase shifts.

In order to use these parameters to determine the thickness of the thin layer, the following equations can be used. R_s and R_p in this case stand for the total reflectivity of the whole arrangement for either s- or p-polarised light, respectively.

$$\frac{R_p}{R_s} = \tan \varphi e^{i\Delta} \quad (49)$$

The reflectivity of the whole sample can then be calculated from the reflectivity at the interfaces between air (phase 1), thin layer (phase 2) and the substrate (phase 3).

$$R_x = \frac{r_{x,12} + r_{x,23} e^{-2\beta i}}{1 + r_{x,12} r_{x,23} e^{-2\beta i}} \quad (50)$$

$$\beta = 2\pi \frac{d}{\lambda} \sqrt{N_2^2 - N_1^2 \sin^2 \kappa_1} \quad (51)$$

In these equations d is the layer thickness and λ is the wavelength of the laser. The reflectivity at the single interfaces can be calculated with the Fresnel equation, which was already shown in 2.2.1 (Equation 46 and 47). By combining all these equations, it is possible to calculate one parameter, most often the layer thickness, if all the other parameters, namely refractive indices, absorption coefficients, angle of incidence and wavelength of the laser, are known. In an analogous way, also a second thin layer can be included in the calculation, which is often necessary for substrates which are susceptible to form native oxide layers. However, then the second layer has to be fully characterised, including the layer thickness, to get meaningful results.

2.2.3 Contact Angle, Surface Tension and Interface Tension Goniometry

Optical goniometry is a method which allows the determination of the surface tension of a liquid and the interface tension between two liquids by analysing a pendant drop. For these measurements, the density of the involved phases has to be known. It can also be used to measure the contact angle of a sessile drop on a solid substrate. (Figure 25)

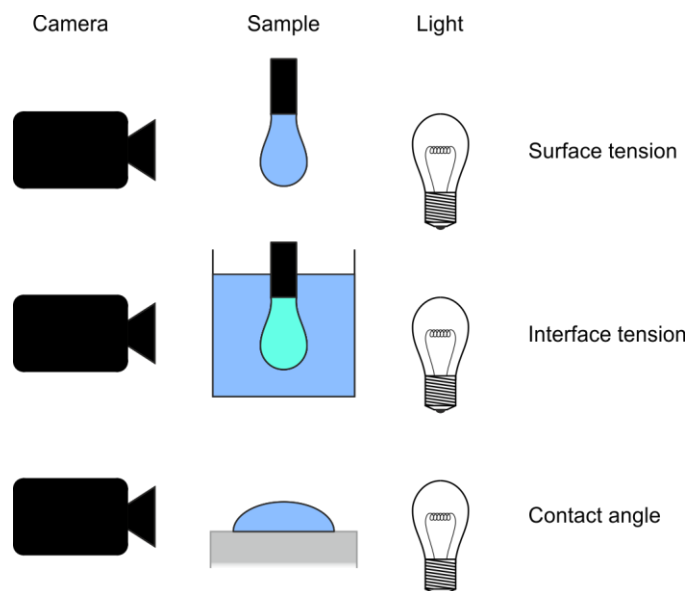


Figure 25: Schematic arrangement for goniometric measurements.

The general arrangement for either of those measurements is simply a camera facing horizontally at a pendant or sessile drop with a light source in the background. The liquid and an eventually involved substrate will then appear dark while the surrounding is bright. By analysis of the grey scales of the picture, the contour of the drop and, in case of a sessile drop, additionally the baseline

of the drop, can be determined (Figure 26). The desired property can then be evaluated from these curves.

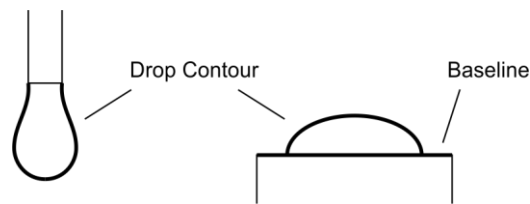


Figure 26: Representation of drop contour and baseline in goniometric measurements.

In order to measure the surface tension of a liquid, a drop is placed at the tip of a cannula. There are two forces in equilibrium which define the final drop shape. First of all, the surface tension describes the behaviour of the drop to minimize its surface. This force then also results in a slight pressure increase inside the drop to obtain an even smaller surface. According to the Laplace equation, the pressure increase is dependent on the surface tension and the curvature of the drop. In other words, the curvature of the drop correlates with the pressure difference and the surface tension. The second force is gravity. Gravity in a resting fluid always results in a hydrostatic pressure. The hydrostatic pressure at a certain point in the drop is dependent on the height and density of liquid above this point. This additional influence on the pressure will also affect the curvature of the drop. For a drop with known density and dimensions, the influence of the hydrostatic pressure can be calculated and, since the total pressure difference can be derived from the curvature, the surface tension can be determined. This approach is called Young-Laplace method and is based on the following equation [64].

$$\frac{a}{r_1} + \frac{a \sin \varphi}{x} = -\frac{a g \Delta \rho z}{\gamma} + 2 \quad (52)$$

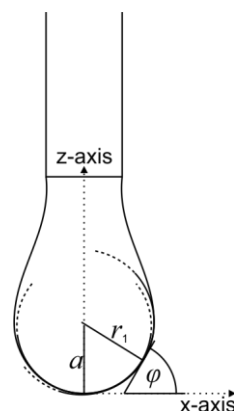


Figure 27: Representation of the different parameters used for the Young-Laplace method.

In this equation, a is the radius of the curvature at the apex of the drop, r_1 is the radius of the curvature at a specific point and φ describes the slope at that point, g is the gravitational constant,

$\Delta\rho$ is the density difference between drop and surrounding, γ is the surface or interface tension and the coordinates x and z describe the contour. Drop shape analysis uses this equation and fits the surface tension to match the measured shape. The very same procedure can also be applied with another liquid as surrounding medium instead of air, resulting then in the interface tension.

The determination of the contact angle works in a similar way. Here again the base line and the drop contour will first be determined from the grey scales of the captured picture. The baseline will then be fitted with a straight line while the drop contour will be fitted with a more complex function. Then the first derivative of the fitted contour will be determined and the angle between it and the base line gives the contact angle.

There are two fundamentally different approaches to determine the fitted drop contour. The first is to use a model which is based on a physical context, which then has to consider separately all influences from gravity, density and other parameters. This can again be done with the Young-Laplace method. It gives therefore well-grounded results and, since the drop is modelled as a whole, small disturbances of the contour are often negligible. However, it is not capable to describe behaviour which was not considered in the model beforehand. Most noteworthy, it is unable to properly fit asymmetric drops which prohibits the measurement of advancing and receding drops on tilted sample stages. Another method to obtain advancing and receding contact angles is to immerse a needle into the drop and alternately increase and decrease the drop volume until the contact line between surface and drop starts to move. However, since the Young-Laplace method fits the drop as a whole an immersed needle, even if only at the apex of the drop, renders the measurement useless. The Young-Laplace method also has its limitations when it comes to flat drops with very small contact angles. In this case errors become large because the determined radius of the curvature is then strongly susceptible to small deviations in the captured picture.

The second approach is to neglect any physical context and use whatever shape models the measured contour best. This can be done with circles, ellipses, polynomials or other functions. A common routine is to just model the contour close to the contact points with a polynomial and neglect the apex. This approach has then basically the opposite characteristic than the Young-Laplace method and they therefore perfectly complement each other. It allows the use of an immersed needle, asymmetric drops and the determination of small contact angles. On the other hand, is it sensitive to non-ideal behaviour of the drop close to the contact point due to inhomogeneities on the surface. It can therefore always be used when the, in principal more robust, Young-Laplace method is not suitable.

3 Experimental

The approved original version of this thesis is
available at the main library of the Vienna
University of Technology.

<http://www.ub.tuwien.ac.at/eng>

3.1 Chemicals and Material

The following chemical were purchased from Sigma-Aldrich and were used without further purification: Acetone, $\geq 99.5\%$, Toluene, $\geq 99.3\%$, 1H,1H,2H,2H-Perfluoro-1-decanol, 97 %, Propiolic acid, 95 %, Hydrofluoric acid, 48 wt.%, Sodium azide, $\geq 99.5\%$, Silver nitrate, $\geq 99\%$, 1-Methylimidazole, 99 %, (3-Chloropropyl)trimethoxysilane, $\geq 97\%$, Trichloro(octadecyl)silane, $\geq 90\%$, Tetrahydrofuran, $\geq 99\%$, Cyclohexane, $\geq 99\%$, (+)-Sodium L-ascorbate, $\geq 98\%$, Ethylene glycol, 99.8 %, Copper(II) sulphate, $\geq 99\%$

The following chemical were purchased from Merck and were used without further purification: Ethanol absolute, $\geq 99.5\%$, Nitric acid, 65 wt.%, Toluene-4-sulfonic acid monohydrate, $\geq 99\%$

The following chemical were purchased from Acros and were used without further purification: N-hexadecane, 99 %, Dimethyl sulfoxide, 99.7 %, N,N-Dimethylformamide, 99.8 %

The following chemical were purchased from Fluka and were used without further purification: Ethyl acetate, $\geq 99.5\%$, Sulfuric acid, 95-97 %

Hydrogen peroxide, 36 wt.%, was purchased from Carl Roth and used without further purification.

Acetonitrile, $\geq 99.95\%$, was purchased from VWR and was used without further purification.

Silicon wafers, 1-0-0, p-type, boron-doped, 10-20 Ωcm , 500-550 μm thickness, double-sided polished, were purchased from MEMC and cleaned as described in 3.2.1.

11-bromoundecyltrichlorosilane, 95 %, was purchased from Gelest and was used without further purification.

Deionized water was produced in-house and used without further purification.

All used ionic liquids were kindly provided by Katharina Schröder.

3.1.1 Synthesis of THFDP

For the synthesis of THFDP (3,3,4,4,5,5,6,6,7,7,8,8,9,9,10,10,10-heptafluorodecyl propiolate), 1H,1H,2H,2H-Perfluoro-1-decanol (2.3 g, 5 mmol), Propiolic acid (0.92 ml, 15 mmol) and Toluene-4-sulfonic acid monohydrate (238 mg, 1.25 mmol) were refluxed in 50 ml Toluene for 24 hours. The solution was then washed three times with 50 ml water. Afterwards the solvent was removed under

reduced pressure. The obtained solid was purified by sublimation ($2.3 \cdot 10^{-1}$ mbar, 100 °C). 1.69 g (65 % yield) of white crystals could be isolated. The product was characterized with FTIR, molten between two sodium chloride windows, and with $^1\text{H-NMR}$ in CDCl_3 . See 4.1.2.3 for the characterization of the compound.

3.1.2 Synthesis of $[\text{C}_3\text{mim}]\text{Cl}$

For the synthesis of $[\text{C}_3\text{mim}]\text{Cl}$ (3-methyl-1-(3-(trimethoxysilyl)propyl)-1H-imidazol-3-ium chloride) we followed a procedure from literature [65]. (3-Chloropropyl) trimethoxysilane (68.6 ml, 376 mmol) and 1-Methylimidazole (15.0 ml, 188 mmol) were stirred for 60 h at 90 °C under N_2 atmosphere. Afterwards the mixture was cooled to room temperature and extracted twice with 150 ml diethyl ether. Residual diethyl ether was removed under reduced pressure. The yellowish, viscous liquid was characterized with IR between sodium chloride windows and with $^1\text{H-NMR}$ in CDCl_3 . The characterization of the compound can be found in 4.2.3.1.

3.2 Sample Preparation

3.2.1 Cutting and Cleaning of Silicon Substrates

Silicon wafers were cleaved along crystallographic axes using a diamond tip to form rectangular pieces in the size of 25 x 18 mm. These pieces were then cleaned by sonication (Bandelin Sonorex Super 10 P) in toluene for 10 minutes, swiped with a toluene drenched tissue, rinsed with about 1 ml toluene and finally the remaining liquid was blown off with argon. Afterwards the samples were treated in an UV/Ozon chamber (Boekel UV clean Model 135500) twice for 10 minutes each turning upside down in between. Flat samples were then immediately used after this cleaning procedure.

3.2.2 Etching of Silicon Nanowires

Freshly cleaned and cut silicon wafers were treated for precisely 1 minute in 20 ml of an aqueous solution containing hydrogen fluoride (6.2 mol/l, 4.5 ml 48 %) and silver nitrate (5 mmol/l, 17.0 mg, unless stated otherwise, see 4.1.1.3). The samples were then thoroughly rinsed with water and immediately afterwards, without intermediate drying, etched in 20 ml of an aqueous solution containing hydrogen fluoride (6.2 mol/l, 4.5 ml 48 %) and hydrogen peroxide (0.06 mol/l, 100 μl 36 wt.%, unless stated otherwise, see 4.1.1.1) for precisely 10 minutes (unless stated otherwise, see 4.1.1.2). The beaker used for etching was covered with a second, larger beaker and aluminium foil for etching in darkness. Afterwards the samples were again thoroughly rinsed with water and treated for 5 minutes in a 1:1 mixture of nitric acid (65 wt.%) and water. After another rinsing step

with water, the samples were immersed for 30 minutes in piranha solution (4:1; H₂SO₄ 96 % : H₂O₂ wt. 36%). The samples were then immersed for about 5 minutes first in water and then in acetone, respectively. The samples were then blow-dried with argon.

3.2.3 Surface Modification

Three freshly cleaned or etched samples were immersed in a single beaker containing 10 ml toluene and either trichloro(octadecyl)silane (OTS, 0.01 mmol, 3.94 μ l) or (11-bromoundecyl) trichlorosilane (BUTS, 0.01 mmol, 2.94 μ l) or 3-methyl-1-(3-(trimethoxysilyl) propyl)-1H-imidazol-3-ium chloride ([C₃mim]Cl, 0.1 mmol, 28,1 mg). Samples being coated with OTS or BUTS were removed after 4 hours (unless stated otherwise, see 4.1.2.1), while the [C₃mim]Cl treatment was performed for 48 hours. Afterwards the samples were removed from the solution, rinsed with toluene and remaining liquid was blown off with argon.

For the Huisgen 1,3-dipolar cycloaddition [66], three BUTS coated samples were simultaneously treated overnight in 10 ml N,N-Dimethylformamide (DMF) saturated with sodium azide. Afterwards they were immersed in 10 ml DMF with THFDP (0.1 mmol, 51.6 mg), (+)-sodium L-ascorbate (0.128 mmol, 25.5 mg), copper sulphate (0.005 mmol, 0.82 mg) and water (200 μ l) for 3 days. They were then rinsed thoroughly consecutively with DMF, water and acetone and blow dried.

3.2.4 Impregnation of SLIPS

Drops of ionic liquid were placed generously on native or functionalized nanowire-covered samples to ensure complete coverage of the samples with ionic liquid. The samples were then placed vertically in a beaker containing enough ionic liquid to cover only the bottom of the beaker and sufficient probe liquid to cover the remaining sample to saturate the ionic liquid with probe liquid. The samples were stored this way for 7 days to allow the excessive ionic liquid to flow off. Upon removing the samples from the beaker, remaining ionic liquid on the lower edge submerged in ionic liquid was carefully removed with a tissue.

3.3 Sample Characterization

3.3.1 FTIR

FTIR measurements were done with a Bruker Vertex 80 FTIR (Figure 28) using the provided OPUS 7.5 software. The measurements were done at a resolution of 4 cm⁻¹. A narrow band MCT detector was thereby used. For each measurement 256 scans were recorded.



Figure 28: Bruker Vertex 80 FTIR with open sample chamber and sample holder for Brewster angle measurements.

All silicon samples were measured in transmission with an angle of incidence of 40° which was sufficient to suppress interference fringes (see 2.2.1). For the determination of coatings on flat samples, the coated samples were referenced against a different uncoated wafer. For investigation of coatings on nanowire samples, each uncoated sample was first individually measured immediately after etching, which acted then as a reference for subsequent measurements of the same sample. To minimize peaks attributable to water vapour and carbon dioxide, the chamber was purged with dry air for 2 minutes before each measurement. Residual carbon dioxide peaks were then removed with the integrated tool of the software, while peaks attributable to water vapour were removed by subtracting a measured spectrum of water vapour from the actual measurement.

Spectra of liquid compounds were measured in transmission as liquid films between two sodium chloride windows.

3.3.2 Ellipsometry

Ellipsometric measurements were carried out using a Sentech SE 500adv (Figure 29) which uses a He-Ne laser as light source and a rotating analyser. The utilized wavelength was 632.8 nm. Data analysis was done with the supplied instrument software SE400advanced 2.16 which uses the McCracking algorithm. The used optical constants were: Si ($n = 3.865$, $k = 0.02$), SiO_2 ($n = 1.465$, $k = 0$), organic layer ($n = 1.5$, $k = 0$). The measurements were done at four different spots on each sample and were then averaged. The variation within a sample was always below 1 \AA .



Figure 29: Sentech SE 500adv ellipsometer and power supply.

3.3.3 Optical Goniometry

Contact angles, surface tensions and interface tensions were measured using a Krüss DSA 30 goniometer (Figure 30) in combination with the provided Krüss ADVANCE 1.5.1.0 software. The device was equipped with a camera with a resolution of 780 x 582 and could record 60 frames per second. Further, a software-controlled inclinable sample stage was installed. The sample stage was improved with a custom-built housing (see 4.1.3.1) which allowed better saturation of the atmosphere around the sample with probe liquid to reduce undesirable evaporation of the drop.

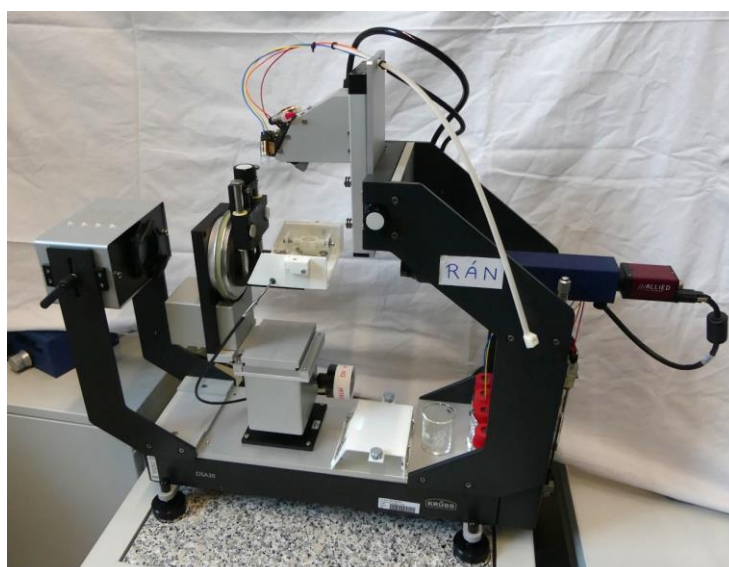


Figure 30: Krüss DSA 30 goniometer.

Static contact angles were determined by placing a drop on the investigated surface with a needle. The volume was adjusted to give drops which cover about 0.5 cm² of the surface. Data analysis was then done with the tangent method ($\theta < 10^\circ$) or the Young-Laplace method ($\theta > 10^\circ$) of the instrument software (see 2.2.3). For the determination of the advancing and receding contact

angles the sample stage was tilted at a rate of 10°/min for final SLIPS systems (4.2.7), at a rate of 15°/min for suitability tests for SLIPS systems (4.2.5) and at a rate of 30°/min for measurements of Cassie-Baxter systems (4.1.3) and the determination of the surface tension of ionic liquids (4.2.2.1).

During the measurement pictures were continuously recorded until the drop rolled off the surface. The last frame which showed the still stationary drop was then used to determine the advancing and receding contact angle using the tangent method. Contact angles with another liquid as surrounding were recorded with the help of a rather large cuvette (4 x 4 x 3.2 cm) which was about half filled. To avoid spillage of the liquid in the cuvette, the sample stage was only tilted up to 45° for measurement of advancing and receding contact angles. For each arrangement three different samples were etched, if applicable, coated and measured. The measured angles were then averaged.

For surface and interface tension measurements, first, the determination of the density was necessary. Ionic liquids were measured in a 10 cm³ pycnometer while for other liquids a 50 cm³ pycnometer was used. In either case, the empty and filled pycnometers were weighed at 20 °C on a Mettler AC 100 balance, respectively. The surface tension measurements were done using a pendant drop of the liquid in question hanging on a needle with an outer diameter of about 0.5 mm. The precise diameter of the needle was determined before equipping it with a micrometre calliper, which was then used to determine the scale of the captured picture. The drop volume was dosed to give drops as big as possible without falling off the needle. Data analysis of the captured picture was done with the Young-Laplace method. For the determination of interface tensions, the same general procedure was used but the surrounding air was replaced with a second immiscible or only partly miscible liquid by immersing the tip of the needle in a filled cuvette (4 x 4 x 3.2 cm). For each liquid or combination of liquids, the device was prepared once and then three drops were measured consecutively. The results were then averaged.

3.3.4 SEM

A FEI Quanta 200 MK2 electron microscope was used to record SEM images. It was equipped with an Everhardt-Thornley detector. The samples were mounted in the device in a way to obtain working distances between 8 to 11 mm. The electron beam voltage was set to 10 keV. For top-view pictures no additional modification was necessary but for cross sections the samples were freshly cleaved and the newly exposed area was measured.

3.3.5 NMR Spectroscopy

^1H NMR and ^{13}C NMR spectra were recorded on a Bruker AVANCE 250 spectrometer. The spectra were referenced internally to residual protio-solvent and solvent resonances, respectively, and were reported relative to tetramethylsilane ($\delta = 0$ ppm).

4 Results and Discussion

The approved original version of this thesis is
available at the main library of the Vienna
University of Technology.

<http://www.ub.tuwien.ac.at>

Based on the theory presented in 2.1, we decided to follow two different paths to achieve liquid repellent surfaces. The first and in general most commonly used are Cassie-Baxter systems. These systems promise to show high contact angles and function for virtually any liquid above a certain surface tension threshold.

Besides them, we decided to also investigate and prepare SLIPS systems. They are only useable in niche applications since they just work with specific probe liquids they were designed for. However, they show lower roll off angles than any other wetting state, which makes them very powerful tools for those systems.

4.1 Cassie-Baxter Systems

4.1.1 Topography

The theoretical background draws a quite clear picture regarding the demands to produce a functioning Cassie-Baxter system. Primarily, the surface topography has to be optimized. In Equation 17 can be seen that the only parameter of the surface structure which affects the contact angle in this state is the solid surface fraction (ϕ). Lower ϕ leads to higher contact angles.

Another point to consider is the stability range of the Cassie-Baxter state, which is presented in Figure 10. Judging from this figure, the thermodynamically stable region can be extended by increasing the roughness (r) since then the line representing the contact angle of the Wenzel state in this figure will become steeper. In addition, it can be seen in Equation 31 that increasing r also stabilizes the metastable extension of the Cassie-Baxter state. In order to enhance r , the two main parameters necessary to consider are the pore size as well as the length of the nanowires. However, it is advisable to choose lower pore size over nanowire length due to gravity. The influence of gravity on drops is usually neglected since it is relatively small. In the Cassie-Baxter state it forces the drops to not only sit on top of the columns but to be impaled on them ever so slightly. This happens to a certain degree so that the resulting force pushing the drop back on top of the columns, due to surface tension, interface tension and surface energy, equals it out with gravity. The force pushing upwards is proportional to the area of vertical side walls of the columns covered with liquid. A substrate with large and long pores has to incorporate therefore a lot more liquid into the pores than one with short and small pores to cover the same surface area. This hinders the roll off of the

drop since on its way over the substrate more mass transfer has to occur. Therefore, the substrate has to feature low ϕ , high r , as well as small pore size for efficient Cassie-Baxter systems.

We decided to use metal-assisted etching with silver as catalyst and H_2O_2 as oxidizing agent to achieve this. Silver is known to give mostly vertical pores, it is easy to precipitate on the surface and it is cheap [47].

4.1.1.1 Optimization of Hydrogen Peroxide Concentration

The first parameter which was varied to achieve the design goal was the H_2O_2 concentration of the etching solution. All other parameters in these experiments were kept unchanged as presented in 3.2.2. A total of five different H_2O_2 concentrations were chosen for this purpose, namely 0.03 M, 0.06 M, 0.12 M, 0.24 M and 0.36 M. A cross-section and a top-view of the respective samples recorded in SEM can be found in Figure 31.

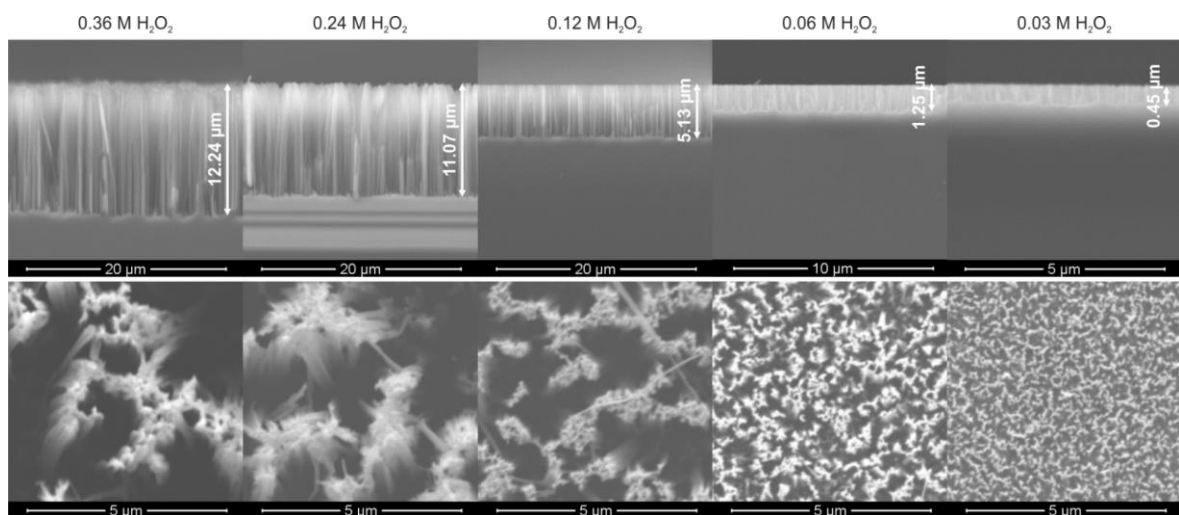


Figure 31: Pictures of cross-sections (top) and top-views (bottom) captured in SEM of nanowire samples etched with different H_2O_2 concentrations.

It is evident that the H_2O_2 concentration has a massive influence on the general structure of the nanowires. Unsurprisingly, the length of the nanowires increases with rising H_2O_2 concentration, however, for our purpose the more interesting changes here are the differences in pore size. It can be seen that samples produced with 0.03 M and 0.06 M H_2O_2 feature very small pores while the other samples have significantly bigger ones. One reason for this is that with increasing H_2O_2 concentration pores become more and more cone shaped due to diffusion of the injected electron holes as presented in 2.1.6. On the outer most surface, cone shaped pores are then indistinguishable from larger pores. Additionally, the flexibility of the nanowires plays an important role. More flexible nanowires tend to clump together. This will stabilize them in their upright position. The diameter of such bundles and the pores in between them is significantly larger than

for an array of only single, free standing nanowires. The flexibility increases mainly with the length of the nanowires but also with decreasing thickness due to cone shaped pores.

Judging from the pore size, only the lowest two concentrations are suitable candidates for liquid repellent surfaces. To distinguish further between those two, the ϕ values were determined by analysing the SEM pictures. The top view pictures were therefore converted in black and white, representing pores and solid at the interface, respectively. Since ϕ is defined as the fraction of solid at the interface, it could then be calculated from the average grey scale of the picture. A representation of the method for a sample etched with 0.06 M H₂O₂ is given in Figure 32. The calculation gave a ϕ of 0.25 for 0.03 M and 0.30 for 0.06 M samples. This determination of ϕ is strongly dependent on the threshold to distinguish between black and white areas in the pictures. However, it is not possible to set this threshold distinctively, it can only be estimated. A relatively large estimated error margin of about 0.1 has therefore to be considered as reasonable. Also, this analysis was only done for the lowest two concentrations since for the higher ones it becomes increasingly more difficult to distinguish between solid and pore.

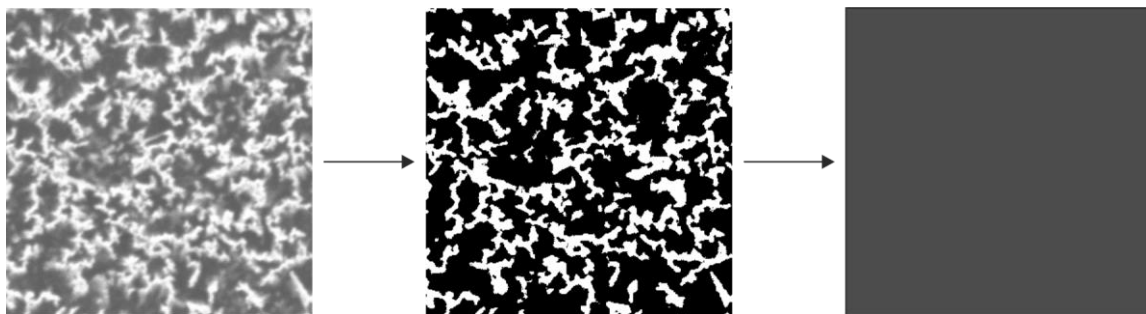


Figure 32: Representation of the procedure for determining ϕ from a top-view SEM image. Left: Section of the original SEM picture of a sample etched with 0.06 M H₂O₂; Middle: Same section after converting it to black and white; Right: Same section after averaging the grey scale.

Additionally, the r value was determined by FTIR measurements. The nanowire samples, as well as a flat sample were coated with OTS according to the procedure presented in 3.2.3. The integral of the peaks attributable to OTS has then to be proportional to r since OTS forms a complete monolayer on the surface as it will be shown in 4.1.2.1. When forming the ratio of the integral of a nanowire sample and the integral of a flat sample with a known r of 1, r of the nanowire sample can be obtained. Using this method and the integral of the CH region (2770-3000 cm⁻¹), the following values for the roughness were obtained (Table 3).

H ₂ O ₂ concentration (M)	<i>r</i> ()
0.03	4.9 ± 1.2
0.06	8.9 ± 0.6
0.12	21 ± 4
0.24	(-3.7)
0.36	94.7

Table 3: Calculated roughness from the ratio of CH bands measured in the FTIR between flat and nanowire sample etched with different H₂O₂ concentration and coated with OTS.

This method failed to determine *r* for samples etched with 0.24 M H₂O₂ concentration. The CH peaks under this condition were reproducibly negative and significantly smaller than expected (Figure 33). A satisfying explanation for this behaviour could not be found so far.

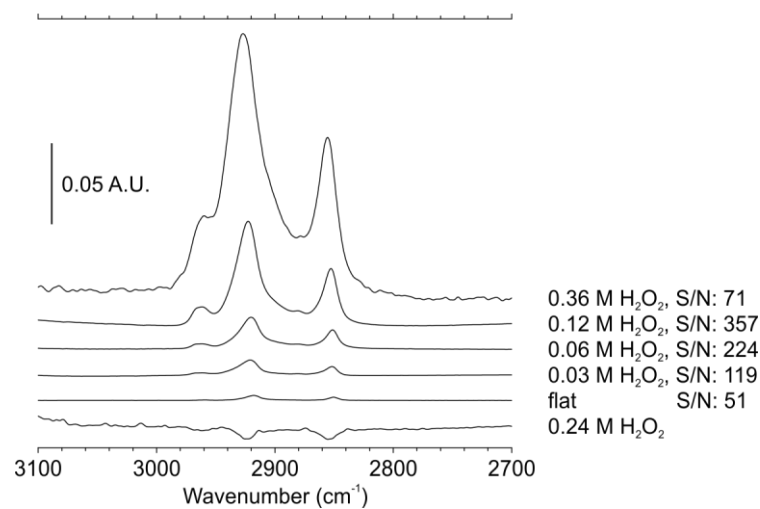


Figure 33: CH region of samples etched with different H₂O₂ concentration and coated with OTS and their calculated signal-to-noise ratio (S/N).

Besides considerations about the wettability, also the suitability of the samples for FTIR measurements is of interest since it is used in further steps to characterize coatings on the surface. It was observed that the total amount of IR light passing through the nanowire substrates strongly depends on the H₂O₂ concentration used for etching as it can be seen in Figure 34. The general trend here is that less IR light passes through the sample with increasing H₂O₂ concentration. The effect is especially pronounced for higher wavenumbers since here the wavelength of the light is already in the same range as the length of the nanowires.

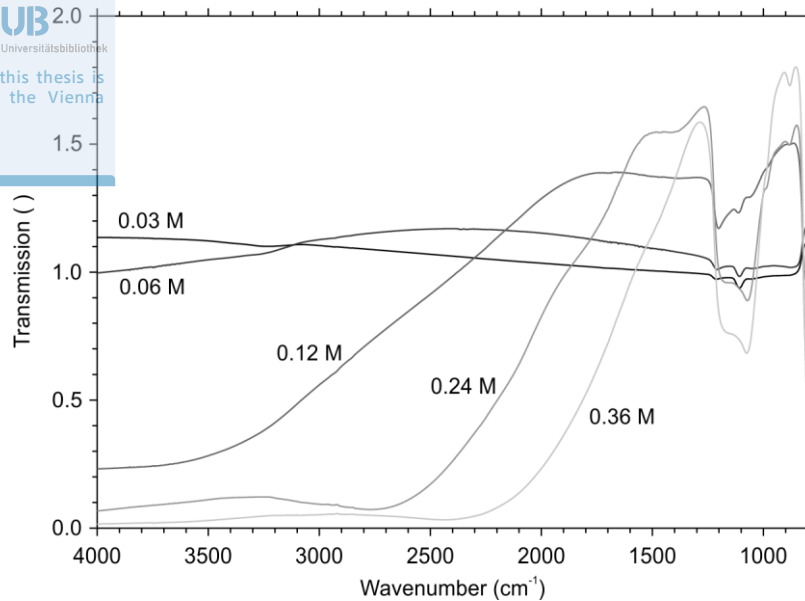


Figure 34: Transmission of infrared light of nanowire covered silicon samples etched with different H_2O_2 concentrations referenced to flat silicon.

This means there are two competing effects influencing the signal-to-noise ratio with increasing H_2O_2 concentration. First, the surface area increases, providing more space for binding the coating and leading to an enhanced signal. Secondly, the overall amount of light decreases, worsening the noise. This is especially true for high wavenumbers which contain lots of relevant information. We therefore calculated the signal-to-noise ratio for all samples etched with different H_2O_2 concentration and coated with OTS. We used here again a CH stretching peak ($\nu_{\text{as}}(\text{CH}_2)$ at 2927 cm^{-1}) since this is the peak occurring at the highest wavenumber of interest in this work. All bands at lower wavenumbers will show similar or better signal-to-noise ratios. The determined signal-to-noise ratios can be found in Figure 33.

Overall, we concluded that samples etched with 0.06 M H_2O_2 show the most promising results for further experiments since they show a good compromise between relatively small pores in combination with a low ϕ value and sufficiently high r and signal-to-noise ratio in the FTIR.

4.1.1.2 Optimization of Etching Duration

In the next step, the etching duration was varied to further improve the sample quality. In addition to the previous duration of 10 minutes, samples were also etched for 6, 8, 12 and 15 minutes. Pictures of the resulting nanowires captured in SEM can be found in Figure 35.

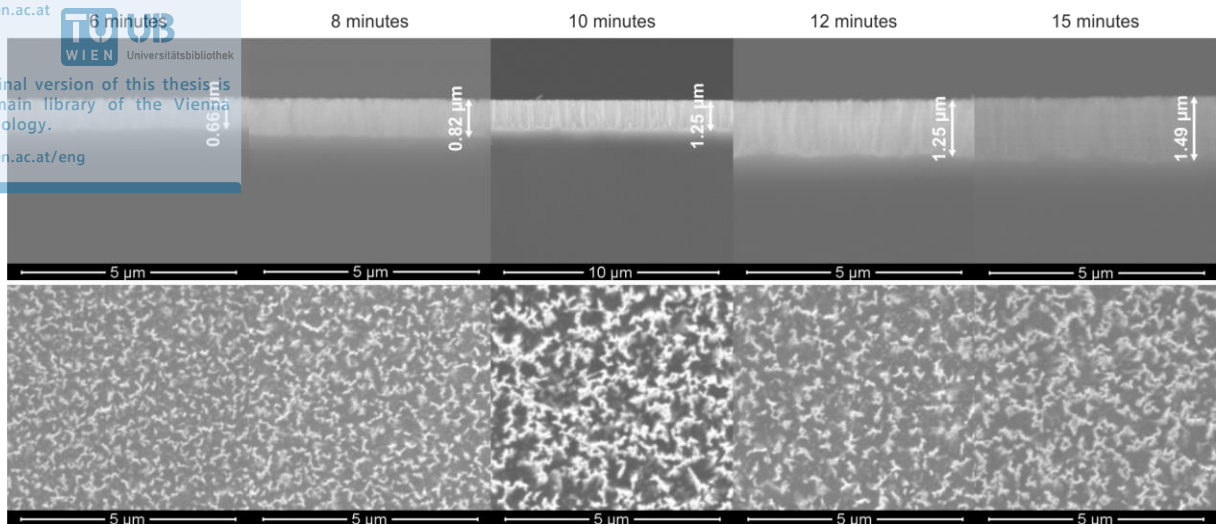


Figure 35: Pictures of cross-sections (top) and top-views (bottom) captured in SEM of nanowire samples etched for different durations. Pictures for 10 minutes etching duration taken from series conducted in 4.1.1.1.

The most noteworthy change is the increase in length of the nanowires with rising etching duration, accompanied by a slightly higher tendency to form bundles due to higher flexibility. The samples were also characterized in a similar manner as in the previous chapter (Table 4, Figure 36). The roughness and signal-to-noise ratio this time, however, was calculated based on a coating with BUTS since further modification and contact angle measurements were planned for these samples but not pursued since, based on the obtained r and ϕ , no significant deviations from samples etched for 10 minutes were expected. Due to the different coating used, the signal-to-noise ratio is not directly comparable with the values shown in Figure 33.

Etching duration (minutes)	r (°)	ϕ (°)	Signal-to-noise ratio $v_{as}(\text{CH}_2)$ (2927 cm^{-1}) (°)
6	8.7	0.20	126
8	9.4	0.26	137
10 ¹	8.9 ± 0.8	0.30	
12	11.8	0.21	231
15	14.5	0.24	329

Table 4: Calculated r , ϕ and signal-to-noise ratio of samples etched for different durations in 0.06 M H_2O_2 using BUTS coating. ¹: Data for 10 minutes etching duration taken from series conducted in 4.1.1.1 using OTS coating.

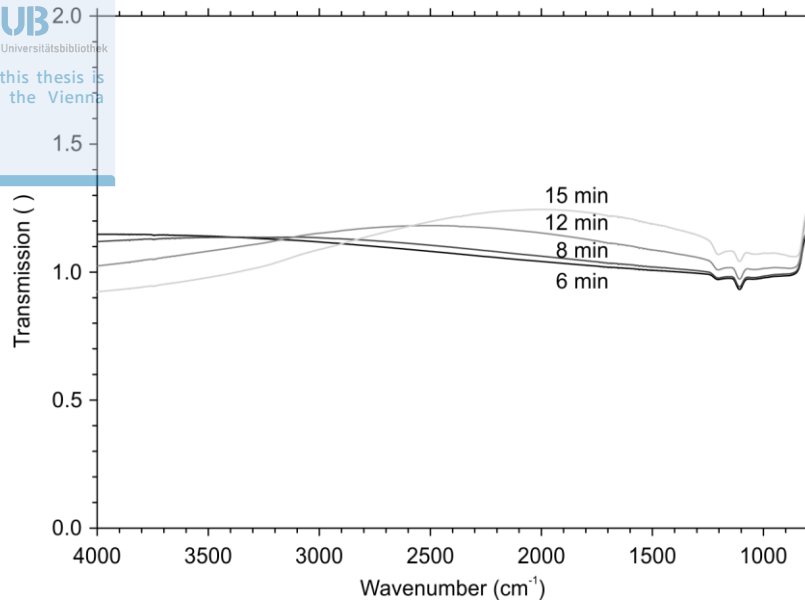


Figure 36: Transmission of infrared light of nanowire covered silicon samples etched for different durations in 0.06 M H_2O_2 and referenced to flat silicon.

Overall, the influence of the etching duration on the nanowire morphology is very similar to the H_2O_2 concentration. Both parameters mainly affect the length of the nanowires and the length then has a major impact on the remaining characteristics, namely roughness, light transmission and bundle formation. However, changes of the H_2O_2 concentration are vastly more pronounced and overshadow any influences of the etching duration. The etching duration for further samples have therefore been kept at 10 minutes because of practical reasons. 10 minutes are short enough to allow continuous work for optimized throughput while being long enough to tolerate deviations of a few seconds without huge impact on the nanowires.

4.1.1.3 Determination of Silver and Hydrogen Peroxide Consumption

In addition to the optimization of the etching conditions, also some process optimization was done. The goal was to minimize the consumed chemicals while maintaining an optimized nanowire structure. In the sample preparation described in 3.2.1 and 3.2.2, most employed chemicals are used in high excess since they are used for cleaning or are intended for quantitative conversion. The only two exceptions are the amount of silver in solution during the deposition of silver right before etching and the H_2O_2 concentration during the etching itself. In order to reuse either solution, the respective chemical has to be replenished since notable consumption is expected during treatment of a sample. Some experiments were therefore performed to determine the necessary replenishment.

Regarding the silver concentration, initially two series of samples with 11 mM and 7.2 mM $AgNO_3$ were prepared to confirm the general predicted decrease. For each series, a single solution was

used and the samples were consecutively treated in it. For easier comparison of the results, a constant HF concentration of 6.2 M and a constant etching time of 1 minute was chosen for all experiments in this chapter. The samples were weighed before and after the treatment in the silver solution (Table 5).

Initial AgNO ₃ Concentration (mM)	11	7.2
first sample, Δm (mg)	4.8	2.5
second sample, Δm (mg)	3.1	1.8
third sample, Δm (mg)	2.5	1.3
fourth sample, Δm (mg)		0.9

Table 5: Decline in weight gain due to the treatment in silver solution when no additional silver is added.

It was confirmed that the precipitated amount of silver decreases. For a deeper understanding a sample treated with silver (5 mM AgNO₃) was examined in SEM (Figure 37).

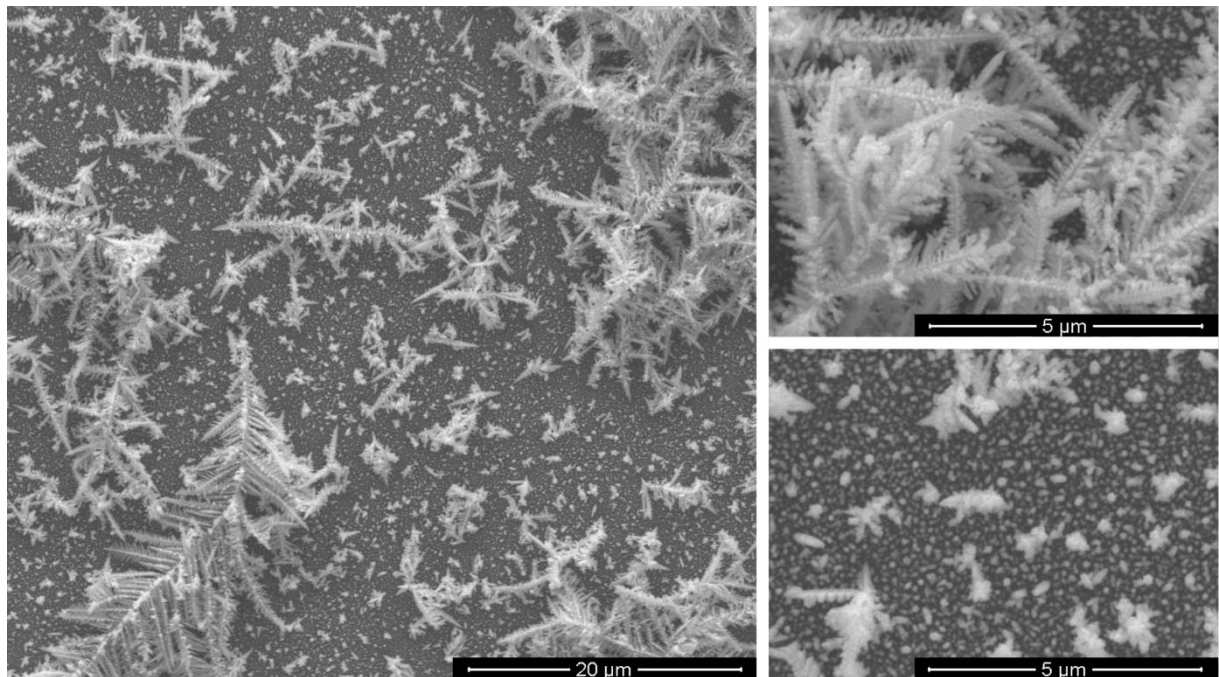


Figure 37: Top-view SEM images of a sample treated with silver (5 mM, 1 minute) solution with two details at higher magnification of silver nanoparticles (bottom right) and silver dendrites (top right).

It can be seen that the silver is present on the surface in two different forms. On the one hand, there are nanoparticles covering the whole surface, on the other hand there are also silver dendrites. Judging from the pores observed in the pictures in the previous chapters, only the nanoparticles participate in the etching process while the dendrites neither participate nor disturb the etching. However, the presence of the dendrite structures indicates that, in fact, also the silver is in excess, at least at the initial concentration. Overall, this means that the requirements for the replenishment are not very high.

To determine the replenishment, three samples were treated each in a fresh solution and weighed before and after the deposition of silver. A weight increase of 1.17 ± 0.12 mg was observed. Since the weight increase can only be due to precipitated silver, an according amount of silver (1 mg) was added after each sample in the form of AgNO_3 (1.57 mg) to compensate for it.

For the H_2O_2 concentration a similar approach was used. This time, in addition to the weight change, also IR spectra were used since a correlation between etching conditions and IR transmission was observed. Here initially six samples were etched each in a fresh 0.06 M H_2O_2 solution and were weighed before and after the procedure. Over the whole etching process, a weight loss of 3 ± 0.3 mg was observed for these samples. We assumed that the weight loss is due to two factors. The first factor is the silver deposition. Since it is deposited in a metal-assisted etching step, it contributes to the dissolution of silicon. When using the previously determined amount of precipitated silver, the weight loss due to silver can be calculated and subtracted from the overall weight loss. The remaining weight loss was attributed to metal-assisted etching with H_2O_2 as oxidizing agent. Based on Reaction 1, the weight loss could then be recalculated to the consumed amount of H_2O_2 . However, since this reaction summarizes two different mechanisms with different silicon to H_2O_2 ratios of 1:1 and 1:2 no conclusive result could be obtained. Considering these ratios, the consumed amount was calculated to be between 0.01 and 0.02 ml H_2O_2 , 36 wt.%.

In a first approach to replenish the concentration back to 0.06 M, 0.015 ml H_2O_2 , 36 wt.%, was added after each sample. Using this refill, four samples were etching consecutively in the same beaker. The same experiment was performed twice. The very first sample was discarded, since it was etched with a fresh solution. All the other samples showed an average weight loss of 2.20 ± 0.14 mg. Since this was considerably lower than the previously determined 3 ± 0.3 mg, we repeated the experiment with a larger refill.

In a second attempt, we chose to add 0.02 ml H_2O_2 after each sample, which matches the highest calculated H_2O_2 consumption. This time three samples were etched consecutively in each beaker and three identical series were carried out. The first sample of each series was again discarded. For the remaining samples, an overall weight loss of 2.83 ± 0.14 mg was measured which sufficiently fits the determined weight loss.

For further evaluation, the FTIR spectra of the last series were recorded and averaged. Since the intention here is to reproduce 0.06 M H_2O_2 conditions, the averaged FTIR spectra were then compared to the FTIR spectra etched with different H_2O_2 concentrations. (Figure 38).

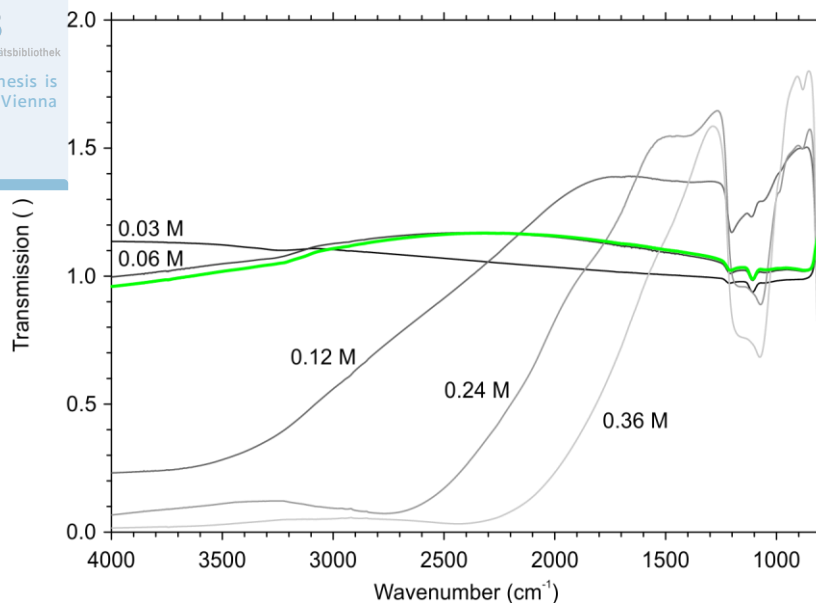


Figure 38: Grey scales: FTIR transmission spectra of nanowire covered silicon samples etched with different H_2O_2 concentrations referenced to flat silicon; Green: Average transmission of samples etched after refilling 0.02 ml H_2O_2 , 36 wt.%, in the etching solution after each sample starting with 0.06 M.

Both, the weight loss as well as the FTIR spectra, indicate that etching always in fresh 0.06 M H_2O_2 solution and etching several samples in the same solution with a 0.02 ml H_2O_2 , 36 wt.%, refill after each sample gives comparable results.

4.1.2 Coating

Beyond a topographic optimization, also the surface composition plays an important role for liquid repellent properties. From Equation 17 and Figure 10 can be seen that a high contact angle on flat surfaces increases the resulting Cassie-Baxter angle and extends the stable region of the Cassie-Baxter state. The Young equation (Equation 1) helps understanding which parameter can be changed to achieve high contact angles on flat surfaces. As explained in 2.1.1, the interface tension, appearing in the Young equation, is usually approximated from surface energy and surface tension of the involved phases. This indicates that the interface energy is not independent from the other two energies. Furthermore, the designed surface should ideally function for a wide range of different probe liquids and therefore for a wide range of surface tensions. Ultimately, the only parameter left in the Young equation to selectively alter to achieve high contact angles is the surface energy. Low surface energies result thereby in high contact angles.

The easiest way to selectively modify the surface energy is to apply a coating. The coating has then to fulfil two major requirements. First and foremost, it has to show a low surface energy, secondly, it should only form a single but complete monolayer. When only a single monolayer is present on the surface, the morphological structure is usually preserved. This allows the independent

optimization of topography and surface energy. If the monolayer is also completely covering the surface, the best control over the surface energy can be achieved since no bare substrate, with most likely undesirable surface energy, is in contact with liquid.

However, the liquid repellent behaviour does not collapse if the coating has some defects. When substrate remains partially uncoated, its influence on the overall contact angle can be calculated analogous to the Cassie-Baxter equation (Equation 17) since in both cases the drop is in contact with a substrate which exhibits two different surface energies. According to the equation, it can be seen that as long as the fraction of uncoated substrate remains small, its influence on the overall contact angle is negligible.

A well-studied and reliable method to coat silicon substrate with organic monolayers is the adsorption of organo-trichlorosilanes [45, 67], which was also used in this work (Figure 39). Briefly, a trichlorosilane is dissolved in an inert solvent and hydrolyses with catalytic amounts of water to form a trisilanol. Upon immersion of a silicon substrate in this solution, the silanol groups react with the surface OH-groups and form siloxane bonds with the surface, by which the organic substituent is covalently attached to the surface and forms an organic monolayer film.

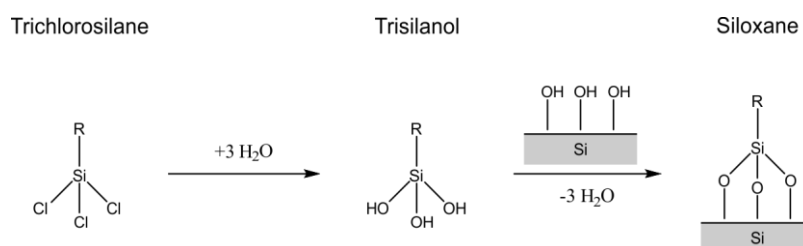


Figure 39: Reaction scheme for covalent coating of silicon substrates with trichlorosilane.

In principle, any substituent, where the corresponding trichlorosilane is stable and can be synthesised, can be used to form a monolayer film. In this work, inert, nonpolar substituents like alkyl or fluorinated alkyl groups, which form low energy surfaces, were of primary interest. Alkyl-trichlorosilanes are commercially available and can be used directly for the corresponding monolayer coating. In this work, we focused on the use of trichloro(octadecyl)silane (OTS) for alkyl modification. Perfluorinated trichlorosilanes, on the other hand, are not commercially available and are very difficult to synthesise. We therefore used a different concept for surface functionalisation with perfluorinated compounds, which is based on copper-catalysed Huisgen 1,3-dipolar cycloaddition reaction between an azide and an alkyne group [66]. To utilize this reaction, we chose to first coat the substrate with a precursor monolayer containing a terminal bromine, in our case 11-bromoundecyltrichlorosilane (BUTS). This bromine was then converted to an azide by treatment with sodium azide. The azide-terminated primer layer was then reacted with a perfluorinated

propionic acid ester, 3,3,4,4,5,5,6,6,7,7,8,8,9,9,10,10,10-heptafluorodecyl propiolate (THFDP)

(Figure 40).

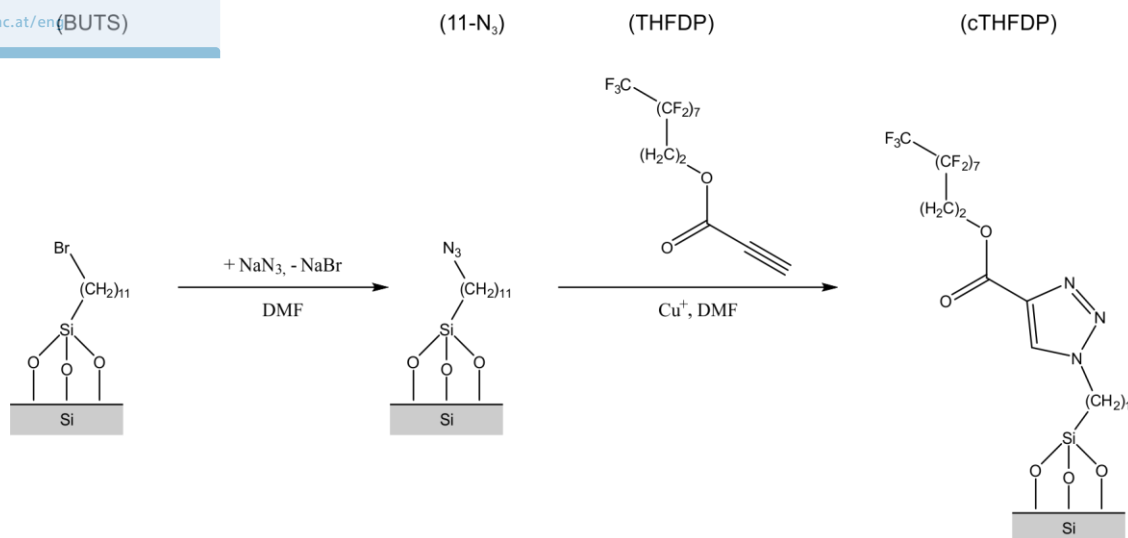


Figure 40: Reaction scheme for surface modification of BUTS coatings with sodium azide and copper catalysed Huisgen 1,3-dipolar cycloaddition of THFDP.

4.1.2.1 Covalent Coating of OTS and BUTS

Initially it was important to confirm that the applied coating actually bonded to the surface and to investigate whether only a monolayer is formed. Subsequent considerations about the surface energy of these coatings will be discussed later in length in chapter 4.1.3.

Starting with BUTS, to determine whether the coating works in principle and to optimize the reaction time for the coating, three series of samples were treated for different durations (1, 4 and 24 hours) in the coating solution. Each series consisted of at least four flat samples and four nanowire samples. Besides the duration, all other parameters for the reaction were kept as presented in 3.2.3. The flat samples were then used for ellipsometry measurements since nanowire sample are not suitable for this method. The obtained layer thickness can be found in Table 6.

Coating duration (h)	Layer thickness (Å)
1	15 ± 2
4	21.2 ± 0.6
24	21.9 ± 1.0

Table 6: Layer thickness of BUTS coated samples as a function of coating duration.

In addition to ellipsometry, the length of the molecule was calculated using Chem3D by determining the distance between the silicon and the bromine atom. The calculated length of 15.6 Å should then correlate with the observed layer thickness if only a single monolayer is present on the surface. The rather large discrepancy between measured and calculated thickness can be explained by the

limited knowledge about the refractive index of the monolayer. As pointed out in 2.2.2, the refractive index of the layer has to be known in order to obtain meaningful experimental values in ellipsometric measurement. However, there is no easy method which allows its determination for thin layers. For the measurements presented here, the refractive index was therefore estimated with 1.5. While the absolute values may not be reliable, some conclusions can still be drawn. First of all, it confirms that there is a layer on top since otherwise the layer thickness would be zero no matter which refractive index is used for the evaluation. Secondly, the relative values are still meaningful since at least they stay constant after 4 hours. The measured layer thickness for 4 and 24 hours, which is virtually the same, confirms therefore that there is no further reaction taking place in this time frame. The only reasonable explanation for this is that the monolayer formation is completed and that the compound does not tend to form multilayers easily. Finally, it can be seen that while the absolute experimental and calculated values differ, they are still in the same order of magnitude. This is another indicator that only a monolayer is formed.

Also, FTIR measurements of the nanowire samples have been performed. They show a similar picture. While here also the integral of the CH stretching region ($2770\text{-}3000\text{ cm}^{-1}$) increases with time, as can be seen in Table 7, the difference between 4 and 24 hours is far less pronounced especially when considering that the time increase is not linear. In addition to the integral, the spectra itself are shown in Figure 41. In this figure, for each duration, the average of the four sample spectra is plotted. Overall, we concluded that for our purpose a complete monolayer coating with BUTS is achieved after 4 hours.

Coating duration (h)	Integral of $2770\text{-}3000\text{ cm}^{-1}$ ()
1	0.38 ± 0.07
4	0.427 ± 0.015
24	0.442 ± 0.018

Table 7: Integral of the CH region ($2770\text{-}3000\text{ cm}^{-1}$) as a function of coating duration.

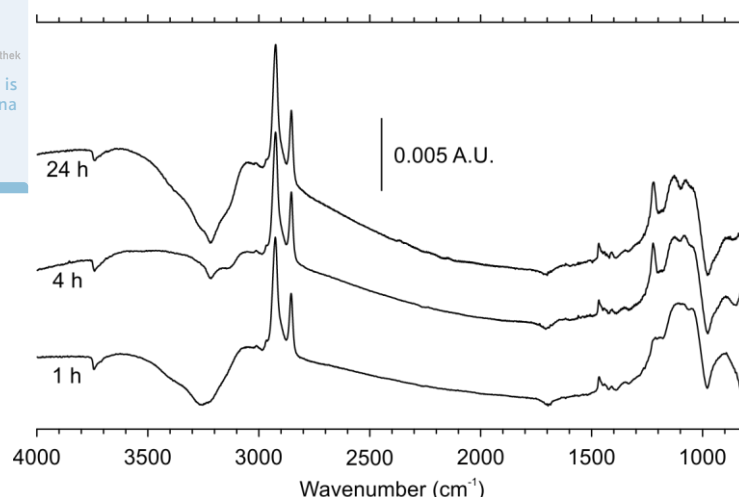


Figure 41: FTIR spectra of nanowire samples treated with a coating solution containing BUTS for different durations, each averaged over three samples.

In a similar fashion, the coating with OTS has been investigated. Again, we chose three different durations for the coating. As before we used 1, 4 and 24 hours. We prepared at least three flat samples for each coating duration with all other parameters according to the procedure presented in 3.2.3. These samples were then investigated with ellipsometry. The obtained layer thicknesses can be found in Table 8.

Coating duration (h)	Layer thickness (Å)
1	26.89 ± 0.16
4	25.9 ± 0.3
24	27.3 ± 0.3

Table 8: Layer thickness of OTS coated samples as a function of coating duration.

We also calculated the length of OTS in Chem3D which resulted in 22.7 Å. It can be seen that already after 1 hour the layer thickness only changes marginally and the measured thickness is again in the same order of magnitude as the calculated one. This leads to the same conclusions which could be drawn for the coating with BUTS. Only a single monolayer is formed on the surface and the formation of the monolayer is largely completed after 1 hour. Nevertheless, for practical reasons we chose to treat the samples for 4 hours like samples coated with BUTS allowing easier work on both coatings at once.

Since no new insights from the FTIR spectra were expected, it was forgone to repeat the whole series with nanowires substrates. Only four samples with the selected conditions of a 4 hour coating duration were prepared and investigated with FTIR. The resulting spectrum, again averaged over all four samples, can be found in Figure 42. The highly characteristic CH-stretching peaks between 2800 and 3000 cm⁻¹ convincingly confirm the presence of OTS on the surface.

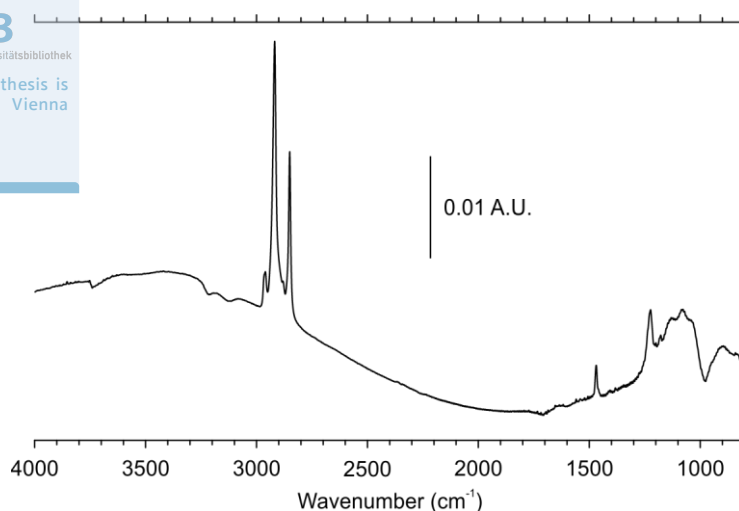


Figure 42: FTIR spectrum of OTS on nanowire substrate, averaged over three samples.

4.1.2.2 Optimization of Sodium Azide Treatment

In order to functionalize the surfaces with azide groups to perform the Huisgen 1,3-dipolar cycloaddition, BUTS coated samples had to be treated with sodium azide. Again, we had to make sure that a high conversion is achieved. Similar as in the previous chapters, we varied the duration of the treatment to find the necessary time for complete conversion. This time we could not use ellipsometry to characterize the reaction progress, because the layer thickness changes only marginally since only the terminal group is replaced but the overall length of the molecule largely stays the same. A change in layer thickness would here likely then be overshadowed by a change in refractive index. Luckily, FTIR measurements promise to be very meaningful in this case. The azide group shows a very strong and sharp peak at 2101 cm^{-1} representing the asymmetric N_3 -stretching vibration. This peak allows easy determination whether full conversion is reached.

Initially we compared the results of 1 hour and 24 hours reaction time. We prepared two nanowire samples for each of the two durations in question. It is necessary to point out that this investigation was done before the optimization of the etching condition. The samples presented here were etched in $0.12\text{ M H}_2\text{O}_2$ solution. Nevertheless, the results are still useful for samples etched with $0.06\text{ M H}_2\text{O}_2$ solution, since, if anything, the bigger surface area due to the higher H_2O_2 concentration increases the necessary reaction time to reach full conversion. At worst, samples etched with $0.06\text{ M H}_2\text{O}_2$ will then be treated unnecessarily long to reach full conversion. The samples were then examined with FTIR. The average integral of the peak between 2020 and 2175 cm^{-1} is listed in Table 9 and the spectra are plotted in Figure 43.

Reaction duration (h)	Integral 2020-2175 cm ⁻¹ ()
1	0.171
24	0.675

Table 9: Time dependency of the integral of the asymmetric stretching vibration of azide after treatment of BUTS coated nanowire samples etched with 0.12 M H₂O₂ for various durations with sodium azide.

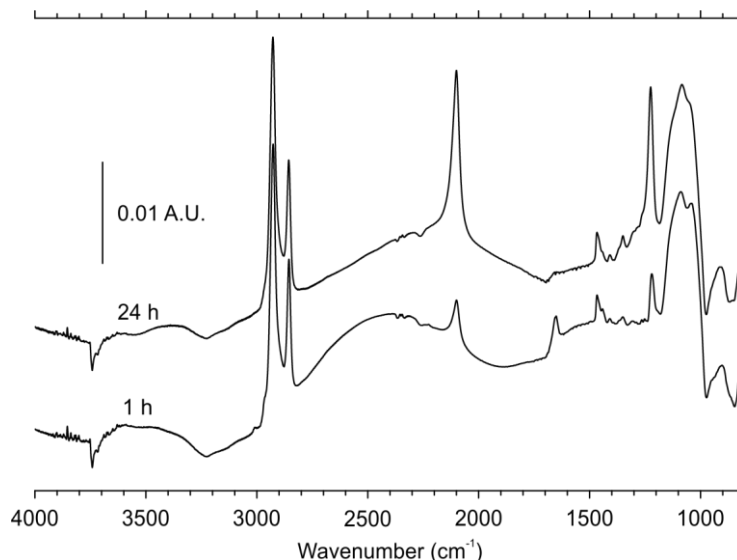


Figure 43: FTIR spectra of BUTS coated nanowire samples etched with 0.12 M H₂O₂ after treatment with sodium azide for various durations, both spectra averaged over two samples.

The results show unambiguously that after 1 hour the reaction is not finished. To further determine if 24 hours are in fact enough we conducted a second series comparing the FTIR spectra of samples treated for 24 and 72 hours. For those series four samples were prepared for each duration. The samples for these series were already etched with 0.06 M H₂O₂. The obtained integrals of the FTIR signals are therefore not comparable with the integrals of the previous series. FTIR spectra were again recorded and evaluated in the same manner. The integral of the asymmetric stretching vibration of the azide (2020-2175 cm⁻¹) is shown in Table 10 and the averaged spectra are shown in Figure 44.

Reaction duration (h)	Integral 2020-2175 cm ⁻¹ ()
24	0.253 ± 0.016
72	0.30 ± 0.05

Table 10: Time dependency of the integral of the asymmetric stretching vibration of azide after treatment of BUTS coated nanowire samples etched with 0.06 M H₂O₂ for various durations with sodium azide.

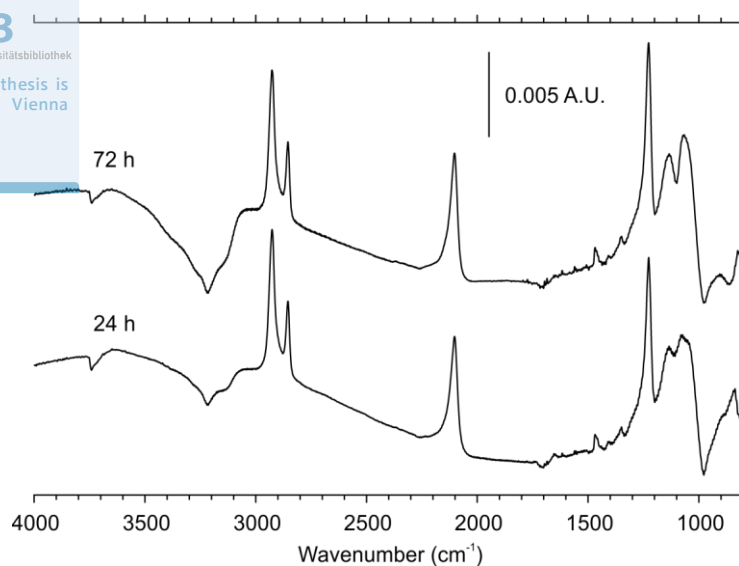


Figure 44: FTIR spectra of BUTS coated nanowire samples etched with 0.06 M H_2O_2 after treatment with sodium azide for various durations, both spectra averaged over four samples.

The spectra showed that 24 hours are sufficient to reach good conversion from BUTS to azide terminated wafers (11-N_3). Although ellipsometry measurements were not used to determine the required treatment duration, for complicity sake four flat samples were prepared and measured. The samples showed a layer thickness of $20 \pm 2 \text{ \AA}$.

4.1.2.3 Synthesis of THFDP and Huisgen 1,3-Dipolar Cycloaddition

For the synthesis of THFDP (Figure 45) we used an esterification of propiolic acid and 1H,1H,2H,2H-perfluoro-1-decanol. The procedure worked very well according to the approach presented in 3.1.1. In order to obtain a FTIR spectrum (Figure 46), the compound was molten ($T_{mp} = 28 \text{ }^\circ\text{C}$) and placed between two sodium chloride windows. Also, an ^1H NMR (Figure 47) was measured.

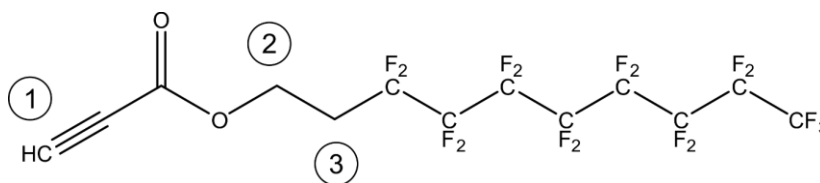


Figure 45: THFDP with labelled CH groups correlating with ^1H NMR peaks shown in Figure 47.

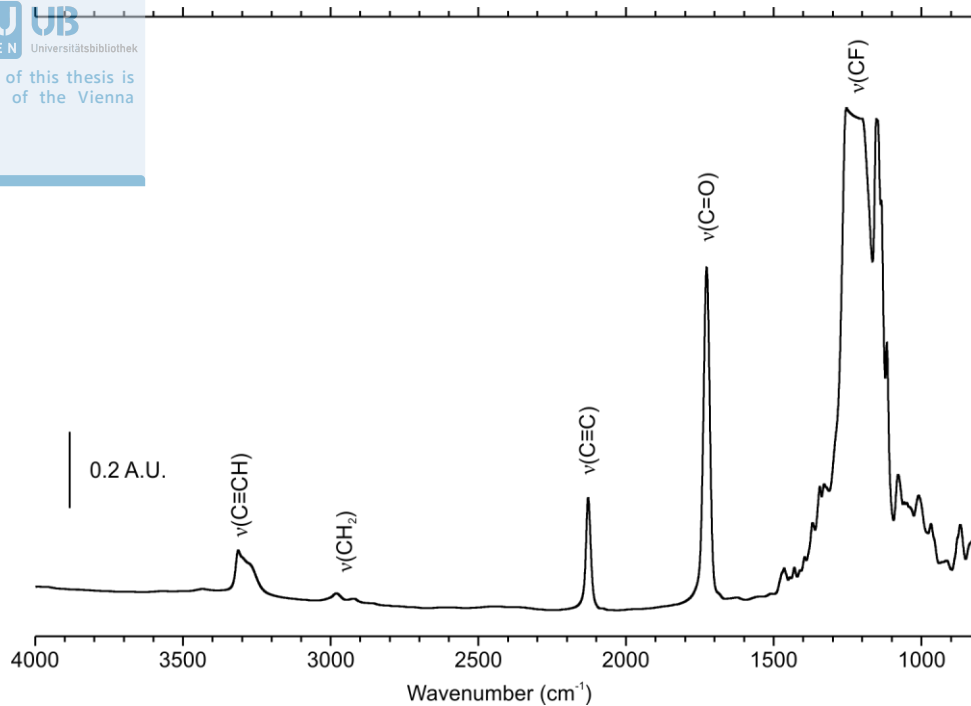


Figure 46: FTIR spectrum of THFDP between two sodium chloride windows.

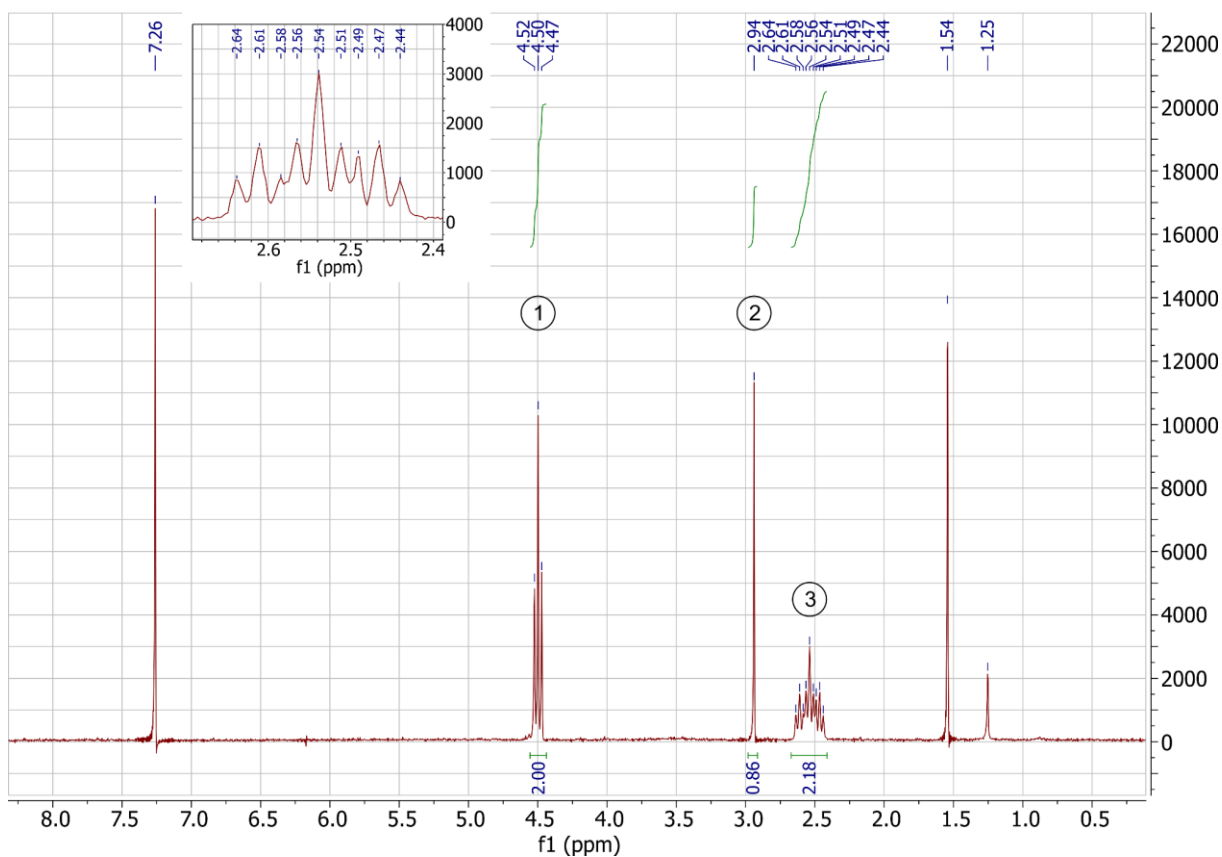


Figure 47: $^1\text{H-NMR}$ of THFDP in CDCl_3 with a magnification of the triplet of triplets at around 2.54 ppm.

$^1\text{H NMR}$ (250 MHz, CDCl_3): $\delta = 2.54$ (tt, $J_1 = 6.6$ Hz, $J_2 = 18.2$ Hz, 2 H), 2.94 (s, 1 H), 4.50 (t, $J = 6.6$ Hz, 2 H) ppm

The spectra showed quite clear that besides residual water and traces of grease the obtained compound was pure and could be used for the modification of an 11-N₃ coating.

The 1,3-dipolar cycloaddition was done according to the procedure presented in 3.2.3 to obtain a layer of 11-N₃ modified with THFDP which will be abbreviated as cTHFDP. A series of four nanowire samples was prepared and investigated with FTIR (Figure 48).

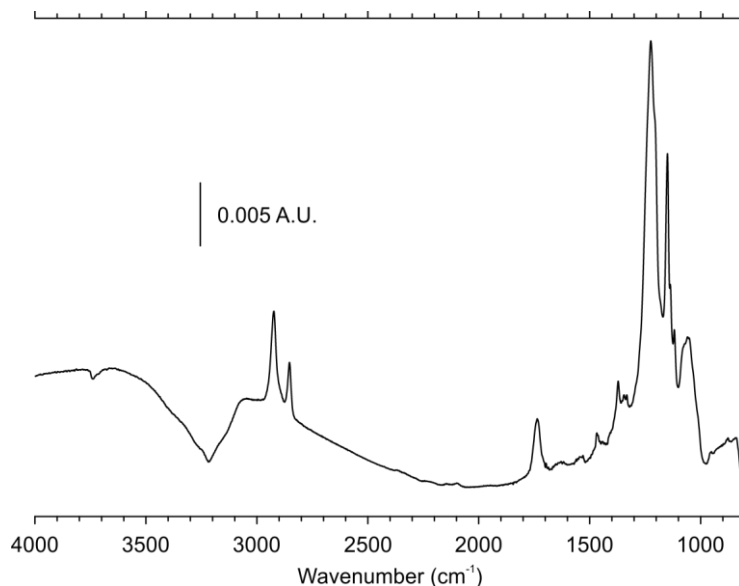


Figure 48: FTIR spectrum of cTHFDP on nanowire substrates, averaged over four samples.

The absence of the asymmetric stretching vibration of the azide at 2101 cm⁻¹ shows quite convincingly that the conversion is complete while the peaks at 1736 cm⁻¹ and around 1200 cm⁻¹, representing the C=O stretching vibration and different CF vibrations, respectively, confirm the presence of cTHFDP on the surface.

For the sake of complete characterization, we also prepared four additional flat samples for layer thickness determination with ellipsometry and compared them again with the calculated length of the molecule with Chem3D. The measured layer thickness of 28.4 ± 0.3 Å indicates that only a monolayer is present and is in reasonable agreement with the calculated length of 31.3 Å.

4.1.3 Wetting Properties of Cassie-Baxter Type Materials

In the next step, we wanted to put our finished Cassie-Baxter systems to the test. The most meaningful way to characterize them is to directly measure the contact angle of different liquids, which allows, with subsequent data analysis, the determination of the surface energy, γ and ϕ according to the equations presented in 2.1. We decided to use water-ethanol mixtures since they are completely miscible, water is mainly polar and shows high surface tension while ethanol is

mainly dispersive and shows low surface tension. Mixtures then cover a wide range of surface tension and polarity. However, we recognized very soon that the conditions for the contact angle measurements had to be precisely controlled to get proper results. Most importantly, evaporation of the probe liquid poses a major problem. This is especially true since we are using a mixture of two liquids. In our case, evaporation will not only change the volume of the drop but also its composition and therefore its surface tension.

4.1.3.1 Influence of Liquid Evaporation on Contact Angle Measurements

To confirm whether evaporation really is as problematic as we expected it to be, we placed a 15 μl drop of a water-ethanol mixture on top of an OTS coated nanowire surface and determined the volume of the drop with the contact angle goniometer over the course of 30 minutes. The water-ethanol mixture was chosen from a set of different mixtures which we also planned to use for the characterization of the surfaces. Further details about the water-ethanol mixtures will be presented in 4.1.3.2. To investigate the evaporation behaviour, we wanted to use the mixture which will be susceptible the most to it, because if we get it under control for this liquid, it will also be unproblematic for all other mixtures. Therefore, we selected a mixture with relatively high ethanol content but with a surface tension high enough so that the drop still shows rather high contact angles. The curvature of the drop will then also contribute to an even higher evaporation rate. The rather high contact angle also helps to get meaningful volume measurements, since for drops with a contact angle close to 0° the determination of the volume becomes less accurate. We chose a mixture containing 30.04 wt.% ethanol and showing a surface tension of $33.3 \pm 0.4 \text{ mJ/m}^2$. The measured decrease of the drop volume over time as well as a picture of the drop right after placing it on the surface and another one after 30 minutes can be shown in Figure 49.

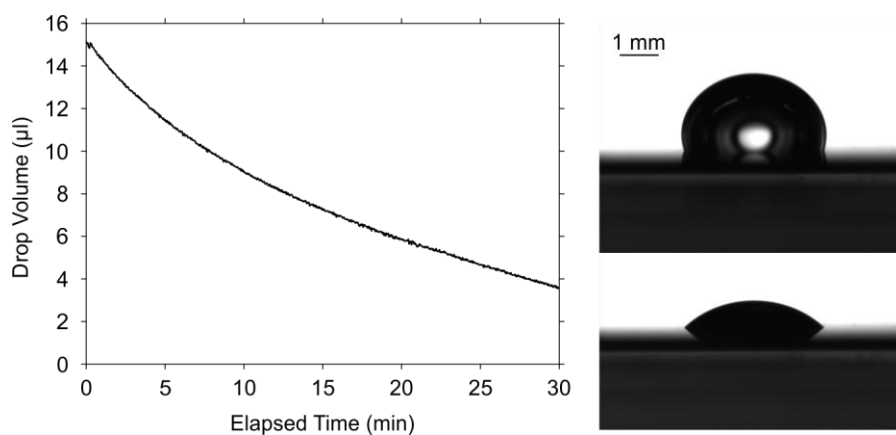


Figure 49: Evaporation of a drop without extra precautions. Left: Decrease of drop volume of a mixture of 69.96 wt.% water and 30.04 wt.% ethanol as a function of time due to evaporation; Top right: Drop at the beginning of the measurement; Bottom right: Drop at the end of the measurement.

Evaporation is a considerable problem, becoming more severe the longer the measurement takes. By doing fast measurements the problem can somewhat be diminished. However, it was also planned to measure advancing and receding contact angles. Here, in general, can be said that a measurement becomes more precise with slower tilting rate because then the drop has more time to reach equilibrium for a specific tilting angle, favouring slower experiments. To avoid these opposing trends and be able to do proper measurements, the obvious solution is to restrain evaporation enabling slower tilting rates. Therefore, we decided to build a sample housing to be able to saturate the atmosphere around the drop with probe liquid to slow down evaporation. A 3D model of the sample housing was drawn with a CAD program and then 3D printed. A rendering of the model as well as a picture of the printed housing is shown in Figure 50 and Figure 51, respectively.

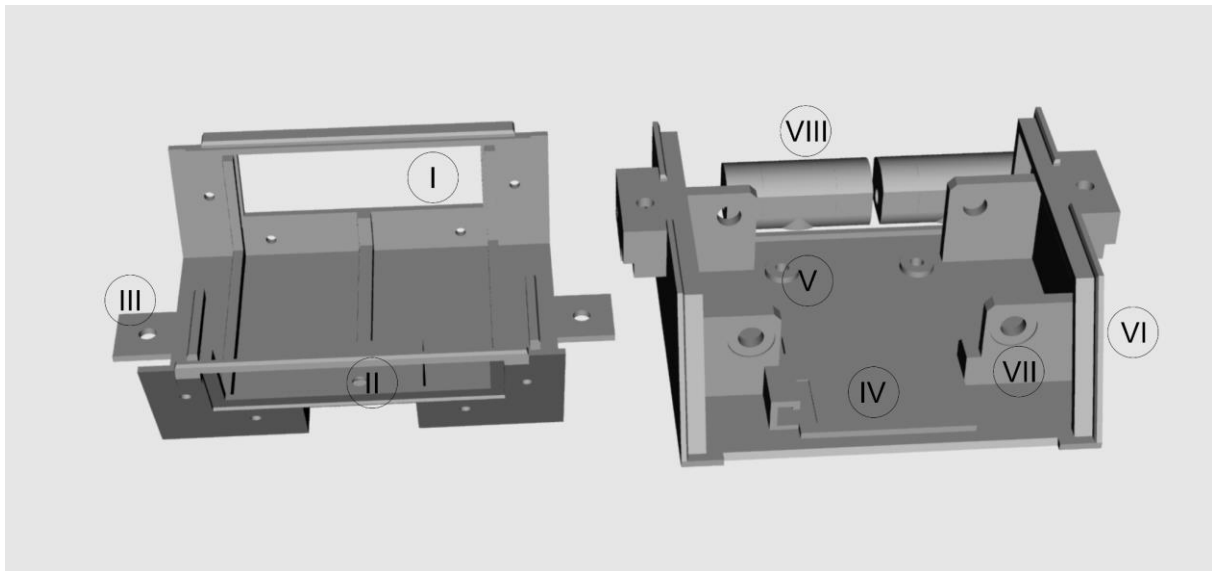


Figure 50: Rendered 3D model of the sample housing used to obtain an atmosphere saturated with probe liquid around the drop of probe liquid for contact angle measurements.

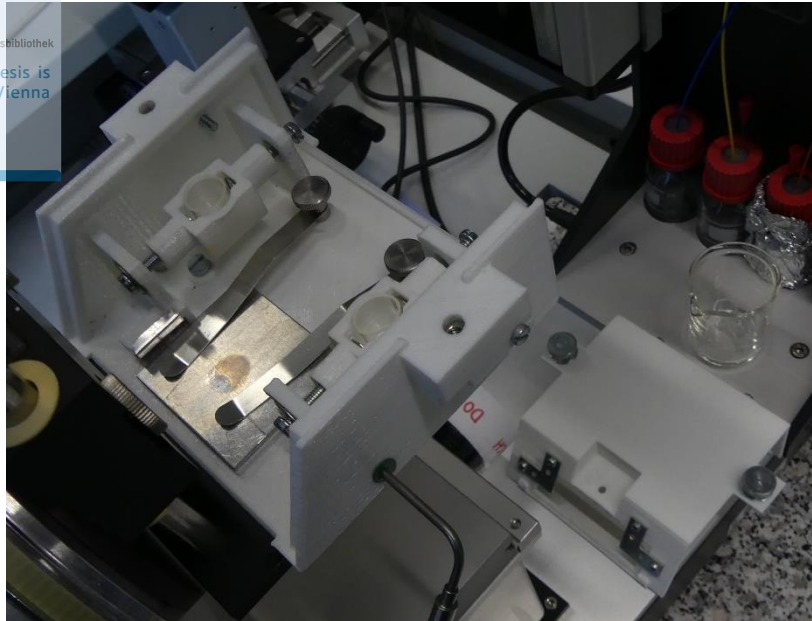


Figure 51: Picture of the 3D printed housing mounted on the sample stage of the goniometer.

The housing consists of four parts. The top part (left in Figure 50) mainly features two large holes to mount glass slides as windows for the measurement (I) and a small hole in the middle to allow the needle the placement of drops on the sample (II). It also has two holes to mount the top on the bottom with screws (III) which is especially important when tilting the samples stage. The bottom part (right front in Figure 50) is screwed to the sample stage of the device. The most important part here is an elevation in the middle to support the sample (IV). After printing, this was further reinforced with an aluminium plate to avoid direct contact of samples with plastic used for 3D printing. In the back are two holes for clamps to fixate the samples in place (V). The bottom has a hole in the side for a temperature probe (VI, not visible in Figure 50 but in Figure 51) and, finally, a suspension (VII) for the remaining two parts. The final two parts (VIII, right back in Figure 50), which can swing freely in the suspension of the bottom part, can carry small beakers. These parts are also heavier on the bottom, which forces the beakers to always stand upright, regardless of the tilt of the sample stage. This way the beakers can be filled with probe liquid during the whole measurement to saturate the housing. In order to do a measurement, the beakers were filled with probe liquid and the sample was mounted on the aluminium plate with the two clamps. The housing was then kept closed for 30 minutes to allow the liquid inside of the beakers to evaporate. After this period, the drop for the measurement was placed on the sample through the hole in the top and the measurement was conducted as usual.

To compare the effects of the housing, an identical evaporation test was done as before but this time with the drop in the housing. The resulting decrease in drop volume as well as a picture before and after the test of the drop can be found in Figure 52.

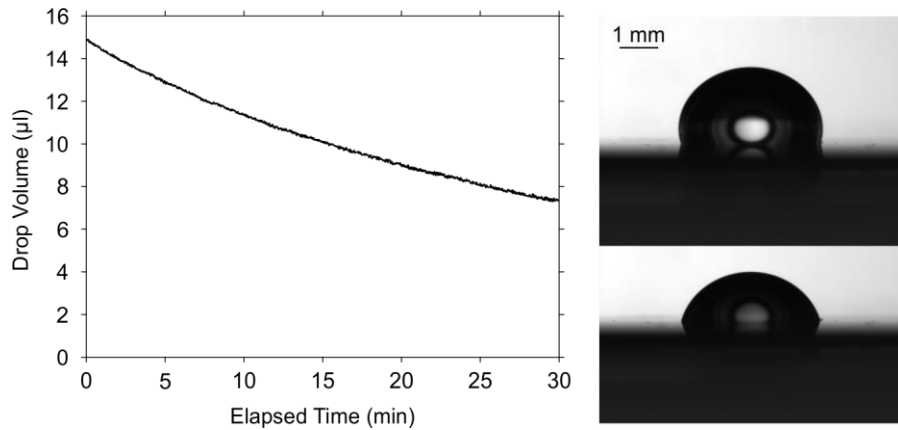


Figure 52: Evaporation of a drop in a housing. Left: Decrease of drop volume of a mixture of 69.96 wt.% water and 30.04 wt.% ethanol as a function of time due to evaporation; Top right: Drop at the beginning of the measurement; Bottom right: Drop at the end of the measurement.

The evaporation over the course of 30 minutes is still noticeable, but it is slowed down. Due to the curvature of the drop, evaporation cannot be completely inhibited solely by saturating the atmosphere with probe liquid with the exact same composition also being used afterwards for the measurement. To get meaningful results from contact angle measurement with water-ethanol mixtures, we decided for a tilting rate of 30°/min. This way a measurement can only take up to 3 minutes but often much less if the drop rolls off early. In this time frame the drop volume decreases by 1.2 µl in the housing. Without a housing, the decrease is, with 2.4 µl, exactly twice as much.

4.1.3.2 Contact Angle Raw Data

As already mentioned, we then characterized our surfaces with contact angle measurements using water-ethanol mixtures. Water has a high surface tension ($\gamma_l = 72.75 \text{ mJ/m}^2$ at 293 K)[68] while the surface tension of ethanol is relatively low ($\gamma_l = 22.31 \text{ mJ/m}^2$ at 293 K)[68]. Since they are completely miscible, it is possible to prepare mixtures with any surface tension in between. This is very convenient when the contact angle as a function of the surface tension is sought after. For our measurements, we decided to use a total of 10 probe liquids distributed evenly over the accessible range. Therefore, we used pure water and ethanol and 8 additional mixtures. The precise mixing ratios could thereby be determined based on literature data [68]. In this paper, the surface tension of water-ethanol mixtures was presented at various compositions and temperatures. An excerpt of the data at 293 K taken from this publication [68] is listed in Table 11 and a corresponding plot is shown in Figure 53.

Ethanol (wt.%)	Surface tension at 293 K (mJ/m ²)
0	72.75
5	56.41
10	48.14
15	42.72
20	38.56
25	36.09
30	33.53
40	30.69
50	28.51
60	26.72
70	25.48
80	24.32
90	23.23
100	22.31

Table 11: Surface tension of water-ethanol mixtures as a function of composition [68].

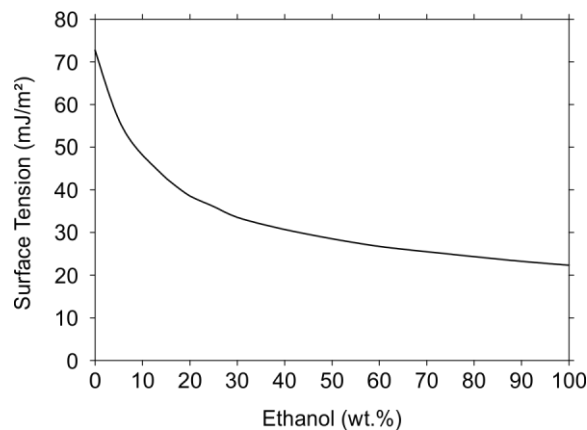


Figure 53: Surface tension of water-ethanol mixtures as a function of composition [68].

Then we used the data to interpolate the ethanol content necessary for a desired surface tension. We prepared mixtures according to the calculated values and measured their density, which is needed for the determination of their surface tension. The surface tension was measured with the pendant drop method described in 3.3.3. It was determined for each probe liquid three times and then the average was formed. All information about the intended composition and the characterization of the probe liquids can be found in Table 12.

Intended surface tension (mJ/m ²)	Ethanol (wt.%)	Density (g/cm ³)	Measured surface tension (mJ/m ²)
72.75	0.00	0.997	72.9 ± 0.9
67.15	1.71	0.993	64 ± 0.8
61.54	3.43	0.991	59.5 ± 0.3
55.94	5.29	0.988	55.6 ± 0.3
50.33	8.67	0.982	50.6 ± 0.3
44.73	13.15	0.975	45.2 ± 0.7
39.12	19.32	0.966	39.57 ± 0.12
33.52	30.04	0.950	33.3 ± 0.4
27.91	53.33	0.906	27.4 ± 0.2
22.31	100.00	0.800	23.03 ± 0.06

Table 12: Composition and characterization of the water-ethanol mixtures used as probe liquids for contact angle measurements.

With the probe liquids at hand, we could then proceed to characterize our surfaces. We decided to investigate three different coatings: cTHFDP because we expected for it the lowest surface energy, 11-N₃ because its wetting properties are of interest for the 1,3-dipolar cycloaddition and finally OTS because it is also expected to show a relatively low surface energy but can be obtained by direct adsorption in a single step. All three coatings were applied on flat surfaces and on nanowire substrates. For each combination three different samples were investigated. The measured contact angles are listed in Table 13.

Probe liquid (mJ/m ²)	θ	OTS	cTHFDP	11-N ₃	OTS	cTHFDP	11-N ₃
		flat (°)	flat (°)	flat (°)	NW (°)	NW (°)	NW (°)
72.9 ± 0.9	θ	112.6 ± 1.3	119.6 ± 0.3	91 ± 2	163 ± 1	168 ± 3	144 ± 2
	$\theta_{rec.}$	105.2 ± 0.6	103.5 ± 1.6	80.4 ± 1.2	150 ± 2	154 ± 3	
	$\theta_{adv.}$	113.3 ± 0.6	121 ± 2	92.0 ± 1.0	165.3 ± 0.4	168.1 ± 1.6	
64 ± 0.8	θ	110.2 ± 1.3	116.6 ± 0.5	88.3 ± 1.4	163.1 ± 1.3	163.8 ± 0.5	135.3 ± 1.4
	$\theta_{rec.}$	104 ± 4	102.0 ± 1.8	74 ± 3	146.4 ± 0.2	152.1 ± 0.6	
	$\theta_{adv.}$	111.1 ± 1.4	120.8 ± 0.8	89 ± 4	167.4 ± 1.4	168 ± 3	
59.5 ± 0.3	θ	109.2 ± 0.7	114.7 ± 0.4	89.0 ± 0.5	160 ± 3	165 ± 3	130 ± 3
	$\theta_{rec.}$	103.1 ± 1.1	100.0 ± 0.7	75 ± 5	148 ± 3	152.7 ± 1.9	
	$\theta_{adv.}$	109.2 ± 1.2	118.8 ± 1.1	90.8 ± 0.6	165.4 ± 0.4	168 ± 3	
55.6 ± 0.3	θ	103.1 ± 0.6	112.5 ± 1.3	86.3 ± 1.5	157.8 ± 1.8	162.0 ± 0.5	127.3 ± 0.4
	$\theta_{rec.}$	95.3 ± 1.8	99.3 ± 1.9	71 ± 5	145 ± 2	151 ± 2	
	$\theta_{adv.}$	106.1 ± 0.4	118.3 ± 0.3	90 ± 4	170 ± 4	170.3 ± 1.0	
50.6 ± 0.3	θ	100.7 ± 0.2	108.5 ± 0.9	81.1 ± 1.5	157.9 ± 1.4	161.7 ± 0.3	119.1 ± 1.9
	$\theta_{rec.}$	94.3 ± 0.6	92 ± 4	60 ± 7	142.4 ± 1.3	148 ± 2	
	$\theta_{adv.}$	100 ± 4	115.3 ± 0.2	86 ± 5	165.4 ± 1.1	170.7 ± 1.2	
45.2 ± 0.7	θ	96 ± 1	104.1 ± 1.2	75.6 ± 1.1	157 ± 4	158.7 ± 1.8	105 ± 5
	$\theta_{rec.}$	86 ± 2	87 ± 3	58.8 ± 1.6	133 ± 2	142 ± 7	
	$\theta_{adv.}$	96.8 ± 0.4	109.6 ± 1.6	87.3 ± 1.3	170 ± 3	166.7 ± 0.4	
39.57 ± 0.12	θ	86 ± 3	100 ± 2	61 ± 6	150.6 ± 1.1	158.5 ± 0.4	60 ± 30
	$\theta_{rec.}$	78 ± 2	79 ± 3	45.6 ± 0.3	0	128 ± 6	
	$\theta_{adv.}$	90.8 ± 1.1	105.17 ± 0.12	79 ± 6	151 ± 13	167.8 ± 1.2	
33.3 ± 0.4	θ	75.8 ± 0.7	92.9 ± 0.4	56 ± 5	121.3 ± 1.1	155.9 ± 1.8	0
	$\theta_{rec.}$	64.8 ± 0.2	73.2 ± 1.8	25 ± 3	0	98 ± 6	0
	$\theta_{adv.}$	79.2 ± 0.4	96.9 ± 0.8	70 ± 4	125.4 ± 1.2	167 ± 2	0
27.4 ± 0.2	θ	62.4 ± 0.3	81 ± 3	24 ± 6	93.4 ± 0.7	140.6 ± 0.8	0
	$\theta_{rec.}$	59 ± 3	64 ± 2		0	0	0
	$\theta_{adv.}$	63.9 ± 0.7	88 ± 2		90 ± 7	138 ± 5	0
23.03 ± 0.02	θ	37.8 ± 0.5	66.2 ± 1.0	9.7 ± 0.5	0	113 ± 2	0
	$\theta_{rec.}$	35 ± 2	50.1 ± 1.1		0	0	0
	$\theta_{adv.}$	42 ± 2	67.7 ± 1.3		0	116 ± 2	0

Table 13: Measured contact angles (θ) as well as receding ($\theta_{rec.}$) and advancing ($\theta_{adv.}$) contact angles of different probe liquids on flat and nanowire (NW) substrates coated with different compounds.

The few empty spaces of the table, which all refer to either advancing or receding contact angles, could not be determined because the drop did not start moving even when the sample stage was tilted to 90°. In a few cases, the observed contact angle directly after placing the drop is larger than the advancing or smaller than the receding contact angle. This can be explained with the different methods used to fit the contour of the drop when measuring advancing and receding (tangent method) in contrast to the sessile drop (Young-Laplace method). An explanation of the methods

can be found in 2.2.3 and 3.3.3. A graphical representation of the data in Table 13 on flat surfaces can be seen in Figure 54 while the data on nanowire substrates are plotted in Figure 55.

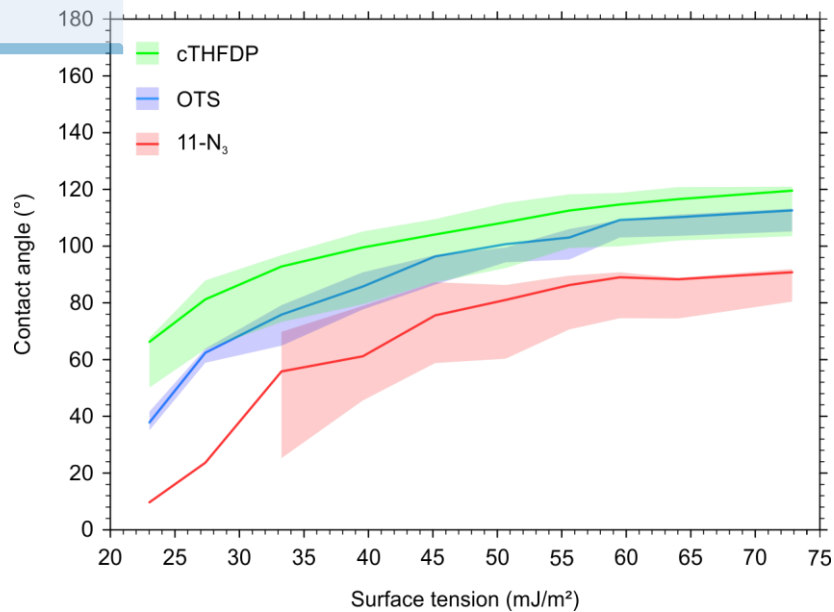


Figure 54: Contact angle of different probe liquids on cTHFDP, OTS and 11-N₃ modified flat surfaces as a function of surface tension. Range between advancing and receding angle is semi-transparently coloured.

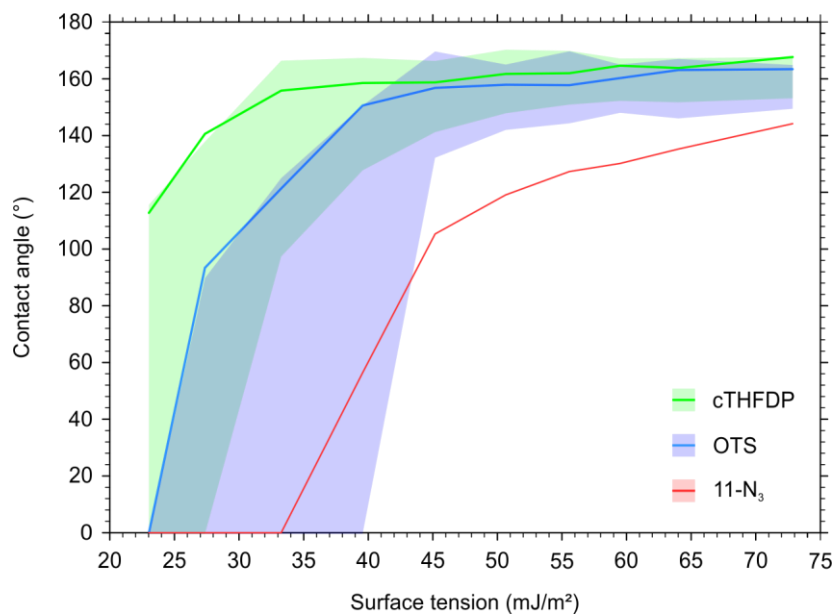


Figure 55: Contact angle of different probe liquids on cTHFDP, OTS and 11-N₃ modified nanowire surfaces as a function of surface tension. Range between advancing and receding angle is semi-transparently coloured.

To give a better idea of the contact angles observed, a few selected images captured during the measurement are shown in Figure 56.

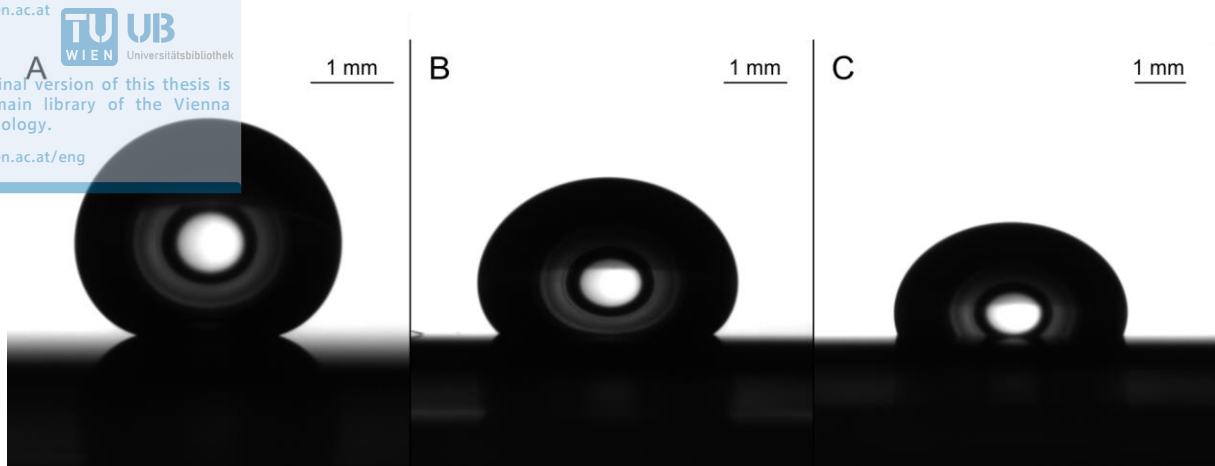


Figure 56: Images captured during contact angle measurements of different probe liquids on cTHFDP coated nanowire substrates. A: Pure water ($\gamma_l = 72.9 \pm 0.9 \text{ mJ/m}^2$); B: A mixture of 53.33 wt.% ethanol and 46.67 wt.% water ($\gamma_l = 27.4 \pm 0.2 \text{ mJ/m}^2$); C: Pure ethanol ($\gamma_l = 23.03 \pm 0.02 \text{ mJ/m}^2$).

4.1.3.3 Surface Energy Calculation

With the contact angle measurements at hand, it was then possible to calculate the surface energy of the different coatings. One way to do this, as presented in 2.1.2, is the Owens-Wendt method. Here the equation given by the combination of the OWKR-approximation and the Young equation of two measurements with different probe liquids is solved for γ_s^d and γ_s^p (Equation 11 and 12). The parameters needed for this evaluation are the measured contact angles and the polar and dispersive surface tension components of the probe liquids. Out of the ten probe liquids we used, only for pure water and pure ethanol the polar and dispersive components are easily accessible from literature but this is sufficient to do this evaluation. The dispersive and polar surface tension components found in literature and used for the calculation were $\gamma_l^d = 21.8 \text{ mJ/m}^2$ and $\gamma_l^p = 51.0 \text{ mJ/m}^2$ for water [58] and $\gamma_l^d = 19.0 \text{ mJ/m}^2$ and $\gamma_l^p = 3.3 \text{ mJ/m}^2$ for ethanol [60]. With those we could calculate the surface energies as presented in Table 14.

Coating	γ_s (mJ/m ²)	γ_s^d (mJ/m ²)	γ_s^p (mJ/m ²)
cTHFDP	12.041 ± 0.004	11.938 ± 0.002	0.103 ± 0.003
OTS	20.24 ± 0.02	20.20 ± 0.02	0.040 ± 0.004
11-N ₃	22.33 ± 0.05	16.83 ± 0.05	5.493 ± 0.009

Table 14: Calculated surface energy of cTHFDP, OTS and 11-N₃ using the Young equation and the OWKR-approximation.

In addition to the Owens-Wendt approach, we also used the Zisman plot, which is explained in 2.1.2, for evaluation of the data presented in 4.1.3.2. The advantage of this method is that no information about the polar and dispersive components of the probe liquid is necessary, so all mixtures presented in Table 13 can be used. On the other hand, no information about the polar and dispersive components of the surfaces is obtained in the process. The most meaningful way to apply

the Zisman plot, is to use probe liquids and surfaces with just one kind of interactions on the interface. Then the data can be fitted according to Equation 15 resulting in a linear relation with an abscissa of -1. However, in our case the probe liquids contained water which shows polar and dispersive interactions. Therefore, it does not fulfil the requirements of the Berthelot hypothesis over the whole range on which Equation 15 is based. In Figure 57 it can be seen that the requirements are indeed not sufficiently met to approximate the behaviour with Equation 15. Satisfactory linear correlations are obtained with neither of the three coatings.

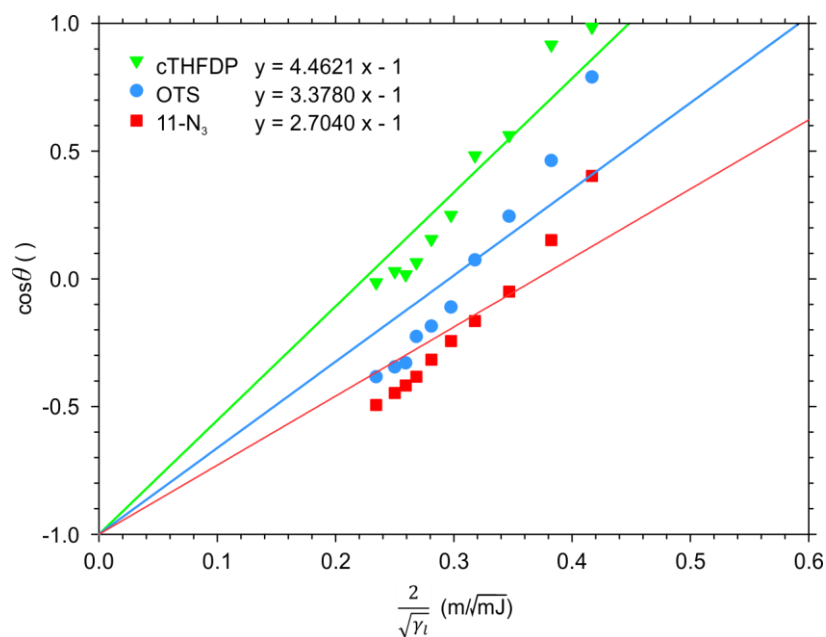


Figure 57: Zisman plot assuming that the Berthelot hypothesis is valid over the whole range.

Another possibility is to plot instead $\cos\theta$ against γ_l and use a polynomial regression curve. We tried to do this with a cubic polynomial (Figure 58) which fits our data reasonably well but it lacks theoretical background and, especially when extrapolation is involved, significant errors may be introduced.

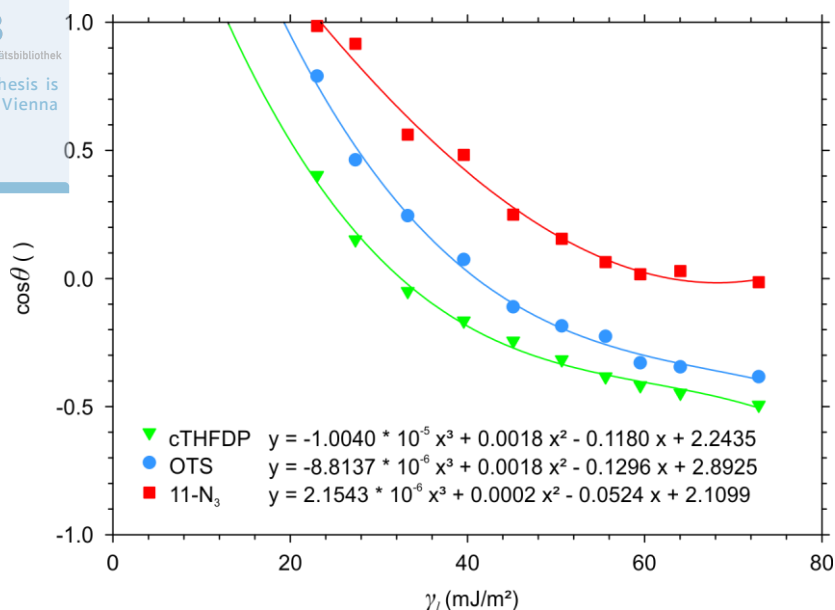


Figure 58: Zisman plot using a cubic polynomial to extrapolate to $\cos\theta = 0$.

In summary, the calculated values with these two methods are listed in Table 15.

Coating	Berthelot - γ_l ($\theta = 0^\circ$) (mJ/m ²)	cubic polynomial - γ_l ($\theta = 0^\circ$) (mJ/m ²)
cTHFDP	7.31	12.89
OTS	11.41	19.28
11-N ₃	19.91	23.93

Table 15: Calculated surface tension to reach a contact angle of 0° on different surfaces using on one hand the Berthelot equation and on the other hand a cubic polynomial to extrapolate the data.

However, for the final evaluation, we wanted to use instead a model which shows a linear relation of some kind with good theoretical background similar to Equation 15. The reason this is not possible with Equation 15, is that the Berthelot hypothesis is not valid over the whole range. However, the very similar OWKR approximation is applicable. Analogous to Equation 15, we therefore tried to incorporate the OWKR approximation into the Young equation and form a linear relation allowing to extrapolate our data. Using this approach, the following equation was obtained (Equation 53).

$$\frac{(\cos\theta+1)\gamma_l}{2\sqrt{\gamma_l^p}} = \sqrt{\gamma_s^d} \sqrt{\frac{\gamma_l^d}{\gamma_l^p}} + \sqrt{\gamma_s^p} \quad (53)$$

To plot data according to this equation, knowledge of the polar and dispersive components of the surface tension is required. To still be able to use this equation with our data, an assumption had to be made. We assumed that the overall surface tension is a linear combination of the surface tension of water and ethanol with a weighting factor characteristic for the composition at the

surface. Thus, from the measured surface tensions the share of water and ethanol on the surface can be calculated. We further assumed that the polar and dispersive components of the mixture are also a linear combination of those of water and ethanol dependent only on the composition of the surface. Therefore, the weighting factors we obtained from the surface tension could be reused to calculate the polar and dispersive share. A graphical presentation of this assumption is shown in Figure 59.

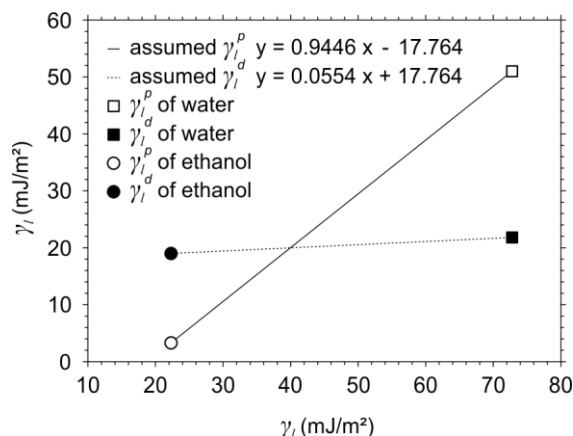


Figure 59: Assumed polar and dispersive components for water-ethanol mixtures calculated from pure water and pure ethanol.

With these values, we were then able to plot our data according to Equation 53 and fit linear curves (Figure 60).

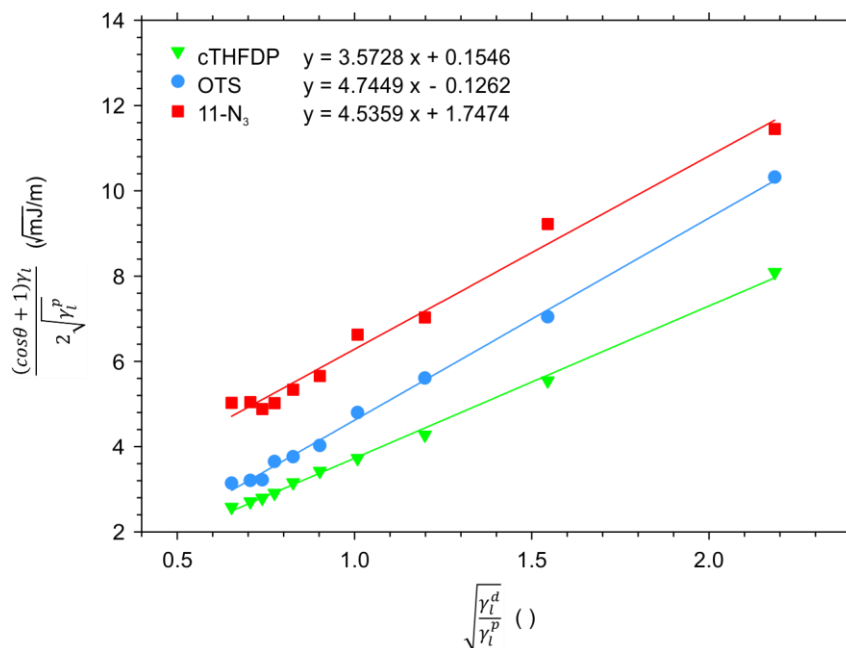


Figure 60: Zisman plot based on the OWKR approximation and the assumption for the polar and dispersive share of water-ethanol mixtures.

These curves can be evaluated in two different ways. First of all, if the assumption we used is correct, which is indicated by the good linear correlations in Figure 60, the slope and the abscissa of the calculated curves can be directly converted to the polar and dispersive components of the surface energies. The corresponding values are listed in Table 16. The negative abscissa for the equation describing OTS in Figure 60 is an artefact but it is sufficiently close to zero to assume that the polar component of this coating in fact is zero and the abscissa is negative only due to small variance of the data.

Coating	γ_s (mJ/m ²)	γ_s^d (mJ/m ²)	γ_s^p (mJ/m ²)
cTHFDP	12.79	12.76	0.02
OTS	22.51	22.51	0
11-N ₃	23.63	20.57	3.05

Table 16: Calculated surface energy from a linear fit based on contact angle measurements plotted according to the OWKR approximation in combination with the Young equation and an approximation of γ_l^d and γ_l^p .

The second way is to merely use these curves as a tool to extrapolate the data to calculate γ_l at a contact angle of 0° and then do the interpretation according to the regular Zisman plot. To do this, Equation 53 at $\theta = 0^\circ$ can be rewritten as Equation 54 and then the slope and abscissa from the fitted curves presented in Figure 60 as well as the approximations for γ_l^d and γ_l^p can be used to calculate γ_l . The calculated values for γ_l using this approach are listed in Table 17.

$$\gamma_l = \sqrt{\gamma_s^d \gamma_l^d} + \sqrt{\gamma_s^p \gamma_l^p} \quad (54)$$

Coating	γ_l ($\theta = 0^\circ$) (mJ/m ²)
cTHFDP	15.43 ± 0.28
OTS	20.47
11-N ₃	23.47

Table 17: Calculated surface tension to reach a contact angle of 0° on different surfaces using the OWKR approximation in combination with the Young equation and an approximation of γ_l^d and γ_l^p .

These data require some discussion. From the previous evaluation methods, we know that 11-N₃ coated surfaces feature, besides the omnipresent dispersive component, also a non-negligible polar component of their surface energy. This already means that, no matter which probe liquid is used, two different kinds of interactions are responsible for the surface energy and therefore the Berthelot hypothesis is not applicable at any point. Beyond that, a water-ethanol mixture with a calculated γ_l of 23.47 mJ/m² would still show some polar component of its surface tension, further disqualifying the Berthelot hypothesis here. Overall this means γ_{sl} has to be greater than zero when

applying Equation 13 and therefore γ_s of the 11-N₃ surface has to be greater than the value of γ_l calculated here to reach a contact angle of 0°.

This is different for OTS coated surfaces. In the other evaluation methods, OTS shows virtually no polar component and also a theoretical probe liquid with a surface tension of 20.47 mJ/m² would show only very little polar properties using the presented approximation. Therefore, for OTS the Berthelot hypothesis is reasonably well fulfilled at a contact angle of 0° and the value of γ_l calculated here is approximately equal to γ_s of the surface.

Finally, there is the evaluation of the coating with cTHFDP. Here a complex number is obtained. When looking at the approximation for γ_l^p in Figure 59 it can be seen that as soon as the overall surface tension becomes lower than 18.81 mJ/m², γ_l^p becomes negative. In Equation 54 then a root is formed containing γ_l^p to solve for γ_l . With this approximation, this results in γ_l being complex as long as γ_l is below 18.81 mJ/m². Neither negative nor complex numbers for the surface tension or the surface energy make any sense and therefore the approximation of γ_l^p cannot be used for an extrapolation below 18.81 mJ/m². The calculated value for γ_l of a theoretical probe liquid showing a contact angle of 0° on cTHFDP is therefore meaningless.

It has to be added that all presented methods to evaluate the surface energy are only applicable if the drops are in equilibrium. However, for some samples we observed quite a large range between the advancing and the receding contact angle and there is no way to distinguish which contact angle between those two is in fact in equilibrium. The contact angles we observed and used for the evaluations are relatively close to the advancing contact angles due to the procedure used for placing the drop on the sample for the measurement. To give upper and lower limits for the surface energies, all evaluations have been repeated with advancing and receding contact angle measurements, respectively. An overview of the surface energies obtained so far is summarized in Table 18, calculations done with advancing contact angles can be found in Table 19 and calculations done with receding in Table 20. All underlying graphs for the evaluation were created analogously and can be found in Figure 61.

Coating	Surface energy (mJ/m ²)	Owens-Wendt approach	Zisman plot: Berthelot	Zisman plot: cubic polynomial	Linear fit: OWKR-Young	Zisman plot: OWKR-Young
cTHFDP	γ_s	12.041 ± 0.004	7.31 ^I	12.89 ^{II, III}	12.79	15.43 ± 0.28 ^I
	γ_s^d	11.938 ± 0.002			12.76	
	γ_s^p	0.103 ± 0.003			0.02	
OTS	γ_s	20.24 ± 0.02	11.41 ^I	19.28 ^{II}	22.51	20.47
	γ_s^d	20.20 ± 0.02			22.51	
	γ_s^p	0.040 ± 0.004			0.00 ^{IV}	
11-N ₃	γ_s	22.33 ± 0.05	19.91 ^I	23.93 ^{II, III}	23.63	23.47 ^{III}
	γ_s^d	16.83 ± 0.05			20.57	
	γ_s^p	5.493 ± 0.009			3.05	

Table 18: Summary of the calculated surface energies of different coatings. ^I: Highly unreliable due to unfulfilled theoretical requirements; ^{II}: Inaccurate due to extrapolation without theoretical background; ^{III}: Underestimates the surface energy due to unfulfilled requirements for the Berthelot hypothesis at $\theta = 0^\circ$; ^{IV}: No precise evaluation possible due to negative abscissa.

Coating	Surface energy (mJ/m ²)	Owens-Wendt approach	Zisman plot: Berthelot	Zisman plot: cubic polynomial	Linear fit: OWKR-Young	Zisman plot: OWKR-Young
cTHFDP	γ_s	11.83 ± 0.05	6.08 ^I	13.41 ^{II, III}	13.08	no solution
	γ_s^d	11.78 ± 0.05			13.08	
	γ_s^p	0.052 ± 0.013			0.00 ^{IV}	
OTS	γ_s	19.188 ± 0.010	10.78 ^I	19.12 ^{II}	21.36	19.94
	γ_s^d	19.139 ± 0.008			21.36	
	γ_s^p	0.050 ± 0.007			0.00 ^{IV}	
11-N ₃	γ_s	20.842 ± 0.014	14.56 ^I	21.52 ^{II, III}	15.10 ^V	14.13 ± 8.72 ^{I, V}
	γ_s^d	15.217 ± 0.014			4.35 ^V	
	γ_s^p	5.625 ± 0.002			10.75 ^V	

Table 19: Summary of the calculated surface energies of different coatings using advancing contact angles. ^I: Highly unreliable due to unfulfilled theoretical requirements; ^{II}: Inaccurate due to extrapolation without theoretical background; ^{III}: Underestimates the surface energy due to unfulfilled requirements for the Berthelot hypothesis at $\theta = 0^\circ$; ^{IV}: No precise evaluation possible due to negative abscissa; ^V: Unreliable results due to bad fit of the regression curve with the data.

Coating	Surface energy (mJ/m^2)	Owens-Wendt approach	Zisman plot: Berthelot	Zisman plot: cubic polynomial	Linear fit: OWKR-Young	Zisman plot: OWKR-Young
cTHFDP	γ_s	15.03 ± 0.04	12.83^I	$12.47^{II, III}$	15.58	16.93 ± 1.99^I
	γ_s^d	12.50 ± 0.04			13.84	
	γ_s^p	2.538 ± 0.009			1.74	
OTS	γ_s	18.954 ± 0.009	13.93^I	18.23^{II}	20.38	20.19
	γ_s^d	17.970 ± 0.007			19.86	
	γ_s^p	0.984 ± 0.006			0.52	
11-N ₃	γ_s	25.91 ± 0.02	26.85^I	$30.50^{II, III}$	31.06	30.34^{III}
	γ_s^d	13.069 ± 0.019			24.18	
	γ_s^p	12.841 ± 0.003			6.87	

Table 20: Summary of the calculated surface energies of different coatings using receding contact angles. ^I: Highly unreliable due to unfulfilled theoretical requirements; ^{II}: Inaccurate due to extrapolation without theoretical background; ^{III}: Underestimates the surface energy due to unfulfilled requirements for the Berthelot hypothesis at $\theta = 0^\circ$; ^{IV}: No precise evaluation possible due to negative abscissa.

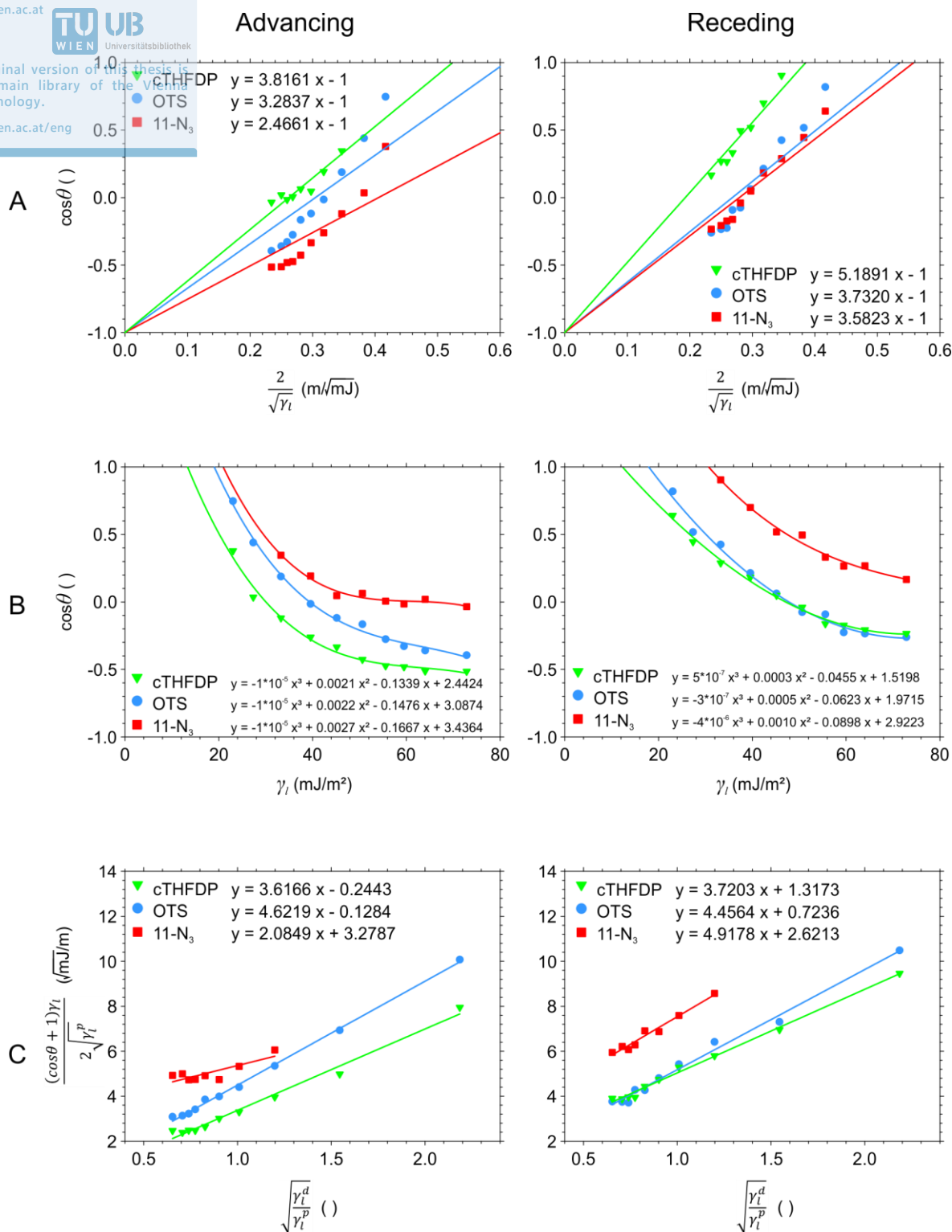


Figure 61: Overview over all plots used to determine surface energies from advancing and receding contact angles. A: Data fitted according to Equation 15, assuming a valid Berthelot hypothesis over the whole range. Subsequent extrapolation to $\cos\theta = 0^\circ$ gives γ_s ; B: Data fitted with a cubic polynomial. Subsequent extrapolation to $\cos\theta = 0^\circ$ gives γ_s ; C: Data fitted according to Equation 53 using the assumption presented in Figure 59. Slope and abscissa used for determination of γ_s^d and γ_s^p . Extrapolation to $\cos\theta = 0^\circ$ gives γ_s .

4.1.3.4 Evaluation of Surface Properties

The approved original version of this thesis is
available at the main library of the Vienna
University of Technology.

<http://www.ub.tuwien.ac.at/eng>

Finally, we wanted to use the contact angle data to gather information about r and ϕ . When looking at the equations describing the Wenzel (Equation 16) and the Cassie-Baxter state (Equation 17) in 2.1.3, it can be seen that there is a linear relation between the cosine of the contact angle on flat surfaces and on rough surfaces. The slope of these linear curves represents r for the Wenzel state and ϕ for the Cassie-Baxter state. Therefore, we plotted our data accordingly to be able to obtain these parameters (Figure 62).

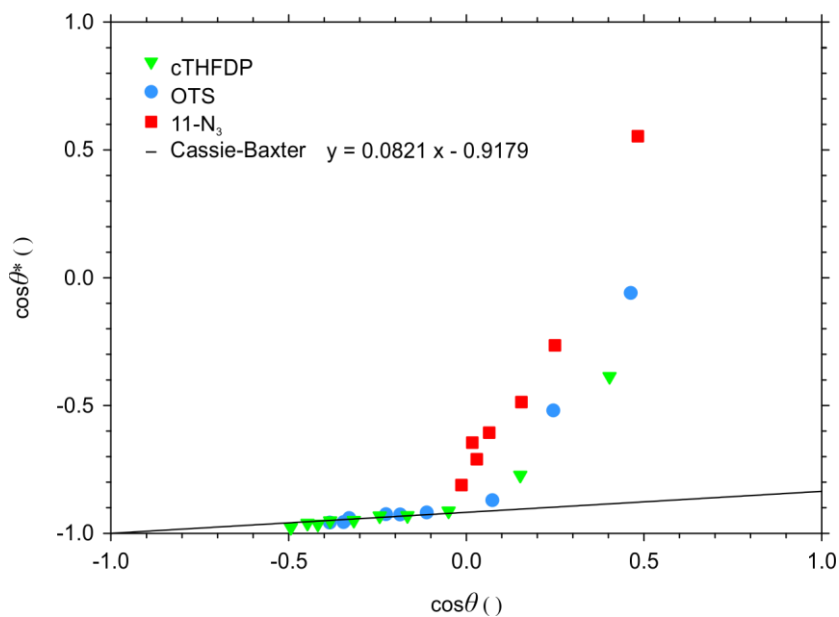


Figure 62: Plot of cosine of contact angle measurements on flat substrates ($\cos\theta$) against cosine of contact angle measurements on rough substrate ($\cos\theta^*$) to determine ϕ and r according to Equation 16 and 17.

The data representing the Cassie-Baxter region are in good agreement with the presented theory in 2.1.3. First of all, we expect all coatings to fit to the same curve since this plot should only be dependent on the topography of the surface, which is the same for all samples, and should be independent of the coating. Also, as expected, the Cassie-Baxter region is only observable for $\cos\theta < 0$. From Equation 17 we can therefore conclude that ϕ is 0.08, which is the slope of the fitted curve.

In 4.1.1.1 ϕ was already determined with a different method. SEM measurements and a subsequent graphical evaluation was used there, ultimately resulting in a ϕ of 0.30 for these etching conditions. The numbers are quite different but both methods have some limitations. As pointed out in 4.1.1.1, the evaluation using the SEM pictures strongly depends on the chosen threshold for the grey scale to distinguish between substrate and pores resulting in a large error. The evaluation presented in this chapter requires the Cassie-Baxter equation to be applicable. The Cassie-Baxter

equation, however, can only describe drops in equilibrium. As already discussed in the previous chapter, we cannot precisely determine the contact angle in equilibrium. Neither method is therefore suitable to reliably determine absolute values of ϕ and both obtained values can only be understood as approximations from two different approaches.

When comparing the Wenzel region in Figure 62 with the theory presented in 2.1.3 there are also some problems. First of all, all different coatings should behave the same but there appears to be a significant difference between them. Secondly, the Wenzel equation requires the curve to pass through the origin. Again, the measured points do not follow this behaviour. The problems probably occur because the data do not represent the equilibrium state and the Wenzel equation is only capable to describe the equilibrium. We were not able to refine the theory in a way to explain the observed behaviour. Nevertheless, we already determined r in 4.1.1.1 from integrals of FTIR measurements. In contrast to the other methods described to determine ϕ , the evaluation of FTIR spectra is a reliable way to obtain good results for r . While it would be desirable to have another method at hand to compare with the value of r obtained from FTIR measurements, it is not needed to fully characterize the samples.

4.2 SLIPS Systems

4.2.1 Probe Liquid – General Considerations

SLIPS systems are more complex than Cassie-Baxter systems since two different liquids are involved, which have to arrange in certain way on a rough substrate. If they mix or complete wetting of the impregnation liquid on the surface is lost, the desired SLIPS collapses. So, before any thoughts about the underlying chemical composition can be made, it has to be decided for which probe liquids a SLIPS system should be designed.

When comparing different liquids, it catches the eye that most liquids with high surface tension show a considerable polar component of their surface tension, while liquids with low surface tension mainly show dispersive properties (Table 2). It is also to mention that it is particularly easy to design a surface which repels liquids with high surface tension with flat or Cassie-Baxter systems. Possibly the most rewarding approach is therefore to target liquids with low surface tension with just dispersive properties.

4.2.2 Impregnation Liquid

The impregnation liquid has to be chosen in accordance with the probe liquid. From 2.1.5 it is known that the following conditions have to be fulfilled to avoid complete wetting of the probe liquid on the impregnation liquid (Inequation 55) as well as cloaking (Inequation 56).

$$\frac{\gamma_i - \gamma_{il}}{\gamma_l} < 1 \quad (55)$$

$$\frac{\gamma_l - \gamma_{il}}{\gamma_i} < 1 \quad (56)$$

In these inequations, γ_{il} can be replaced using the OWKR approximation (Equation 9) and secondly, since the targeted probe liquids will not have any significant polar component, $\gamma_i^p = 0$ and $\gamma_l = \gamma_l^d$ can be applied. This leaves us with the following updated conditions to avoid the undesired states.

$$\gamma_i^d < \gamma_l^d \quad (57)$$

$$\frac{\sqrt{\gamma_l^d \gamma_i^d}}{\gamma_i^d + \gamma_i^p} < 1 \quad (58)$$

It can be seen that complete wetting can be avoided if the dispersive component of the impregnation liquid is low (Inequation 57). Further a high polar component of the impregnation liquid is beneficial to avoid cloaking (Inequation 58).

Besides wetting properties, the impregnation liquid should also show low volatility since, when the impregnation liquid evaporates, the SLIPS state will inevitably collapse. Thus, we decided to use ionic liquids. They show only negligible evaporation, resulting in the most durable SLIPS systems and they are promising candidates to fulfil the requirements both, regarding their surface tension and immiscibility with the probe liquid, because of their widely tuneable properties.

4.2.2.1 Surface Tension Measurement of Selected Ionic Liquids

With the desired properties of the impregnation liquid known, we then wanted to search for an ionic liquid with suitable properties for SLIPS systems, namely a low dispersive component (γ_i^d) and a high polar component (γ_i^p). We were provided with several ionic liquids by Katharina Schröder to investigate their properties. The structure of all ionic liquids tested here are shown in Table 21.

Abbreviation

Structure

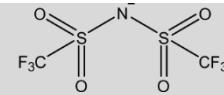
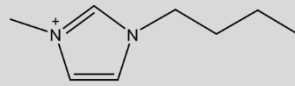
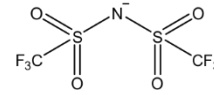
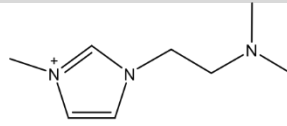
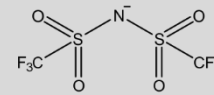
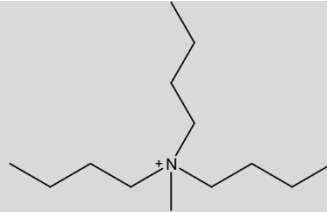
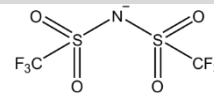
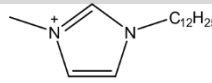
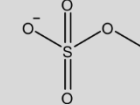
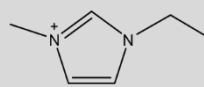
[bmim][NTf₂][MeNCmim][NTf₂][N4441][NTf₂][C₁₂mim][NTf₂][C₂mim][MeSO₄]

Table 21: Structure of selected ionic liquids investigated regarding their suitability as impregnation liquid for SLIPS systems.

With these liquids at hand, we could then proceed to characterize them regarding their suitability for SLIPS systems. The most important parameters to determine are the dispersive and polar component of the surface tension. In 2.1.2 and 4.1.3.3 we already discussed and carried out the determination of the polar and dispersive components for solids. There we used well-characterized liquids and brought them in contact with unknown solid surfaces. From the contact angle of the liquids on the surfaces, we could then derive the properties of the surface. These methods are also applicable the other way around, when the liquid is unknown and the solid is well-characterized.

Out of the different approaches discussed in 4.1.3.3, we chose to use an adapted Owens-Wendt approach. The evaluation is thereby based on a combination of the Young equation and the OWKR approximation (Equation 10). For each measurement, if the properties of the surfaces are known, an equation can be formed with only two unknown variables, γ_i^p and γ_i^d . If each liquid is measured on two different surfaces, the two resulting equations can then be solved for γ_i^p and γ_i^d (Equation 59 and 60).

$$\gamma_i^p = \left(\frac{2 \left(\sqrt{\gamma_{s,1}^d \gamma_{s,2}^p} - \sqrt{\gamma_{s,2}^d \gamma_{s,1}^p} \right) \left(\sqrt{\gamma_{s,1}^d} (\cos \theta_2 + 1) - \sqrt{\gamma_{s,2}^d} (\cos \theta_1 + 1) \right)}{\left(\sqrt{\gamma_{s,1}^d} (\cos \theta_2 + 1) - \sqrt{\gamma_{s,2}^d} (\cos \theta_1 + 1) \right)^2 + \left(\sqrt{\gamma_{s,1}^p} (\cos \theta_2 + 1) - \sqrt{\gamma_{s,2}^p} (\cos \theta_1 + 1) \right)^2} \right)^2 \quad (59)$$

$$\left(\frac{2 \left(\sqrt{\gamma_{s,1}^d \gamma_{s,2}^p} - \sqrt{\gamma_{s,2}^d \gamma_{s,1}^p} \right) \left(\sqrt{\gamma_{s,1}^p (\cos \theta_2 + 1)} - \sqrt{\gamma_{s,2}^p (\cos \theta_1 + 1)} \right)}{\left(\sqrt{\gamma_{s,1}^d (\cos \theta_2 + 1)} - \sqrt{\gamma_{s,2}^d (\cos \theta_1 + 1)} \right)^2 + \left(\sqrt{\gamma_{s,1}^p (\cos \theta_2 + 1)} - \sqrt{\gamma_{s,2}^p (\cos \theta_1 + 1)} \right)^2} \right)^2 \quad (60)$$

Therefore, we could put the surfaces we investigated in 4.1.3.3 to good use and utilized them for the characterization of the ionic liquids. We decided to use 11-N₃ and cTHFDP coated flat substrates since their properties differ the most out of the three surfaces, which is beneficial for the accuracy of this method. For the surface energy of the two surfaces we have different values calculated based on different models available but, to stay consistently to the same model for all calculations, we decided to use the values obtained from the Owens-Wendt approach (11-N₃: $\gamma_l^p = 5.493 \pm 0.009$ mJ/m² and $\gamma_l^d = 16.83 \pm 0.05$ mJ/m²; cTHFDP: $\gamma_l^p = 0,103 \pm 0.003$ mJ/m² and $\gamma_l^d = 11.938 \pm 0.002$ mJ/m²). All measured contact angles and the calculated values for γ_i^p and γ_i^d according to Equation 59 and 60 are listed in Table 22.

Probe liquid		11-N ₃ (°)	cTHFDP (°)	γ_i (mJ/m ²)	γ_i^p (mJ/m ²)	γ_i^d (mJ/m ²)
[bmim][NTf ₂]	θ	22.5	87.3	20.69	12.82	7.87
	$\theta_{rec.}$	7.8	72.0			
	$\theta_{adv.}$	45.7	87.1			
[MeNCmim][NTf ₂]	θ	19.0	81.8	22.04	10.88	11.16
	$\theta_{rec.}$	0.0	70.3			
	$\theta_{adv.}$	37.0	71.0			
[N4441][NTf ₂]	θ	23.0	79.9	23.40	9.78	13.61
	$\theta_{rec.}$	4.3	63.5			
	$\theta_{adv.}$	45.6	80.0			
[C ₁₂ mim][NTf ₂]	θ	11.6	83.5	20.30	11.58	8.72
	$\theta_{rec.}$	0.0	69.4			
	$\theta_{adv.}$	29.7	86.8			
[C ₂ mim][MeSO ₄]	θ	57.4	104.1	28.14	21.08	7.06
	$\theta_{rec.}$	50.0	84.7			
	$\theta_{adv.}$	66.4	105.2			

Table 22: Measured contact angles on 11-N₃ and cTHFDP coated surfaces and calculated polar and dispersive component of the surface tension for selected ionic liquids.

Out of these five ionic liquids, [C₂mim][MeSO₄] shows the most promising results since it has the highest polar component and simultaneously the lowest dispersive component. Therefore, we continued all further investigations of SLIPS systems with this ionic liquid as impregnation liquid.

The requirements on the coating are very different than for Cassie-Baxter systems. The coating has to be adjusted to fit perfectly to the impregnation liquid. It is shown in 2.1.5 that for a functioning SLIPS, the impregnation liquid has to completely wet the surface regardless of the surrounding phase. To wet the surface under air, the Young equation can be directly applied (Equation 61). For the complete wetting of impregnation liquid with probe liquid as surrounding, a slightly adapted Young equation has to be used (Equation 62).

$$\frac{\gamma_s - \gamma_{si}}{\gamma_i} \geq 1 \quad (61)$$

$$\frac{\gamma_{sl} - \gamma_{si}}{\gamma_{il}} \geq 1 \quad (62)$$

For a deeper insight into the requirements regarding the coating, the OWKR approximation (Equation 9), as well as the fact that the probe liquid has no polar component ($\gamma_i^p = 0$ and $\gamma_l = \gamma_i^d$) can be applied to Inequation 61 and 62 leading to Equation 63 and 64.

$$\frac{\sqrt{\gamma_s^d \gamma_i^d} \sqrt{\gamma_s^p \gamma_i^p}}{\gamma_i^d + \gamma_i^p} \geq 1 \quad (63)$$

$$\frac{\gamma_i^d - \gamma_i - 2\sqrt{\gamma_s^d \gamma_i^d} + 2\sqrt{\gamma_s^d \gamma_i^d} + 2\sqrt{\gamma_s^p \gamma_i^p}}{\gamma_i^d + \gamma_i - 2\sqrt{\gamma_i^d \gamma_i^d}} \geq 1 \quad (64)$$

While increasing dispersive properties of the surface energy is beneficial for wetting under air (Inequation 63), it is not for wetting with probe liquid as surrounding (Inequation 64), since $\sqrt{\gamma_s^d \gamma_i^d}$ has to be smaller than $\sqrt{\gamma_s^d \gamma_i^d}$ to still fulfil Inequation 57. Increasing polar properties of the surface energy, however, helps to fulfil both, Inequation 63 and 64. As long as the premise is met, that the probe liquid only shows dispersive properties, it is therefore desirable to use a coating with a polar component as high as possible.

This question can also be approached from a different perspective. When assuming that the properties of the coating and the impregnation liquid are perfectly identical, all indices of s and i are interchangeable ($\gamma_s = \gamma_i$, $\gamma_s^d = \gamma_i^d$ and $\gamma_s^p = \gamma_i^p$). With that assumption, also the interface tension between those two becomes 0 according to the OWKR approximation ($\gamma_{si} = 0$). When inserting this in Equation 61 and 62, it can be seen that the left side of both inequations equals 1

and therefore they are always met. This is even true for probe liquids which show polar properties of their surface tension and therefore adds versatility to the final SLIPS system.

The ideal coating therefore would be as similar to the impregnation liquid as possible and, if there is any deviation, it should be an increased polar contribution when targeting dispersive probe liquids. We decided that a coating similar to the selected ionic liquid had to be synthesised to meet these requirements. The most promising approach for this is probably to use a coating which features the same chemical functions as the impregnation liquid and is an ionic liquid itself. The counterions of the coating can then exchange with those of the impregnation liquid for a perfect match of their properties. Additionally, we also planned to use an uncoated SiO₂ surface and to compare the results.

4.2.3.1 Synthesis and Covalent Coating of [C₃mim]Cl

We chose [C₃mim]Cl (Figure 63) as coating for our SLIPS systems. The compound was provided by Matthias Mastalier who synthesised it according to a procedure presented in literature [65]. He used the approach presented in 3.1.2. The compound was characterized with FTIR between sodium chloride windows (Figure 64) and with ¹H-NMR in CDCl₃ (Figure 65).

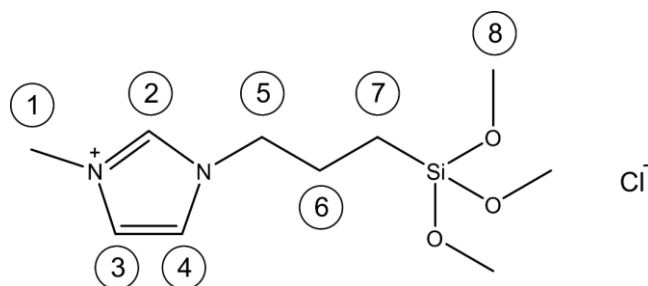


Figure 63: [C₃mim]Cl with labelled CH groups correlating with ¹H-NMR peaks found in Figure 65.

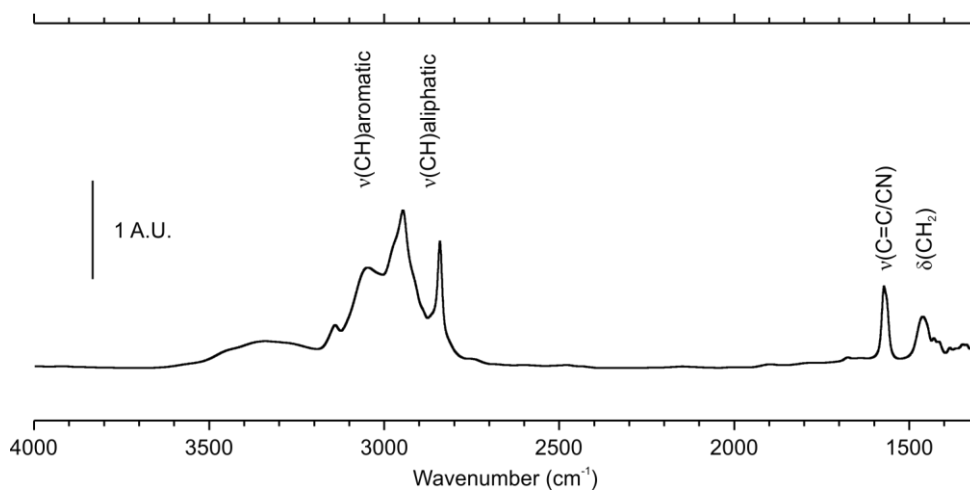


Figure 64: IR spectrum of [C₃mim]Cl between two sodium chloride windows.

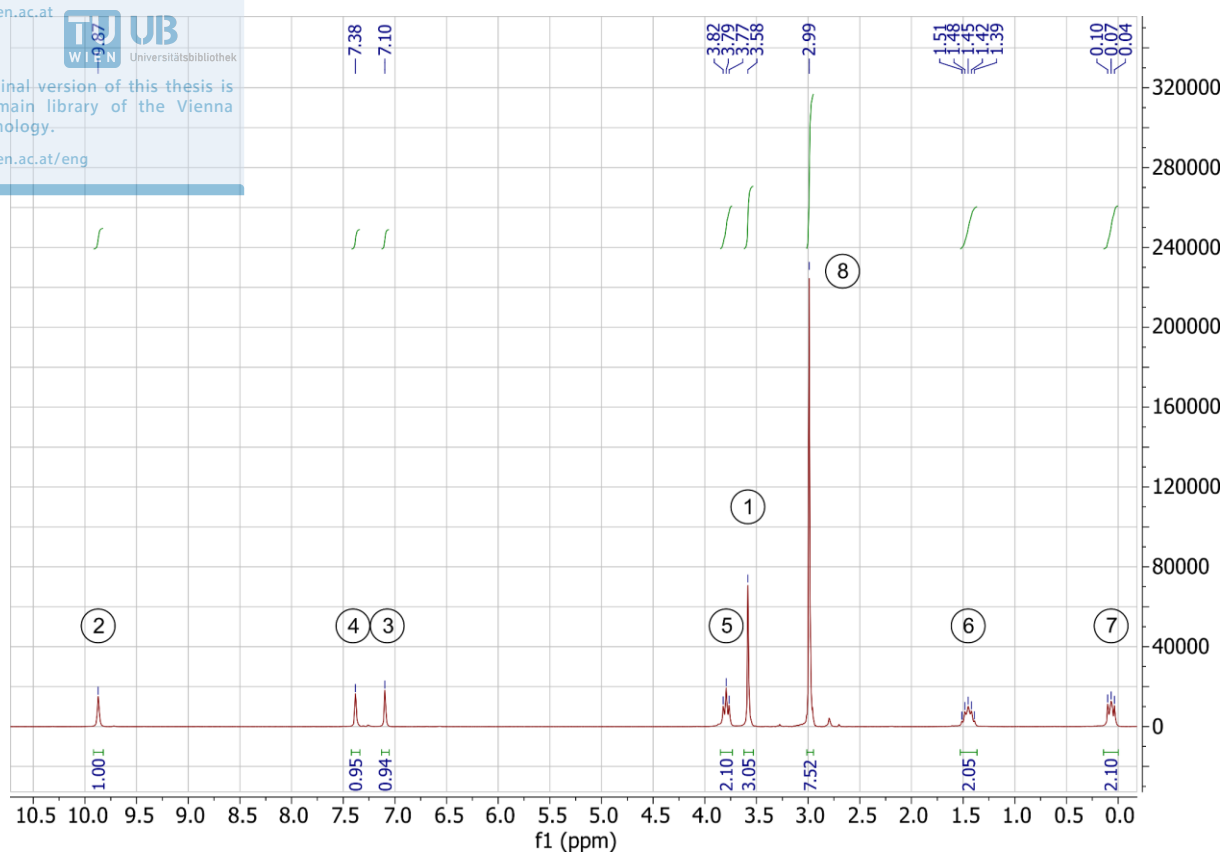


Figure 65: $^1\text{H-NMR}$ measurement of $[\text{C}_3\text{mim}]\text{Cl}$ in CDCl_3 .

$^1\text{H NMR}$ (250 MHz, CDCl_3): $\delta = 0.07$ (t, $J = 8.2$ Hz, 2H), 1.45 (5, $J = 7.6$ Hz, 2H), 2.99 (s, 9H), 3.58 (s, 3H), 3.79 (t, $J = 7.1$ Hz, 2H), 7.10 (s, 1H), 7.38 (s, 1H), 9.87 (s, 1H) ppm

The measurements showed all expected peaks and the compound could therefore be used for coating. Based on results of the coating with OTS and BUTS, for $[\text{C}_3\text{mim}]\text{Cl}$ a slightly different procedure was chosen to ensure a monolayer formation. Here we did not investigate the necessary time to reach a complete coating but instead we assumed that, as the previous two compounds showed, the coating does not form multilayers. This means while the reaction time can be too short, it cannot be too long. We chose to treat the samples 48 hours, which should be more than sufficient, and measured the layer thickness and FTIR spectra afterwards to check if the results are reasonable.

We performed ellipsometric measurements on flat samples resulting in a layer thickness of $4.7 \pm 0.3 \text{ \AA}$ which is in reasonably good agreement with the distance between the silicon atom and the outer most carbon atom of 8.8 \AA calculated from Chem3D, considering that the refractive index of the compound is unknown. For FTIR measurements a relative high number of 15 nanowire samples were prepared, since they were also needed for subsequent investigations of SLIPS systems. An average of the recorded 15 spectra is shown in Figure 66.

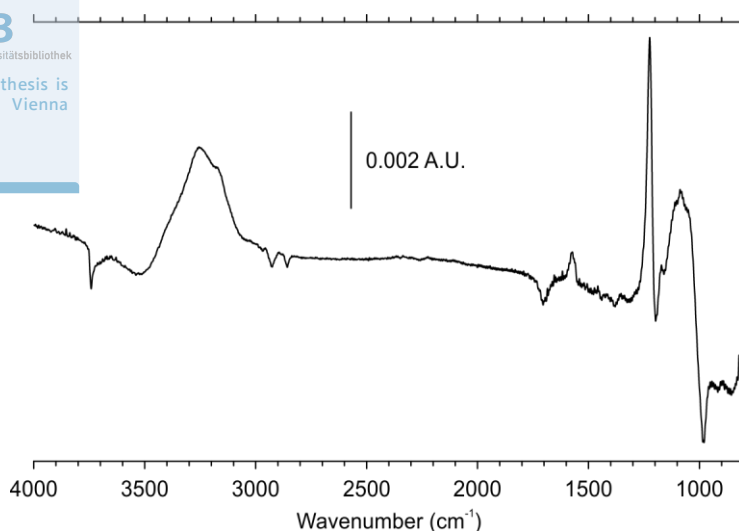


Figure 66: FTIR spectrum of [C₃mim]Cl on nanowire substrate, averaged over fifteen samples.

Interestingly, every single sample showed negative peaks in the CH region which was already observed when investigating samples etched with a H₂O₂ concentration of 0.24 M (Figure 33). Still no explanation for the behaviour could be found. Nevertheless, due to mere presence of peaks in the CH region, even though they are negative, and due to the peak at 1573 cm⁻¹, representing the C–C/C–N ring stretching vibration of the imidazolium ring, we concluded that the coating worked and continued with the samples to prepare SLIPS systems. Also, applying the coating to a flat surface and measuring FTIR spectra did not give any additional information since no peaks in the region of question were observed at all. However, this is mainly due to the low amount of analyte on flat surfaces. The FTIR spectrum of [C₃mim]Cl applied to a flat surface averaged over three different samples is shown in Figure 67.

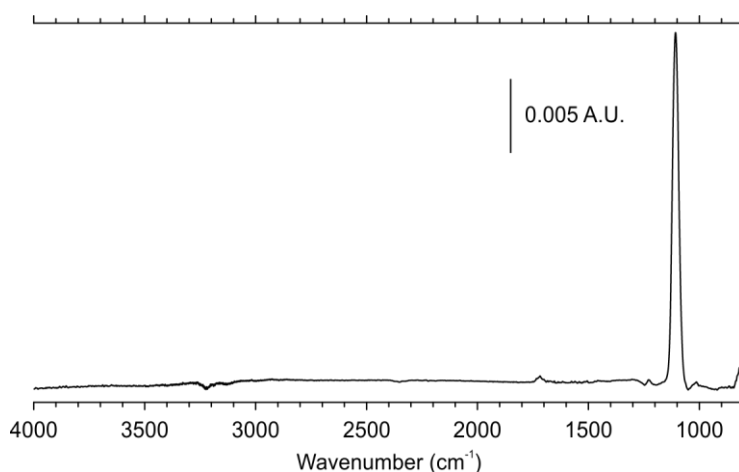


Figure 67: FTIR spectrum of [C₃mim]Cl on flat substrate, averaged over three samples.

Ultimately, contact angle measurements presented in 4.2.5 later supported our assumption regarding the presence of [C₃mim]Cl on the surface, since the behaviour of ionic liquid on the surface can very well be explained with the presence of the coating.

4.2.4 Probe Liquid - Miscibility with [C₂mim][MeSO₄]

In the next step, we were interested which liquids potentially can be repelled by a SLIPS system based on [C₂mim][MeSO₄] as impregnation liquid and [C₃mim]Cl as coating. We chose a set of very common organic solvents, preferably with different chemical functions, to have compounds representing a group of similar solvents. We used dimethylformamide (DMF), dimethyl sulfoxide (DMSO), acetonitrile, ethylene glycol, ethanol, water, diethyl ether, tetrahydrofuran (THF), cyclohexane, hexadecane, toluene and ethyl acetate.

However, not all listed solvents are suitable for this application. Probably the most important criterion to exclude probe liquids from further experiments is miscibility. If a probe liquid is completely miscible with the impregnation liquid, a SLIPS state cannot form when a drop of probe liquid comes in contact with the final surface. Instead the impregnation liquid in the pores will be diluted and washed out, destroying the arrangement in the process.

Partial miscibility, on the other hand, is less of a problem, if handled correctly. If there is some solubility of impregnation liquid in the probe liquid, it still may wash the impregnation liquid out of the pores but only until the probe liquid is saturated. Thus, by only using probe liquids pre-saturated with impregnation liquid, loss of impregnation liquid can be avoided. Even though it is manageable, high solubility is still disadvantageous. It increased the consumption of the expensive ionic liquid necessary to saturate the probe liquid. If there is some solubility the other way around, it is also manageable. In general, solubility of probe liquid in the impregnation liquid will change the properties of the impregnation liquid during the experiment, leading to poorly reproducible results if unchecked. This can again be completely avoided if the used impregnation liquid was already saturated before the experiment takes place. But also in this case too much solubility is harmful since then the properties of the carefully selected impregnation liquid are significantly altered when mixing with another liquid, probably giving worse results. It is therefore advisable to use liquids which are as little miscible as possible. As a consequence, we decided whenever two liquids get into contact during an experiment, to make sure first that both are saturated with each other to avoid further problems.

Then we proceeded to investigate the listed solvents regarding their suitability by checking if they show a miscibility gap with [C₂mim][MeSO₄]. We mixed and stirred 500 µl of [C₂mim][MeSO₄] with

500 μl of the probe liquid in question at room temperature. If after 4 hours only one phase remained, we excluded the probe liquid from further experiments. We only investigated the miscibility at room temperature since all further experiments were planned to be conducted at room temperature. Also, we only investigated a single mixing ratio so that we falsely may have excluded some solvents which show only a small miscibility gap. However, as pointed out, if there is only a small miscibility gap, the probe liquid is not ideal anyway. Therefore, falsely eliminating those was not considered an issue. The results of the preliminary miscibility tests can be found in Table 23.

Solvent	Number of phases after mixing with $[\text{C}_2\text{mim}][\text{MeSO}_4]$ 1:1 vol.
DMF	1
DMSO	1
acetonitrile	1
ethylene glycol	1
ethanol	1
water	1
diethyl ether	1
THF	2
cyclohexane	2
hexadecane	2
toluene	2
ethyl acetate	2

Table 23: Investigation of the solubility of different organic solvents with $[\text{C}_2\text{mim}][\text{MeSO}_4]$ by mixing 500 μl solvent with 500 μl ionic liquid, stirring and checking after 4 hours the number of formed phases.

This leaves us with THF, cyclohexane, hexadecane, toluene and ethyl acetate as possible probe liquids for further investigations.

4.2.5 Suitability Tests of Selected SLIPS Systems

Finally, we could then proceed to bring all three phases together and investigate the combination regarding their feasibility for SLIPS systems. As pointed out in 2.1.5, there is a total of four requirements which have to be met for a SLIPS system to be stable.

For the first two requirements, the impregnation liquid has to show a contact angle of 0° with air (Equation 61) and with probe liquid (Equation 62) as surrounding. Conveniently, both can directly be measured without further data analysis. It is thereby sufficient if only the receding contact angle is 0° to maintain the SLIPS state. On the other hand, an advancing contact angle of 0° leads to spontaneous formation of the SLIPS state. Therefore, a receding angle of 0° is required for all surroundings being used and at least under one surrounding the impregnation liquid also has to

show an advancing angle of 0° allowing the preparation of the SLIPS system. The results of the contact angle measurements can be found in Table 24.

Surrounding phase		SiO ₂ (°)	[C ₃ mim]Cl (°)
Air	θ	0	0
	$\theta_{rec.}$	0	0
	$\theta_{adv.}$	0	0
Toluene	θ	19.2 ± 1.3	9.7 ± 0.4
	$\theta_{rec.}$	0	0
	$\theta_{adv.}$	25.5 ± 0.4	24 ± 3
Hexadecane	θ	17 ± 6	22 ± 3
	$\theta_{rec.}$	0	0
	$\theta_{adv.}$	28 ± 3	32 ± 6
Ethyl acetate	θ	14.3 ± 1.4	0
	$\theta_{rec.}$	0	0
	$\theta_{adv.}$	16.9 ± 1.3	0
THF	θ	14 ± 4	0
	$\theta_{rec.}$	0	0
	$\theta_{adv.}$	28 ± 3	0
Cyclohexane	θ	29.5 ± 1.3	16 ± 3
	$\theta_{rec.}$	0	0
	$\theta_{adv.}$	41 ± 6	29 ± 2

Table 24: Contact angle data for [C₂mim][MeSO₄] on SiO₂ and [C₃mim]Cl coated flat substrates with different surrounding phases. For the measurements of [C₂mim][MeSO₄] surrounded by another liquid, both liquids were saturated with each other before the measurement took place.

In the table can be seen that the advancing contact angle under air is 0° for both surfaces, which allows the formation of the SLIPS state independent of the probe liquid used afterwards. All other receding contact angles measured are 0° and should therefore inhibit the spontaneous breakdown of the SLIPS state. From this point of view all combinations are therefore viable to give SLIPS.

Although the results look promising, THF notably showed a different behaviour than all other solvents. When saturating THF with [C₂mim][MeSO₄], the obtained solution was slightly cloudy (Figure 68). This indicates that an emulsion is formed with small drops of ionic liquid with diverting refractive index within the toluene phase leading to light scattering and thus the cloudiness. Due to difficulties separating the phases, all experiments for THF were in fact performed with the emulsion and therefore must be viewed critical. In general, using probe liquids which show a tendency to form emulsions with the impregnation liquid is problematic. Whenever there is kinetic energy input, like shaking, while a drop is on the SLIPS surface, parts of the impregnation liquid may leave the pores on the surface and form an emulsion within the small drop of probe liquid, leading to loss of impregnation liquid when the drop later leaves the surface. From that perspective, it can be

concluded that THF most certainly is not an ideal probe liquid for this SLIPS system and thus inaccuracies due to incomplete phase separation is less of a concern.

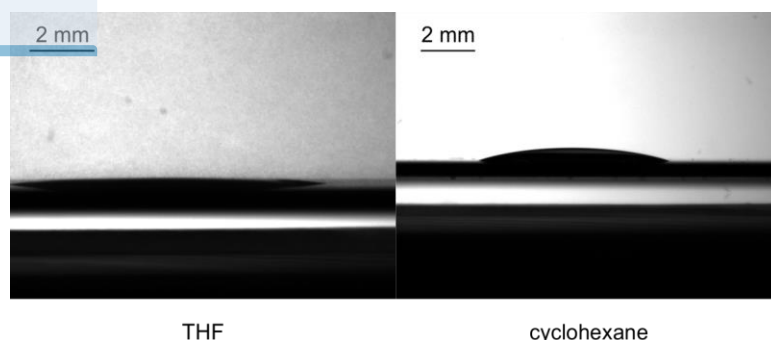


Figure 68: Comparison of a measurement showing a THF emulsion as surrounding with a measurement showing cyclohexane as surrounding. All other probe liquids investigated here showed similar behaviour as cyclohexane in this regard. In both pictures the contrast was increased identically to highlight the light scattering effects due to the emulsion found in THF.

Furthermore, the contact angle measurements confirm the claim from chapter 4.2.3.1 regarding the presence of $[C_3mim]Cl$ on the surface, which could not be confirmed without a doubt in that chapter. Based on the contact angle measurements here, there had to be a coating present on the surface treated with $[C_3mim]Cl$ since there were significant differences in the observed contact angles between the treated and the untreated set of samples. Overall, the observed contact angles on the treated samples were lower which correlates with the reason why this compound was chosen in the first place. The only reasonable conclusion could therefore be that the coating with $[C_3mim]Cl$ was indeed successful and contributed significantly to the formation of a stable SLIPS system.

This leaves then only the other two requirements to discuss, which only affect the interaction of the probe liquid with the impregnation liquid. The probe liquid should not completely wet the impregnation liquid (Equation 55) and there should be no cloaking occurring (Equation 56). These conditions cannot be directly measured but they are still easily and accurately accessible since every parameter in the equations can be determined with pendent drop measurements. This is also true for the interface tension between two liquids because then a pendent drop measurement with one of the two liquids as surrounding can be done.

To do pendent drop measurement, first the density of all liquids had to be determined. We remeasured the density of all probe liquids, even though precise measurements are known from literature, because in this work we did not use pure solvents but saturated them with the ionic liquid before the experiments, altering their density. On the other hand, we refrained from doing the same for the ionic liquid, even though it is also saturated with probe liquids, since this would

require a significant amount of expensive ionic liquid. Judging from the results obtained from the remeasured densities of the saturated probe liquids (Table 25) and from the underlying equation used in the instrument software to evaluate surface and interface tensions (Equation 52), the reduced accuracy due to the deviating density of the ionic liquid is expected to be negligible and well within the overall error of the method. Thus, we used the density of pure $[\text{C}_2\text{mim}][\text{MeSO}_4]$ for all evaluations of surface and interface tensions despite the fact that for the measurements itself $[\text{C}_2\text{mim}][\text{MeSO}_4]$ saturated with the respective probe liquid was used. Then, we proceeded to measure all surface and interface tensions according to the procedure presented in 3.3.3. The results of all these measurements are listed in Table 25.

Probe liquid	ρ { }	ρ { $[\text{C}_2\text{mim}][\text{MeSO}_4]$ }	γ_l { $[\text{C}_2\text{mim}][\text{MeSO}_4]$ }	γ_i {probe liquid}	γ_{il} {probe liquid; $[\text{C}_2\text{mim}][\text{MeSO}_4]$ }
	(g/cm ³)	(g/cm ³)	(mJ/m ²)	(mJ/m ²)	(mJ/m ²)
Toluene	0.87 [69]	0.871	25.03 ± 0.04	56.6 ± 0.3	12.1 ± 0.2
Hexadecane	0.77 [69]	0.761	22.9 ± 0.3	51.1 ± 0.5	20.5 ± 0.3
Ethyl acetate	0.90 [69]	0.894	18.3 ± 0.2	51.8 ± 0.3	6.15 ± 0.05
THF	0.89 [69]	0.881	23.25 ± 0.18	55.8 ± 0.5	7.38 ± 0.13
Cyclohexane	0.78 [69]	0.802	25.29 ± 0.04	53.4 ± 0.6	18.2 ± 0.4
$[\text{C}_2\text{mim}][\text{MeSO}_4]$	1.295			55.2 ± 0.5	

Table 25: Overview over density measurements in comparison with values from literature and surface and interface tension measurements using the measured density values for the evaluation. For the surface and interface tension measurements, i represents $[\text{C}_2\text{mim}][\text{MeSO}_4]$ whereas l represents the different probe liquids. The compound in curly brackets indicates the liquid used to saturate the investigated liquid before the measurement took place.

Using the values obtained here, we could then proceed with the evaluation to check if the combinations of liquids are prone to show cloaking or complete wetting of probe liquid on the impregnation liquid according to the conditions defined in Equations 55 and 56. The corresponding parameters are listed in Table 26. Values smaller than 1 indicate that the conditions are fulfilled and desired behaviour is expected.

Probe liquid	Cloaking $\frac{\gamma_i - \gamma_{il}}{\gamma_l}$ ()	Wetting behaviour $\frac{\gamma_i - \gamma_{il}}{\gamma_i}$ ()
Toluene	0.228 ± 0.004	1.777 ± 0.016
Hexadecane	0.047 ± 0.009	1.34 ± 0.03
Ethyl acetate	0.235 ± 0.005	2.49 ± 0.04
THF	0.284 ± 0.005	2.08 ± 0.03
Cyclohexane	0.133 ± 0.006	1.39 ± 0.03

Table 26: Calculated terms according to the conditions presented in Equation 55 and 56 for cloaking and complete wetting of probe liquid on the impregnation liquid. Values smaller than 1 are unproblematic for either behaviour.

While cloaking is not an issue for any investigated probe liquid, it is disappointing to see that the parameters in the last row of Table 26 predict complete wetting of all probe liquids on the impregnation liquid. This wetting behaviour, although undesirable, is the less impactful problem since at least the arrangement below the probe liquid is stable and impregnation liquid is not expected to be lost. Therefore, these systems may still serve some purpose when a stable liquid-liquid interface is of interest instead of the liquid repellent behaviour.

However, calculating these parameters for reported SLIPS systems in the literature, it can be seen that in fact several are predicted not to give stable SLIPS states even though it is shown in the publications that they do (Table 27). Thus, the theoretical parameters introduced in 2.1.5 are likely not sufficient to reliably predict the behaviour of SLIPS systems. As a consequence, we continued with the experimental evaluation of all probe liquids, even though they are predicted to show a contact angle of 0° on the SLIPS surfaces.

Substrate	Impregnation liquid	Probe liquid	θ_i {air} (°)	θ_i {probe liquid} (°)	Cloaking $\frac{\gamma_i - \gamma_{il}}{\gamma_l}$ ()	Wetting behaviour $\frac{\gamma_l - \gamma_{il}}{\gamma_i}$ ()	Ref.
Si - FDTS ^I	Krytox	Glycerol	42.3	0.0 ^{II}	-0.39	1.15	[43]
Si - FDTS ^I	Krytox	Heptane	42.3	37.8 ^{II}	0.63	0.91	[43]
Si - FDTS ^I	Krytox	Hexadecane	42.3	0.0 ^{II}	0.30	1.09	[43]
Si - FDTS ^I	Krytox	Water	42.3	27.2 ^{II}	-0.54	0.94	[43]
Si - OTS	Krytox	Water	28.0	28.0	-0.44	1.35	[70]
Si - OTS	Silicone	Water	0.0	0.0	-0.37	1.27	[44]
Si - OTS	Bmim ^{IV}	Water	60.8	12.5	0.50 ^{III}	0.85 ^{III}	[44]
Si - SiO ₂	Bmim ^{IV}	Water	9.8	133.1	0.50 ^{III}	0.85 ^{III}	[44]
Si - SiO ₂	Water	Hexane	13.1	0.0 ^{II}	1.16	-0.45	[71]

Table 27: Contact angle data and parameters describing cloaking and wetting behaviour either directly taken from literature or recalculated from published values to fit the representation style chosen here. Surrounding of the contact angle measurement indicated in curly brackets. A thermodynamically stable SLIPS system requires contact angles of 0° under both surroundings and values for cloaking and wetting smaller than 1. ^I: The used coating abbreviated as FDTS is heptadecafluoro - 1,1,2,2 - tetrahydrodecyltrichlorosilane; ^{II}: Values for θ_i {probe liquid} were calculated from published values of ΔE_1 , r and γ_{il} using the relation $\Delta E_1 = \gamma_{il} (r \cos\theta_i - 1)$; ^{III}: Surface and interface tensions for the calculation of the cloaking and wetting behaviour have been taken from [70]; ^{IV}: 1-Butyl-3-methylimidazolium bis(trifluoro-methyl-sulfonyl) imide

4.2.6 Topography

The topography of the underlying substrate also has to fulfil different needs for SLIPS. This time its only purpose is to keep the impregnation liquid in place. Since it is mandatory for the impregnation liquid to show a contact angle of 0°, an undisturbed surface will always stay wetted no matter the topography. However, the total energy difference between the desired thermodynamic stable state and any other state is proportional to the interface area between substrate and impregnation

liquid. This means external forces like gravity or other influences like mechanical damage disrupt the equilibrium for flat substrates more easily. To protect and further stabilize the SLIPS, the total energy difference can be increased by introducing roughness. While in general it is good to use a rough substrate for stability reasons, neither r nor ϕ of the substrate directly affect the final contact angle of the system. Extensive experiments inquiring those two parameters are therefore not fruitful for this application.

We decided to use the same substrates we prepared for Cassie-Baxter systems also for SLIPS systems because they already feature some roughness and no improvements regarding the contact angle from deviating topographies can be expected.

4.2.7 Contact Angle Measurements of SLIPS Systems

Finally, after thorough investigations of the applicability, we prepared several surfaces to investigate whether a stable SLIPS state forms. We prepared six silicon nanowire substrates for each probe liquid according to the procedure described in 4.1.1. Three of those were coated with $[\text{C}_3\text{mim}]\text{Cl}$ while the other three were used directly after the cleaning process with piranha solution and are therefore SiO_2 terminated. These samples were then impregnated with ionic liquid according to the procedure described in 3.2.4 and ultimately the contact angle of the respective probe liquid on the surface was measured (Table 28).

Probe liquid		[C ₃ mim]Cl (°)	SiO ₂ (°)
Toluene	θ	10.2 ± 0.4	9.6 ± 1.6
	Roll-off	5.0 ± 0.5	3.2 ± 0.7
	$\theta_{rec.}$	3.1 ± 1.8	2.7 ± 1.3
	$\theta_{adv.}$	13.9 ± 0.6	13.6 ± 0.4
Hexadecane	θ	0	
	Roll-off		
	$\theta_{rec.}$		
	$\theta_{adv.}$		
Ethyl acetate	θ	0	
	Roll-off		
	$\theta_{rec.}$		
	$\theta_{adv.}$		
THF	θ	0	
	Roll-off		
	$\theta_{rec.}$		
	$\theta_{adv.}$		
Cyclohexane	θ	8.5 ± 1.8	5.1 ± 1.4
	Roll-off	1.8 ± 1.2	1.2 ± 0.6
	$\theta_{rec.}$	5.7 ± 0.4	3.7 ± 1.1
	$\theta_{adv.}$	9 ± 2	5 ± 2

Table 28: Measured contact angles of SLIPS systems with different probe liquids and surface treatments.

Here we observed, as predicted, that hexadecane, ethyl acetate and THF in fact show a contact angle of 0° on the surface. The measurements with SiO₂ terminated surfaces were then skipped since the contact angle of the probe liquid is independent of the coating. After removal of the bulk of probe liquid by tilting and after a brief time for the remaining probe liquid to evaporate, the surface optically appeared unchanged, indicating that the other three requirements are indeed met, also as predicted. An optical examination of the sample has thereby been found to be useful to a certain extent. Dry parts are dull, while wet parts are reflective. Changes in composition of the outermost layer of the impregnation liquid are observable due to interferences, similar to a thin film of oil on water. And, finally, drops of displaced ionic liquid can also be easily spotted.

The measurements for toluene and cyclohexane, on the other hand, were successful (Figure 69, left and middle row). In both cases the observed contact angle was barely above the predicted 0°, yet large enough for functioning SLIPS. Here the surfaces also appeared unchanged after the removal of the probe liquid by tilting, indicating that the other three requirements are again met. The most compelling property of the surfaces is, though, the small roll-off angle of 1.8 ± 1.2° for cyclohexane and 5 ± 0.5° for toluene. It was even challenging for the measurement of cyclohexane to align the goniometer perfectly to avoid spontaneous movement of the drop when the sample stage was supposed to be horizontal.

It is also necessary to point out that the roll-off angle is dependent on the total weight and therefore the volume of the drop. Smaller drops are lighter and yield higher roll-off angles. For the measurements here, it was not possible to keep the drop size constant. The drops, which can be captured by the camera, are inevitable very small due to the small contact angle, simultaneously the automatic dosing unit of the device is not suited to dose such small volumes and even then, would the achievable precision be limited by evaporation. Instead we chose to use drops as big as possible to still fit on the picture to get more reliable values for the contact angles, which are independent of the drop size. The observed roll-off angles can therefore be only understood as a sign for exceptional liquid repellent behaviour and not as a precisely reproducible quantity. We did not list the roll-off angles for Cassie-Baxter systems because there we also did not put emphasis on keeping the drop volume constant either. Just to give a qualitative comparison, we measured the roll-off angle of pure water on a cTHFDP coated nanowire surface (Figure 69, right row). The samples showed a roll-off angle of $4.2 \pm 1.2^\circ$ which is higher than at least cyclohexane on the SLIPS surface even though the surface tension of water and the drop volume on this Cassie-Baxter surface is vastly higher, both favouring a smaller roll-off angle. Yet the speed with which the drop rolls off, once it started moving, is higher for Cassie-Baxter systems. Time-resolved images of drops of cyclohexane and toluene rolling off the SLIPS surfaces in comparison with a drop of water rolling off a cTHFDP terminated Cassie-Baxter surface are shown in Figure 69.

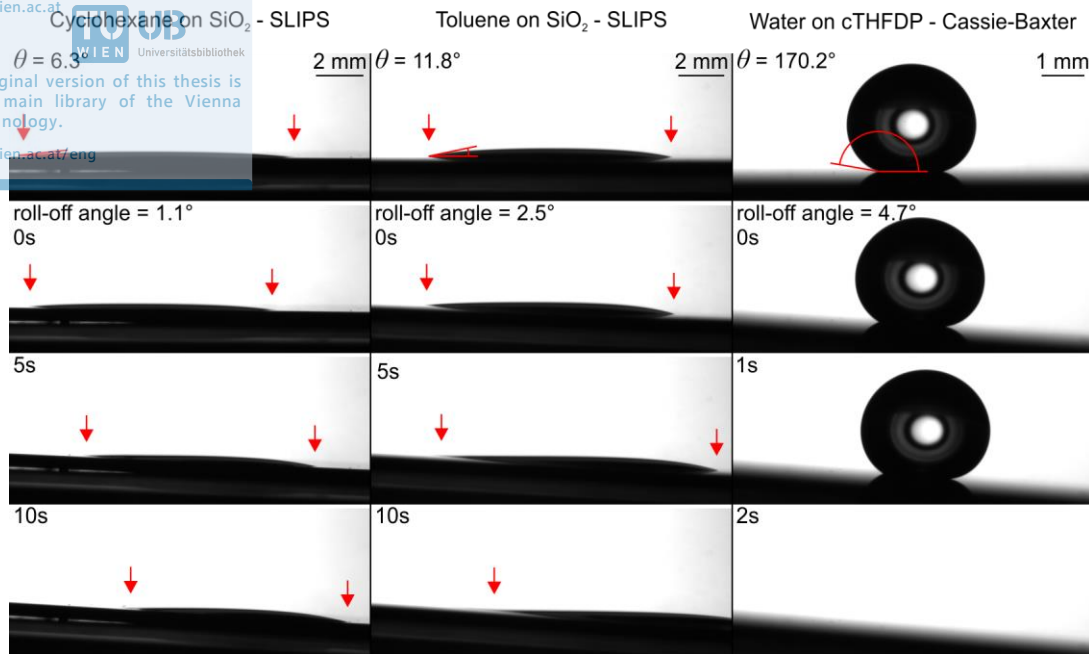


Figure 69: Cyclohexane (left row) and toluene (middle row) rolling-off a SiO₂-terminated SLIPS surfaces with [C₂mim][MeSO₄] as impregnation liquid in comparison with water rolling off a Cassie-Baxter surface (right row). In the first picture of each series the drop can be seen with horizontal sample stage and the measured contact angle. The second picture marks the point where the drops started moving and thus the roll-off angle was reached. The remaining pictures show the movement of the drop a few seconds after the drop started moving. For easier recognition of the drop in SLIPS, both ends of the drops in the picture were highlighted with red arrows. The denoted angles in the picture deviate slightly from the averaged values presented in Table 28 since they represent the measured value only for the single depicted measurement.

5 Conclusion

The approved original version of this thesis is
available at the main library of the Vienna
University of Technology.

<http://www.ub.tuwien.ac.at>

The topic of this thesis were two different concepts of liquid repellent surfaces, a 'dry' model based on the Cassie-Baxter wetting state and a 'wet' model based on a liquid infused surface (SLIPS). Several prototypes for each system were prepared and their properties, advantages and limitations were compared.

The first goal was the fabrication of versatile Cassie-Baxter substrates in a few simple and fast production steps without the requirement of sophisticated instrumentation. Starting with silicon wafers, rough nanostructured surfaces were prepared using silver-assisted etching. By employing FTIR, SEM and contact angle measurements, we were able to determine roughness und solid fraction of the resulting samples and finetune these parameters by varying etching duration and H₂O₂ concentration in order to control wettability and enhance FTIR signal-to-noise ratio. In order to improve the efficiency of the etching, we also determined the consumption of the chemicals of the etching solution which allowed us to replenish and reuse most solutions.

Overall, the surface structure prepared with this method cannot compete with hierarchically structured or overhanging, mushroom-like shapes regarding its liquid repellent properties. However, in return it is considerably easier to produce and also applicable to large areas without extra experimental setup.

In order to lower the surface energy of the blank silicon substrate, we used a two-step method. First, we applied a coating of a terminal azide on the surface and optimized this step to give only a monolayer. Then, we functionalized the monolayer with a polyfluorinated alkyl chain. All this could be observed with FTIR and ellipsometry measurements. We were then able to determine the surface energy of this coating with contact angle measurements.

The achieved surface energy ($\gamma_s = 12.79 \text{ mJ/m}^2$) lies on the lower end of typical polyfluorinated coatings, most notably, it outperforms PTFE ($\gamma_s = 21.36 \text{ mJ/m}^2$) [72]. One major advantage of this method is that it strictly forms monolayers on the silicon substrate. This will preserve the surface structure necessary for Cassie-Baxter systems. Furthermore, the method requires again only standard chemical laboratory equipment.

Our best Cassie-Baxter system gave a water contact angle of $168 \pm 3^\circ$. Results from experimentally similar approaches range here from 160° [73] to $173.5 \pm 2.9^\circ$ [74]. There are also reports of completely different but roughly similar extensive methods which show for example a contact angle

of greater than 150° [75] or again 160° [76]. Our water contact angles are apparently close to the top of comparable systems and most definitely in a range where small differences in contact angle no longer matter for concrete applications. This system also achieved a remarkable contact angle for ethanol of $113 \pm 2^\circ$. A proper comparison with other surfaces repelling liquids with low surface tension reported in literature cannot be done, since the surface tension of the probe liquids used in individual publications vary wildly and overshadow all surface properties.

Future investigations could focus on incorporation of controlled wettability to already existing silicon based components. When using different alkynes in the coating process, virtually any functionality can be added to a surface, enabling a broad range of applications. For example, a primary coating of azide, subsequently coupled to a molecule which shows strong but reversible interactions with an analyte and applied to the gate of a silicon based field-effect transistor, could result in a powerful sensor. Control of wettability by adding a monolayer with high or low surface energy on top of the sensor material in a second Huisgen cycloaddition as well as addition of roughness will most certainly be able to finetune the performance of the sensor.

A different approach considered during this work was to add anisotropy to the coating. This can be achieved by using alkyne covered gold nanoparticles and binding them to a rough azide coated surface. When using a solvent for this reaction which wets the surface according to the Cassie-Baxter state, the gold particles will only be able to bind to the tips of the nanowires. This leaves a rough surface which features alkyne groups at the tips and azide groups within the pores. Both groups can then be further functionalized independently. When using a polyfluorinated compound on the tips, a substrate can be prepared with certain functional groups only in contact with a liquid if the surface tension is below a threshold. This can be useful for example in analytics, catalysis or even medicine since the substrate can be activated in a controlled way by proper selection of the surrounding surface tension by addition of surfactants.

The second main focus in this work was the preparation of ionic liquid based SLIPS systems, repelling low surface tension liquids. For the most important task, the proper selection of the ionic liquid, we presented a set of criteria to assess their applicability as impregnation liquids and applied them on a small set of samples, favouring $[\text{C}_2\text{mim}][\text{MeSO}_4]$. We were then able to synthesise and attach a coating to a rough surface to match the properties of the selected ionic liquid, leading to a stable film of ionic liquid on the surface under all conditions tested here. This SLIPS substrate was then able to repel toluene and cyclohexane accordingly with extremely small roll-off angles, $5.0 \pm 0.5^\circ$ for toluene ($\gamma_l = 28.5 \text{ mJ/m}^2$) and $1.8 \pm 1.2^\circ$ for cyclohexane ($\gamma_l = 25.2 \text{ mJ/m}^2$). The other probe liquids tested could not be repelled due a contact angle of 0° , but also here the film of ionic

liquid on the surface below the probe liquid was not disturbed. They are therefore not eligible for SLIPS systems, but they still might be interesting for other applications where an immobilized ionic liquid in contact with another solvent is required. A brief overview of the results obtained in this work were also published [77].

In contrast to Cassie-Baxter systems, SLIPS are a more recently discovered topic. Hence, research covering it is, in comparison, scarce. There is especially very little research describing the use of ionic liquids in SLIPS despite their advantages regarding negligible evaporation and better tuneable surface tension. The few existing works then focus mainly on water as probe liquid, which is a good model system but water repellence is in general also achievable in way simpler arrangements. The repellence of low surface tension liquids on ionic liquid based SLIPS is, to our best knowledge, yet only reported once in literature [49]. They reported a roll-off angle of $3.7 \pm 1.2^\circ$ for n-decane ($\gamma_l = 23.6 \text{ mJ/m}^2$) on a fluorinated ionic liquid.

Possible successive work should mainly focus on the improvement of the used model to predict the behaviour of the ionic liquids, since we still found significant discrepancies between the predicted and the observed behaviour. Secondly, screening of a wider range of ionic liquids is necessary to find suitable surface compositions for all common solvents.

6 References

The approved original version of this thesis is
available at the main library of the Vienna
University of Technology.

<http://www.ub.tuwien.ac.at>

1. Bhushan, B., *Biomimetics: lessons from nature - an overview*. Philos. Trans. R. Soc., A, 2009. **367**(1893): p. 1445-1486.
2. Barthlott, W. and C. Neinhuis, *Purity of the sacred lotus, or escape from contamination in biological surfaces*. Planta, 1997. **202**(1): p. 1-8.
3. Feng, L., et al., *Super-hydrophobic surfaces: from natural to artificial*. Adv. Mater. (Weinheim, Ger.), 2002. **14**(24): p. 1857-1860.
4. Lee, W., et al., *Nanostructuring of a Polymeric Substrate with Well-Defined Nanometer-Scale Topography and Tailored Surface Wettability*. Langmuir, 2004. **20**(18): p. 7665-7669.
5. Watson, G.S., et al., *Putative functions and functional efficiency of ordered cuticular nanoarrays on insect wings*. Biophys. J., 2008. **94**(8): p. 3352-3360.
6. Wagner, T., C. Neinhuis, and W. Barthlott, *Wettability and Contaminability of Insect Wings as a Function of Their Surface Sculptures*. Acta Zoologica, 1996. **77**(3): p. 213-225.
7. Gu, Z.-Z., et al., *Structural color and the lotus effect*. Angew. Chem., Int. Ed., 2003. **42**(8): p. 894-897.
8. Vukusic, P. and J.R. Sambles, *Photonic structures in biology*. Nature (London, U. K.), 2003. **424**(6950): p. 852-855.
9. Hu, D.L., B. Chan, and J.W.M. Bush, *The hydrodynamics of water strider locomotion*. Nature (London, U. K.), 2003. **424**(6949): p. 663-666.
10. Parker, A.R. and C.R. Lawrence, *Water capture by a desert beetle*. Nature (London, U. K.), 2001. **414**(6859): p. 33-34.
11. Shirtcliffe, N.J., G. McHale, and M.I. Newton, *Learning from Superhydrophobic Plants: The Use of Hydrophilic Areas on Superhydrophobic Surfaces for Droplet Control*. Langmuir, 2009. **25**(24): p. 14121-14128.
12. Cassie, A.B.D. and S. Baxter, *Wettability of porous surfaces*. Trans. Faraday Soc., 1944. **40**: p. 546-51.
13. Nishimoto, S. and B. Bhushan, *Bioinspired self-cleaning surfaces with superhydrophobicity, superoleophobicity, and superhydrophilicity*. RSC Adv., 2013. **3**(3): p. 671-690.
14. Liu, M., et al., *Bioinspired design of a superoleophobic and low adhesive water/solid interface*. Adv. Mater. (Weinheim, Ger.), 2009. **21**(6): p. 665-669.
15. Bauer, U. and W. Federle, *The insect-trapping rim of Nepenthes pitchers: surface structure and function*. Plant Signal Behav, 2009. **4**(11): p. 1019-23.
16. Wong, T.-S., et al., *Bioinspired self-repairing slippery surfaces with pressure-stable omniphobicity*. Nature (London, U. K.), 2011. **477**(7365): p. 443-447.
17. Schuyten, H.A., et al., *Imparting Water-Repellency to Textiles by Chemical Methods: A Review of the Literature*. Textile Research Journal, 1948. **18**(8): p. 490-503.
18. Tomsic, B., et al., *Sol-gel coating of cellulose fibers with antimicrobial and repellent properties*. J. Sol-Gel Sci. Technol., 2008. **47**(1): p. 44-57.
19. Na, B. and R.L. Webb, *A fundamental understanding of factors affecting frost nucleation*. Int. J. Heat Mass Transfer, 2003. **46**(20): p. 3797-3808.
20. Tourkine, P., M. Le Merrer, and D. Quere, *Delayed Freezing on Water Repellent Materials*. Langmuir, 2009. **25**(13): p. 7214-7216.
21. Kulinich, S.A. and M. Farzaneh, *Ice adhesion on super-hydrophobic surfaces*. Appl. Surf. Sci., 2009. **255**(18): p. 8153-8157.
22. Kawai, T., H. Nishihara, and K. Aramaki, *Inhibition effects of amines and thiols on iron corrosion in anhydrous methanol solution containing FeCl₃*. J. Electrochem. Soc., 1996. **143**(12): p. 3866-3873.

23. Zhang, F., et al., *Corrosion resistance of superhydrophobic layered double hydroxide films on aluminum*. *Angew. Chem., Int. Ed.*, 2008. **47**(13): p. 2466-2469.
24. Liu, T., et al., *Corrosion behavior of super-hydrophobic surface on copper in seawater*. *Electrochimica Acta*, 2007. **52**(28): p. 8003-8007.
25. Liu, T., et al., *Super-hydrophobic surfaces improve corrosion resistance of copper in seawater*. *Electrochimica Acta*, 2007. **52**(11): p. 3709-3713.
26. Hermelin, E., et al., *Ultrafast Electrosynthesis of High Hydrophobic Polypyrrole Coatings on a Zinc Electrode: Applications to the Protection against Corrosion*. *Chem. Mater.*, 2008. **20**(13): p. 4447-4456.
27. Meng, H., et al., *Facile means of preparing superamphiphobic surfaces on common engineering metals*. *J. Phys. Chem. C*, 2008. **112**(30): p. 11454-11458.
28. Min, W.-L., B. Jiang, and P. Jiang, *Bioinspired self-cleaning antireflection coatings*. *Adv. Mater. (Weinheim, Ger.)*, 2008. **20**(20): p. 3914-3918.
29. Shirtcliffe, N.J., et al., *Superhydrophobic Copper Tubes with Possible Flow Enhancement and Drag Reduction*. *ACS Appl. Mater. Interfaces*, 2009. **1**(6): p. 1316-1323.
30. Wang, B., et al., *Biomimetic super-lyophobic and super-lyophilic materials applied for oil/water separation: A new strategy beyond nature*. *Chem. Soc. Rev.*, 2015. **44**(1): p. 336-361.
31. Chu, Z., Y. Feng, and S. Seeger, *Oil/Water Separation with Selective Superantiwetting/Superwetting Surface Materials*. *Angew. Chem., Int. Ed.*, 2015. **54**(8): p. 2328-2338.
32. Prime, K.L. and G.M. Whitesides, *Adsorption of proteins onto surfaces containing end-attached oligo(ethylene oxide): a model system using self-assembled monolayers*. *J. Am. Chem. Soc.*, 1993. **115**(23): p. 10714-21.
33. Sun, T., et al., *No platelet can adhere—largely improved blood compatibility on nanostructured superhydrophobic surfaces*. *Small*, 2005. **1**(10): p. 959-963.
34. Mehnert, C.P., et al., *Supported Ionic Liquid Catalysis - A New Concept for Homogeneous Hydroformylation Catalysis*. *J. Am. Chem. Soc.*, 2002. **124**(44): p. 12932-12933.
35. Sun, M., et al., *Artificial Lotus Leaf by Nanocasting*. *Langmuir*, 2005. **21**(19): p. 8978-8981.
36. Minko, S., et al., *Two-level structured self-adaptive surfaces with reversibly tunable properties*. *J Am Chem Soc*, 2003. **125**(13): p. 3896-900.
37. Fuerstner, R., et al., *Wetting and Self-Cleaning Properties of Artificial Superhydrophobic Surfaces*. *Langmuir*, 2005. **21**(3): p. 956-961.
38. Sheen, Y.-C., et al., *New approach to fabricate an extremely super-amphiphobic surface based on fluorinated silica nanoparticles*. *J. Polym. Sci., Part B: Polym. Phys.*, 2008. **46**(18): p. 1984-1990.
39. Hosono, E., et al., *Superhydrophobic Perpendicular Nanopin Film by the Bottom-Up Process*. *J. Am. Chem. Soc.*, 2005. **127**(39): p. 13458-13459.
40. Deng, X., et al., *Candle Soot as a Template for a Transparent Robust Superamphiphobic Coating*. *Science*, 2012. **335**(6064): p. 67.
41. Sun, T., et al., *Control over the Wettability of an Aligned Carbon Nanotube Film*. *Journal of the American Chemical Society*, 2003. **125**(49): p. 14996-14997.
42. Liu, T. and C.-J. Kim, *Turning a surface superrepellent even to completely wetting liquids*. *Science (Washington, DC, U. S.)*, 2014. **346**(6213): p. 1096-1100.
43. Dai, X., et al., *Slippery Wenzel State*. *ACS Nano*, 2015. **9**(9): p. 9260-9267.
44. Smith, J.D., et al., *Droplet mobility on lubricant-impregnated surfaces*. *Soft Matter*, 2013. **9**(6): p. 1772-1780.
45. Maoz, R. and J. Sagiv, *On the formation and structure of self-assembling monolayers. I. A comparative atr-wettability study of Langmuir—Blodgett and adsorbed films on flat substrates and glass microbeads*. *Journal of Colloid and Interface Science*, 1984. **100**(2): p. 465-496.
46. He, Y. and Y. Su, *Silicon Nano-biotechnology*. 2014: Springer.

47. Huang, Z., et al., *Metal-Assisted Chemical Etching of Silicon: A Review In memory of Prof. Ulrich Goesele*. Adv. Mater. (Weinheim, Ger.), 2011. **23**(2): p. 285-308.
48. Dawood, M.K., et al., *Mimicking Both Petal and Lotus Effects on a Single Silicon Substrate by Tuning the Wettability of Nanostructured Surfaces*. Langmuir, 2011. **27**(7): p. 4126-4133.
49. Miranda, D.F., et al., *Physically and chemically stable ionic liquid-infused textured surfaces showing excellent dynamic omniphobicity*. APL Materials, 2014. **2**(5): p. 056108.
50. Young, T., *An Essay on the Cohesion of Fluids*. Phil. Trans. R. Soc. Lond., 1805. **95**: p. 65-87.
51. Fowkes, F.M., *Attractive forces at interfaces*. Ind. Eng. Chem., 1964. **56**(12): p. 40-52.
52. Fowkes, F.M., *Donor-acceptor interactions at interfaces*. J. Adhes., 1972. **4**(2): p. 155-9.
53. Owens, D.K. and R.C. Wendt, *Estimation of the surface free energy of polymers*. J. Appl. Polym. Sci., 1969. **13**(8): p. 1741-7.
54. Kaelble, D.H., *Dispersion-polar surface tension properties of organic solid*. J. Adhes., 1970. **2**(April): p. 66-81.
55. Rabel, W., *Wetting theory and its application to the study and use of the surface properties of polymers*. Farbe Lack, 1971. **77**(10): p. 997-1006.
56. Żenkiewicz, M., *Methods for the calculation of surface free energy of solids*. Journal of Achievements in Materials and Manufacturing Engineering, 2007. **24**(1): p. 137-145.
57. Nishino, T., et al., *The Lowest Surface Free Energy Based on -CF₃ Alignment*. Langmuir, 1999. **15**(13): p. 4321-4323.
58. Janczuk, B. and T. Bialopiotrowicz, *Surface free-energy components of liquids and low energy solids and contact angles*. J. Colloid Interface Sci., 1989. **127**(1): p. 189-204.
59. Schultz, J., K. Tsutsumi, and J.B. Donnet, *Surface properties of high-energy solids. II. Determination of the nondispersive component of the surface free energy of mica and its energy of adhesion to polar liquids*. J. Colloid Interface Sci., 1977. **59**(2): p. 277-82.
60. Good, R.J., *ADVANCE Substance Database*.
61. Wenzel, R.N., *Resistance of solid surfaces to wetting by water*. Ind. Eng. Chem., 1936. **28**: p. 988-94.
62. Bressers, P.M.M.C., et al., *Surface morphology of p-type (100) silicon etched in aqueous alkaline solution*. J. Electrochem. Soc., 1996. **143**(5): p. 1744-1750.
63. Huang, Z., et al., *Oxidation Rate Effect on the Direction of Metal-Assisted Chemical and Electrochemical Etching of Silicon*. J. Phys. Chem. C, 2010. **114**(24): p. 10683-10690.
64. Bashforth, F. and J.C. Adams, *An attempt to test the theories of capillary action by comparing theoretical and measured forms of drops of fluid*. Cambridge University Press, 1883.
65. Chi, Y.S., et al., *Control of Wettability by Anion Exchange on Si/SiO₂ Surfaces*. Langmuir, 2004. **20**(8): p. 3024-3027.
66. Huisgen, R., *1,3-Dipolar cycloaddition - introduction, survey, mechanism*. 1984. Wiley.
67. Henriksson, A., G. Friedbacher, and H. Hoffmann, *Surface Modification of Silicon Nanowires via Copper-Free Click Chemistry*. Langmuir, 2011. **27**(12): p. 7345-7348.
68. Vazquez, G., E. Alvarez, and J.M. Navaza, *Surface Tension of Alcohol Water + Water from 20 to 50 °C*. J. Chem. Eng. Data, 1995. **40**(3): p. 611-14.
69. *GESTIS-Stoffdatenbank*. 11.7.2017]; Available from: www.dguv.de/ifa/stoffdatenbank.
70. Anand, S., et al., *Enhanced Condensation on Lubricant-Impregnated Nanotextured Surfaces*. ACS Nano, 2012. **6**(11): p. 10122-10129.
71. Wong, T.-S., et al., *Bioinspired self-repairing slippery surfaces with pressure-stable omniphobicity*. Nature, 2011. **477**(7365): p. 443-447.
72. Janczuk, B. and T. Bialopiotrowicz, *The total surface free energy and the contact angle in the case of low energetic solids*. J. Colloid Interface Sci., 1990. **140**(2): p. 362-72.
73. Nguyen, T.P.N., et al., *Fabrication of superhydrophobic and highly oleophobic silicon-based surfaces via electroless etching method*. Appl. Surf. Sci., 2014. **295**: p. 38-43.

74. Kim, B.S., et al., *Control of Superhydrophilicity/Superhydrophobicity using Silicon Nanowires via Electroless Etching Method and Fluorine Carbon Coatings*. Langmuir, 2011. **27**(16): p. 10148-10156.
75. Wu, X., L. Zheng, and D. Wu, *Fabrication of Superhydrophobic Surfaces from Microstructured ZnO-Based Surfaces via a Wet-Chemical Route*. Langmuir, 2005. **21**(7): p. 2665-2667.
76. Zhang, G., et al., *Fabrication of Superhydrophobic Surfaces from Binary Colloidal Assembly*. Langmuir, 2005. **21**(20): p. 9143-9148.
77. Bittner, R.W., K. Bica, and H. Hoffmann, *Fluorine-free, liquid-repellent surfaces made from ionic liquid-infused nanostructured silicon*. Monatshefte für Chemie - Chemical Monthly, 2017. **148**(1): p. 167-177.

7 List of Figures

The approved original version of this thesis is
available at the main library of the Vienna
University of Technology.

<http://www.ub.tuwien.ac.at>

Figure 1: Involved forces at the boundary of a drop according to Young.....	9
Figure 2: Wenzel wetting state.	13
Figure 3: Calculated rough contact angles as a function of the flat contact angle according to the Wenzel state.....	14
Figure 4: Cassie-Baxter wetting state.....	14
Figure 5: Calculated rough contact angle as a function of the flat contact angle according to the Cassie-Baxter state.	15
Figure 6: Impregnated Cassie-Baxter wetting state.....	15
Figure 7: Calculated rough contact angle as a function of the flat contact angle according to the impregnated Cassie-Baxter state.	16
Figure 8: Representation of the most stable wetting state on a rough surface (green) superimposed on calculated rough contact angles according to the Cassie-Baxter, Wenzel and impregnated Cassie-Baxter state (black).....	18
Figure 9: Representation of the collapse of the Cassie-Baxter state and transition to the Wenzel state.....	18
Figure 10: Contact angles of thermodynamic stable states (green) and metastable Cassie-Baxter state (black) on rough surfaces as a function of the flat contact angle.	20
Figure 11: Advancing and receding contact angle in the Cassie-Baxter state.....	20
Figure 12: Advancing and receding contact angle in the Wenzel state.	22
Figure 13: SLIPS scheme.	23
Figure 14: SLIPS regions for stability considerations.....	23
Figure 15: Different possible wetting states in region 1.	23
Figure 16: A: Results of the inequations between the energies of the different wetting states in region 1; B: Most stable state in region 1.	24
Figure 17: Different possible wetting states in region 2.	25
Figure 18: A: Results of the inequations between the energies of the different wetting states in region 2; B: Most stable state for region 2.....	26
Figure 19: Transition between complete ($\theta = 0^\circ$) and non-complete ($\theta > 0^\circ$) wetting on SLIPS.	27
Figure 20: Transition between cloaking and non-cloaking behaviour on SLIPS.....	27
Figure 21: Metal-assisted etching schema.	28
Figure 22: Schematic of a Brewster angle FTIR setup highlighting the partial polarization due to an angle of incidence (κ_1).	31

Figure 23: Reflectivity of s- and p-polarized light as a function of the angle of incidence for silicon and air.	32
Figure 24: Schematic arrangement for ellipsometric measurements.	32
Figure 25: Schematic arrangement for goniometric measurements.	34
Figure 26: Representation of drop contour and baseline in goniometric measurements.	35
Figure 27: Representation of the different parameters used for the Young-Laplace method.	35
Figure 28: Bruker Vertex 80 FTIR with open sample chamber and sample holder for Brewster angle measurements.	40
Figure 29: Sentech SE 500adv ellipsometer and power supply.	41
Figure 30: Krüss DSA 30 goniometer.	41
Figure 31: Pictures of cross-sections (top) and top-views (bottom) captured in SEM of nanowire samples etched with different H ₂ O ₂ concentrations.	45
Figure 32: Representation of the procedure for determining ϕ from a top-view SEM image. Left: Section of the original SEM picture of a sample etched with 0.06 M H ₂ O ₂ ; Middle: Same section after converting it to black and white; Right: Same section after averaging the grey scale.	46
Figure 33: CH region of samples etched with different H ₂ O ₂ concentration and coated with OTS and their calculated signal-to-noise ratio (S/N).	47
Figure 34: Transmission of infrared light of nanowire covered silicon samples etched with different H ₂ O ₂ concentrations referenced to flat silicon.	48
Figure 35: Pictures of cross-sections (top) and top-views (bottom) captured in SEM of nanowire samples etched for different durations. Pictures for 10 minutes etching duration taken from series conducted in 4.1.1.1.	49
Figure 36: Transmission of infrared light of nanowire covered silicon samples etched for different durations in 0.06 M H ₂ O ₂ and referenced to flat silicon.	50
Figure 37: Top-view SEM images of a sample treated with silver (5 mM, 1 minute) solution with two details at higher magnification of silver nanoparticles (bottom right) and silver dendrites (top right).	51
Figure 38: Grey scales: FTIR transmission spectra of nanowire covered silicon samples etched with different H ₂ O ₂ concentrations referenced to flat silicon; Green: Average transmission of samples etched after refilling 0.02 ml H ₂ O ₂ , 36 wt.%, in the etching solution after each sample starting with 0.06 M.	53
Figure 39: Reaction scheme for covalent coating of silicon substrates with trichlorosilane.	54
Figure 40: Reaction scheme for surface modification of BUTS coatings with sodium azide and copper catalysed Huisgen 1,3-dipolar cycloaddition of THFDP.	55

Figure 41: FTIR spectra of nanowire samples treated with a coating solution containing BUTS for different durations, each averaged over three samples.....	57
Figure 42: FTIR spectrum of OTS on nanowire substrate, averaged over three samples.....	58
Figure 43: FTIR spectra of BUTS coated nanowire samples etched with 0.12 M H ₂ O ₂ after treatment with sodium azide for various durations, both spectra averaged over two samples.	59
Figure 44: FTIR spectra of BUTS coated nanowire samples etched with 0.06 M H ₂ O ₂ after treatment with sodium azide for various durations, both spectra averaged over four samples.....	60
Figure 45: THFDP with labelled CH groups correlating with ¹ H NMR peaks shown in Figure 47.....	60
Figure 46: FTIR spectrum of THFDP between two sodium chloride windows.	61
Figure 47: ¹ H-NMR of THFDP in CDCl ₃ with a magnification of the triplet of triplets at around 2.54ppm.	61
Figure 48: FTIR spectrum of cTHFDP on nanowire substrates, averaged over four samples.	62
Figure 49: Evaporation of a drop without extra precautions. Left: Decrease of drop volume of a mixture of 69.96 wt.% water and 30.04 wt.% ethanol as a function of time due to evaporation; Top right: Drop at the beginning of the measurement; Bottom right: Drop at the end of the measurement.	63
Figure 50: Rendered 3D model of the sample housing used to obtain an atmosphere saturated with probe liquid around the drop of probe liquid for contact angle measurements.....	64
Figure 51: Picture of the 3D printed housing mounted on the sample stage of the goniometer. ...	65
Figure 52: Evaporation of a drop in a housing. Left: Decrease of drop volume of a mixture of 69.96 wt.% water and 30.04 wt.% ethanol as a function of time due to evaporation; Top right: Drop at the beginning of the measurement; Bottom right: Drop at the end of the measurement.	66
Figure 53: Surface tension of water-ethanol mixtures as a function of composition [68].	67
Figure 54: Contact angle of different probe liquids on cTHFDP, OTS and 11-N ₃ modified flat surfaces as a function of surface tension. Range between advancing and receding angle is semi-transparently coloured.	70
Figure 55: Contact angle of different probe liquids on cTHFDP, OTS and 11-N ₃ modified nanowire surfaces as a function of surface tension. Range between advancing and receding angle is semi-transparently coloured.....	70
Figure 56: Images captured during contact angle measurements of different probe liquids on cTHFDP coated nanowire substrates. A: Pure water ($\gamma_l = 72.9 \pm 0.9$ mJ/m ²); B: A mixture of 53.33 wt.% ethanol and 46.67 wt.% water ($\gamma_l = 27.4 \pm 0.2$ mJ/m ²); C: Pure ethanol ($\gamma_l = 23.03 \pm 0.02$ mJ/m ²).....	71
Figure 57: Zisman plot assuming that the Berthelot hypothesis is valid over the whole range.....	72

Figure 58: Zisman plot using a cubic polynomial to extrapolate to $\cos\theta = 0$.	73
Figure 59: Assumed polar and dispersive components for water-ethanol mixtures calculated from pure water and pure ethanol.	74
Figure 60: Zisman plot based on the OWKR approximation and the assumption for the polar and dispersive share of water-ethanol mixtures.	74
Figure 61: Overview over all plots used to determine surface energies from advancing and receding contact angles. A: Data fitted according to Equation 15, assuming a valid Berthelot hypothesis over the whole range. Subsequent extrapolation to $\cos\theta = 0^\circ$ gives γ_s ; B: Data fitted with a cubic polynomial. Subsequent extrapolation to $\cos\theta = 0^\circ$ gives γ_s ; C: Data fitted according to Equation 53 using the assumption presented in Figure 59. Slope and abscissa used for determination of γ_{sd} and γ_{sp} . Extrapolation to $\cos\theta = 0^\circ$ gives γ_s .	79
Figure 62: Plot of cosine of contact angle measurements on flat substrates ($\cos\theta$) against cosine of contact angle measurements on rough substrate ($\cos\theta^*$) to determine ϕ and r according to Equation 16 and 17.	80
Figure 63: $[\text{C}_3\text{mim}]\text{Cl}$ with labelled CH groups correlating with $^1\text{H-NMR}$ peaks found in Figure 65.	86
Figure 64: IR spectrum of $[\text{C}_3\text{mim}]\text{Cl}$ between two sodium chloride windows.	86
Figure 65: $^1\text{H-NMR}$ measurement of $[\text{C}_3\text{mim}]\text{Cl}$ in CDCl_3 .	87
Figure 66: FTIR spectrum of $[\text{C}_3\text{mim}]\text{Cl}$ on nanowire substrate, averaged over fifteen samples.	88
Figure 67: FTIR spectrum of $[\text{C}_3\text{mim}]\text{Cl}$ on flat substrate, averaged over three samples.	88
Figure 68: Comparison of a measurement showing a THF emulsion as surrounding with a measurement showing cyclohexane as surrounding. All other probe liquids investigated here showed similar behaviour as cyclohexane in this regard. In both pictures the contrast was increased identically to highlight the light scattering effects due to the emulsion found in THF.	92
Figure 69: Cyclohexane (left row) and toluene (middle row) rolling-off a SiO_2 -terminated SLIPS surfaces with $[\text{C}_2\text{mim}][\text{MeSO}_4]$ as impregnation liquid in comparison with water rolling off a Cassie-Baxter surface (right row). In the first picture of each series the drop can be seen with horizontal sample stage and the measured contact angle. The second picture marks the point where the drops started moving and thus the roll-off angle was reached. The remaining pictures show the movement of the drop a few seconds after the drop started moving. For easier recognition of the drop in SLIPS, both ends of the drops in the picture were highlighted with red arrows. The denoted angles in the picture deviate slightly from the averaged values presented in Table 28 since they represent the measured value only for the single depicted measurement.	98

8 List of Tables

The approved original version of this thesis is
available at the main library of the Vienna
University of Technology.

<http://www.ub.tuwien.ac.at>

Table 1: General characteristic of different preparation methods for Cassie-Baxter systems with + and - representing advantageous and disadvantageous behaviour, respectively. Approach 1: Top-down methods applied on low surface energy substrate; Approach 2: Top-down methods applied to any substrate with subsequent surface modification; Approach 3: Bottom-up methods using low surface energy building blocks; Approach 4: Bottom-up methods using any building blocks with subsequent surface modification.	5
Table 2: Total, polar and dispersive surface tension of different liquids and calculated contact angle on a flat $C_{20}F_{42}$ surface using the Young equation.....	13
Table 3: Calculated roughness from the ratio of CH bands measured in the FTIR between flat and nanowire sample etched with different H_2O_2 concentration and coated with OTS.	47
Table 4: Calculated r , ϕ and signal-to-noise ratio of samples etched for different durations in 0.06 M H_2O_2 using BUTS coating. ¹ : Data for 10 minutes etching duration taken from series conducted in 4.1.1.1 using OTS coating.	49
Table 5: Decline in weight gain due to the treatment in silver solution when no additional silver is added.....	51
Table 6: Layer thickness of BUTS coated samples as a function of coating duration.	55
Table 7: Integral of the CH region ($2770-3000\text{ cm}^{-1}$) as a function of coating duration.	56
Table 8: Layer thickness of OTS coated samples as a function of coating duration.	57
Table 9: Time dependency of the integral of the asymmetric stretching vibration of azide after treatment of BUTS coated nanowire samples etched with 0.12 M H_2O_2 for various durations with sodium azide.....	59
Table 10: Time dependency of the integral of the asymmetric stretching vibration of azide after treatment of BUTS coated nanowire samples etched with 0.06 M H_2O_2 for various durations with sodium azide.....	59
Table 11: Surface tension of water-ethanol mixtures as a function of composition [68].	67
Table 12: Composition and characterization of the water-ethanol mixtures used as probe liquids for contact angle measurements.....	68
Table 13: Measured contact angles (θ) as well as receding ($\theta_{rec.}$) and advancing ($\theta_{adv.}$) contact angles of different probe liquids on flat and nanowire (NW) substrates coated with different compounds.....	69
Table 14: Calculated surface energy of cTHFDP, OTS and 11- N_3 using the Young equation and the OWKR-approximation.	71

Table 15: Calculated surface tension to reach a contact angle of 0° on different surfaces using on one hand the Berthelot equation and on the other hand a cubic polynomial to extrapolate the data.	73
Table 16: Calculated surface energy from a linear fit based on contact angle measurements plotted according to the OWKR approximation in combination with the Young equation and an approximation of γ_{ld} and γ_{lp}	75
Table 17: Calculated surface tension to reach a contact angle of 0° on different surfaces using the OWKR approximation in combination with the Young equation and an approximation of γ_{ld} and γ_{lp}	75
Table 18: Summary of the calculated surface energies of different coatings. ^I : Highly unreliable due to unfulfilled theoretical requirements; ^{II} : Inaccurate due to extrapolation without theoretical background; ^{III} : Underestimates the surface energy due to unfulfilled requirements for the Berthelot hypothesis at $\theta = 0^\circ$; ^{IV} : No precise evaluation possible due to negative abscissa.	77
Table 19: Summary of the calculated surface energies of different coatings using advancing contact angles. ^I : Highly unreliable due to unfulfilled theoretical requirements; ^{II} : Inaccurate due to extrapolation without theoretical background; ^{III} : Underestimates the surface energy due to unfulfilled requirements for the Berthelot hypothesis at $\theta = 0^\circ$; ^{IV} : No precise evaluation possible due to negative abscissa; ^V : Unreliable results due to bad fit of the regression curve with the data.	77
Table 20: Summary of the calculated surface energies of different coatings using receding contact angles. ^I : Highly unreliable due to unfulfilled theoretical requirements; ^{II} : Inaccurate due to extrapolation without theoretical background; ^{III} : Underestimates the surface energy due to unfulfilled requirements for the Berthelot hypothesis at $\theta = 0^\circ$; ^{IV} : No precise evaluation possible due to negative abscissa.	78
Table 21: Structure of selected ionic liquids investigated regarding their suitability as impregnation liquid for SLIPS systems.....	83
Table 22: Measured contact angles on 11-N ₃ and cTHFDP coated surfaces and calculated polar and dispersive component of the surface tension for selected ionic liquids.	84
Table 23: Investigation of the solubility of different organic solvents with [C ₂ mim][MeSO ₄] by mixing 500 μ l solvent with 500 μ l ionic liquid, stirring and checking after 4 hours the number of formed phases.	90
Table 24: Contact angle data for [C ₂ mim][MeSO ₄] on SiO ₂ and [C ₃ mim]Cl coated flat substrates with different surrounding phases. For the measurements of [C ₂ mim][MeSO ₄] surrounded by another liquid, both liquids were saturated with each other before the measurement took place.	91

Table 25: Overview over density measurements in comparison with values from literature and surface and interface tension measurements using the measured density values for the evaluation. For the surface and interface tension measurements, i represents $[C_2mim][MeSO_4]$ whereas l represents the different probe liquids. The compound in curly brackets indicates the liquid used to saturate the investigated liquid before the measurement took place.	93
Table 26: Calculated terms according to the conditions presented in Equation 55 and 56 for cloaking and complete wetting of probe liquid on the impregnation liquid. Values smaller than 1 are unproblematic for either behaviour.....	93
Table 27: Contact angle data and parameters describing cloaking and wetting behaviour either directly taken from literature or recalculated from published values to fit the representation style chosen here. Surrounding of the contact angle measurement indicated in curly brackets. A thermodynamically stable SLIPS system requires contact angles of 0° under both surroundings and values for cloaking and wetting smaller than 1. ^I : The used coating abbreviated as FDTs is heptadecafluoro - 1,1,2,2 – tetrahydrodecyltrichlorosilane; ^{II} : Values for θ_i {probe liquid} were calculated from published values of ΔE_1 , r and γ_{il} using the relation $\Delta E_1 = \gamma_{il} (r \cos\theta_i - 1)$; ^{III} : Surface and interface tensions for the calculation of the cloaking and wetting behaviour have been taken from [70]; ^{IV} : 1-Butyl-3-methylimidazolium bis(trifluoro-methyl-sulfonyl) imide.....	94
Table 28: Measured contact angles of SLIPS systems with different probe liquids and surface treatments.....	96

9 List of Abbreviations

The approved original version of this thesis is
available at the main library of the Vienna
University of Technology.

<http://www.ub.tuwien.ac.at>

[C₂mim][MeSO₄] - 1-ethyl-3-methyl-1H-imidazol-3-ium methyl sulfate (see Table 21)

[C₃mim]Cl - 3-methyl-1-(3-(trimethoxysilyl) propyl)-1H-imidazol-3-ium chloride

11-N₃ – Silicon surface treated with BUTS and sodium azide to replace the terminal bromine with an azide group

Bmim - 1-Butyl-3-methylimidazolium bis(trifluoro-methyl-sulfonyl) imide

BUTS - 11-bromoundecyltrichlorosilane

CAD – Computer aided design

CB - Cassie-Baxter state (see 2.1.3)

CDCl₃ - Deuterated chloroform

cTHFDP - 11-N₃ treated silicon surface subsequently modified with THFDP

DMF - N,N-Dimethylformamide

DMSO - Dimethyl sulfoxide

FDTS - Heptadecafluoro - 1,1,2,2 – tetrahydrodecyltrichlorosilane

FTIR - Fourier-transform infrared spectroscopy

HF - Hydrofluoric acid

IR - Infrared spectroscopy

MCT – Mercury cadmium tellurite

NMR - Nuclear magnetic resonance spectroscopy

NW - Nanowire

OTS - Trichloro(octadecyl)silane

OWKR - Owens, Wendt, Rabel and Kaelble approximation (see Equation 9)

PTFE - Polytetrafluoroethylene

r - Surface roughness

SEM - Scanning electron microscopy

SILP - Supported ionic liquid phases

SLIPS - Slippery liquid infused porous surface (see 2.1.5)

THFDP - 3,3,4,4,5,5,6,6,7,7,8,8,9,9,10,10,10-heptadecafluorodecyl propiolate

W - Wenzel state (see 2.1.3)

ϕ - Solid fraction at the outermost surface

θ - Contact angle

10 Curriculum Vitae

The approved original version of this thesis is
available at the main library of the Vienna
University of Technology.

<http://www.ub.tuwien.ac.at/>

Roland Wolfgang Bittner, BSc, MSc

Personal Information

Date of birth 21. April 1986
Nationality Austrian

Contact

Address Pannaschgasse 4/11, 1050 Wien
Telephone number +43 699 12369885
E-Mail rolandbittner@gmx.at

Education and Career

From 1.4.2013 PhD thesis at the Institute of Applied Synthetic Chemistry at the TU Vienna with the title 'Liquid-Repellent Surfaces based on Nanostructured Silicon Substrates' under supervision of Ao.Univ.Prof. Dipl.-Ing. Dr.techn. Helmuth Hoffmann

1.9.2012 – 31.12.2012 Project work at the University of Vienna under supervision of Ao. Univ.-Prof Dr. Hans Flandorfer

28.8.2012 Graduation with the degree Master of Science with distinction

14.2.2011 – 14.3.2011 Research stay at the EMPA in Dübendorf, Switzerland, for brazing experiments in the course of the master thesis

2010 - 2012 Master thesis at the Institute for Inorganic Chemistry/Materials Chemistry at the University of Vienna with the title 'Investigation of the aluminium-germanium-titanium phase diagram for brazing applications' under supervision of Ao. Univ.-Prof. Dr. Klaus Richter

28.4.2009 Graduation with the degree Bachelor of Science

WS 2005 Beginning with studies of chemistry at the University of Vienna

2004 Military service with training as paramedic

1996 - 2004 Secondary School, Erzbischöfliches Privatgymnasium Borromäum

Conferences

September 2016 AOFA, Soest, Poster presentation: Benetzungseigenschaften modifizierter Siliziumoberflächen

July 2015 18. Tagung Festkörperanalytik, Vienna, Oral presentation: Benetzungseigenschaften von chemisch modifizierten Silizium Nanodrähten

March 2016 WACÖ, Vienna, Oral presentation: Flüssigkeitsabweisende Modifizierung von Siliziumoberflächen

July 2015



The approved original version of this thesis is
available at the main library of the Vienna
University of Technology

<http://www.ub.tuwien.ac.at/eng>

April 2014

8th ICAVS, Vienna, Poster presentation: Chemically modified flat and rough silicon substrates as models for liquid repellent surfaces

WACÖ, Salzburg, Oral presentation: Herstellung von super-omniphoben Siliziumoberflächen

September 2012

IRDG Spring Meeting, Vienna, Poster presentation: Chemical modification of nanostructured silicon surfaces via click chemistry

TOFA, Pula, Oral presentation: Phase diagram of aluminium-germanium-titanium

April 2012

WACÖ, Innsbruck, Oral presentation: Das Phasendiagramm von Aluminium-Germanium-Titan

September 2011

14. Österreichische Chemietage, Linz, Poster presentation: Phase diagram of aluminium-germanium-titanium

Publications and Patents

Surface Analysis with Infrared Spectroscopy, Encyclopedia of Analytical Sciences, 3rd Edition, 2018, In preparation

Wetting Properties of Surface-Modified Silicon Nanowires, In preparation

Chemoselective Supported Ionic Liquid Phase (SILP) Aldehyde Hydrogenation Catalyzed by an Fe(II) PNP Pincer Complex, Angewandte Chemie (2017), Manuscript submitted

Visible light-induced cis/trans isomerization of dicarbonyl Fe(II) PNP pincer complexes, Polyhedron (2017), Manuscript accepted

A195/2017 SERS Substrat, Patent in registration

Fluorine-free, liquid-repellent surfaces made from ionic liquid-infused nanostructured silicon, Monatshefte für Chemie (2017), 148(1), 167-177

Al-Ge-Ti: Phase equilibria and structural characterization of new ternary compounds, Intermetallics (2014), 53, 157-168

Revision of the Ge-Ti phase diagram and structural stability of the new phase Ge₄Ti₅, Journal of Alloys and Compounds (2013), 577, 211-216

Awards

Best Young Scientist Paper Award 2017 for 'Fluorine-free, liquid-repellent surfaces made from ionic liquid-infused nanostructured silicon'

Skills

Driving licence class B

German First language

English Fluent in speaking and writing

Good computer skills especially with Microsoft Office, CorelDraw and basic skills with Adobe Flash